

# **Thesis**

## **Theoretical study of multi-orbital correlated electron systems with Hund's coupling**

Shiro Sakai

Department of Physics  
Graduate School of Science  
University of Tokyo

December 2006



# Contents

<b>1</b>	<b>Introduction</b>	<b>1</b>
1.1	Strongly correlated electron systems . . . . .	1
1.2	The single-orbital Hubbard model . . . . .	1
1.2.1	Mott's metal-insulator transition . . . . .	2
1.2.2	Itinerant Ferromagnetism . . . . .	3
1.2.3	Superconductivity . . . . .	4
1.3	Orbital degrees of freedom . . . . .	5
1.3.1	$d$ orbitals in crystals . . . . .	5
1.3.2	Coulomb-matrix elements between $d$ electrons . . . . .	7
1.3.3	Example for real materials . . . . .	9
1.4	Motivation and outline . . . . .	14
<b>2</b>	<b>The multiorbital Hubbard model</b>	<b>17</b>
2.1	Formulation . . . . .	17
2.2	Hund's coupling . . . . .	20
<b>3</b>	<b>The dynamical mean-field theory</b>	<b>23</b>
3.1	General formalism . . . . .	23
3.2	Application to the single-orbital Hubbard model . . . . .	26
3.2.1	Mott's transition . . . . .	27
3.2.2	Ferromagnetism . . . . .	28
3.2.3	Superconductivity . . . . .	29
3.3	Application to the multiorbital Hubbard model . . . . .	30
3.3.1	Mott's transition . . . . .	30
3.3.2	Ferromagnetism . . . . .	32
3.3.3	Superconductivity . . . . .	33
3.3.4	Orbital-selective Mott's transition . . . . .	34
3.4	The LDA+DMFT method . . . . .	35
3.5	Comparison of impurity solvers . . . . .	38
<b>4</b>	<b>The auxiliary-field quantum Monte Carlo methods</b>	<b>40</b>
4.1	The Hirsch-Fye algorithm for the single-orbital case . . . . .	40
4.2	Extension to multiorbital systems . . . . .	42
4.3	Negative-sign problem . . . . .	46

4.4	Series-expansion algorithms . . . . .	47
4.5	The (Trotter + Series-expansion) algorithm . . . . .	49
4.6	Applicable region for the algorithm . . . . .	52
<b>5</b>	<b>Itinerant ferromagnetism in multiorbital systems</b>	<b>55</b>
5.1	Introduction . . . . .	55
5.1.1	Motivation . . . . .	55
5.1.2	Metallic ferromagnetism in the single-orbital Hubbard model . . .	56
5.1.3	Ferromagnetism in the multiorbital Hubbard model . . . . .	62
5.2	Comparison of the ferromagnetic instability between Ising and SU(2) Hund's couplings . . . . .	65
5.3	Effect of Hund's coupling on metallic ferromagnetism . . . . .	67
5.3.1	Consideration from the Kanamori theory — particle-hole channel	67
5.3.2	Result for the simple cubic lattice . . . . .	68
5.3.3	Result for the fcc lattice . . . . .	69
5.3.4	Discussion . . . . .	73
5.4	Summary . . . . .	76
<b>6</b>	<b>Application to a three-orbital system</b>	<b>77</b>
6.1	Introduction . . . . .	77
6.1.1	Purpose . . . . .	77
6.1.2	Correlation effects in $\text{Sr}_2\text{RuO}_4$ . . . . .	78
6.2	Crystal structure and bandstructure of $\text{Sr}_2\text{RuO}_4$ . . . . .	80
6.3	Modeling . . . . .	82
6.4	Result . . . . .	84
6.4.1	Quasiparticle spectra — Comparison between Ising and SU(2) cases	84
6.4.2	Quasiparticle mass . . . . .	86
6.5	Discussion . . . . .	86
6.6	Summary . . . . .	88
<b>7</b>	<b>Concluding remarks</b>	<b>90</b>
7.1	Summary of the thesis . . . . .	90
7.2	Future problems . . . . .	91

# Chapter 1

## Introduction

### 1.1 Strongly correlated electron systems

Electron correlation problem in transition-metal-based materials is one of the most intriguing challenges in condensed-matter physics. The materials exhibit remarkably versatile properties for electronic transport (metallic, insulating, superconducting, etc.) and magnetism (paramagnetism, ferromagnetism, antiferromagnetism, etc.), and sometimes totally change the properties according to temperature, pressure, external fields, and chemical dopings.

Experimental research for the compounds was fuelled by the discovery of high- $T_c$  superconductivity in cuprates [1], and was accelerated by subsequent discoveries of unconventional superconductivity in other materials such as  $\text{Sr}_2\text{RuO}_4$  [2], colossal magnetoresistance in manganites [3, 4, 5], complex magnetic phase diagrams in manganites [6], cobaltates [7, 8, 9], and so on.

In these materials  $d$  electrons of the transition metals dominate the low-energy properties. The diversity in physical properties is attributed to the partially localized nature of the  $d$  electrons, which hop around in a crystal, where electron-electron repulsions are as large as the kinetic energy. The duality of the itinerant and the localized features of the  $d$  electrons makes the problem quite difficult because perturbation approaches break down. Therefore theoretical studies for the system have evolved with developments of non-perturbative methods. Drastic improvements of computer facilities have further pushed theoretical studies to more realistic and accurate calculations.

### 1.2 The single-orbital Hubbard model

A simplest model for the  $d$  electrons in transition metals or their compounds is the single-orbital Hubbard model [10],

$$\hat{H} = t \sum_{ij\sigma} c_{i\sigma}^\dagger c_{j\sigma} + U \sum_i n_{i\uparrow} n_{i\downarrow}, \quad (1.1)$$

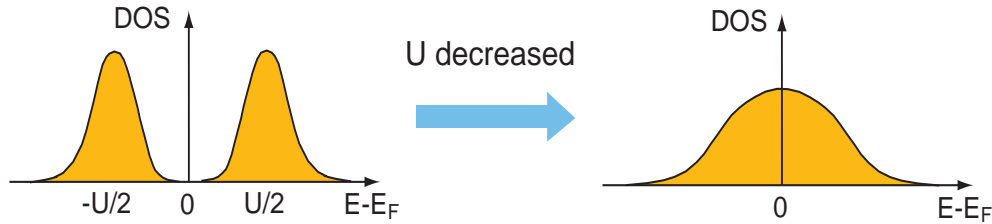


Figure 1.1: Schematic density of states in the Mott-Hubbard insulator-to-metal transition.

where  $c_{i\sigma}^\dagger$  ( $c_{i\sigma}$ ) is the creation (annihilation) operator for the electron with spin  $\sigma$  at lattice point  $i$ , and  $n_{i\sigma} \equiv c_{i\sigma}^\dagger c_{i\sigma}$ . The first term represents electron hoppings to neighboring sites, and the second term describes the on-site Coulomb repulsion ( $U > 0$ ).

It has turned out that the single-orbital Hubbard model, despite the simplicity, can describe a variety of phenomena, such as metal-insulator transition, ferromagnetism, unconventional superconductivities. In the following we give a brief introduction for these phenomena.

### 1.2.1 Mott's metal-insulator transition

In the band theory, which is based on a one-electron picture, insulators must have even number of electrons per atom. However, some transition-metal oxides are insulating in spite of having odd number of electrons per atom [11].

Mott and Peierls [12] pointed out that the insulating behavior should be due to the Coulomb repulsion between electrons: If two electrons are on the same site, the electrons feel a strong Coulomb repulsion. Hence when the interaction is large and a valence band is half filled, that is, the number of valence electrons per site is one, the electrons cannot hop among neighboring sites, and the material becomes an insulator. Such an insulator is called the Mott insulator [13].

The Hubbard Hamiltonian (1.1) should be appropriate for describing the above situation. In fact, Hubbard [10] showed that at half filling the density of states for a large  $U$  has two peaks at around  $E_F \pm \frac{U}{2}$  ( $E_F$ : the Fermi level), and an energy gap exists between the two peaks, which corresponds to the insulating behavior suggested by Mott and Peierls. As  $U$  is decreased, the gap becomes narrower and vanishes at a critical value  $U_c$ , which is an insulator-to-metal transition driven by electron correlations (Fig. 1.1). Indeed, this type of insulator-to-metal transition has been found for some Mott's insulators [14, 15], exemplified by  $V_2O_3$  [16], where the bandwidth  $W$ , and thereby  $U/W$ , is controlled by pressure or chemical dopings.

The Hubbard theory, however, fails to reproduce quasiparticle properties in the metallic state. Brinkman and Rice [17] considered Mott's transition from the metallic side in a mean-field theory. They described the transition as the divergence of the quasiparticle effective mass. However, this theory cannot reproduce the splitting of the density of states in the insulating side.

The first unified description of the Mott transition was achieved by the dynamical

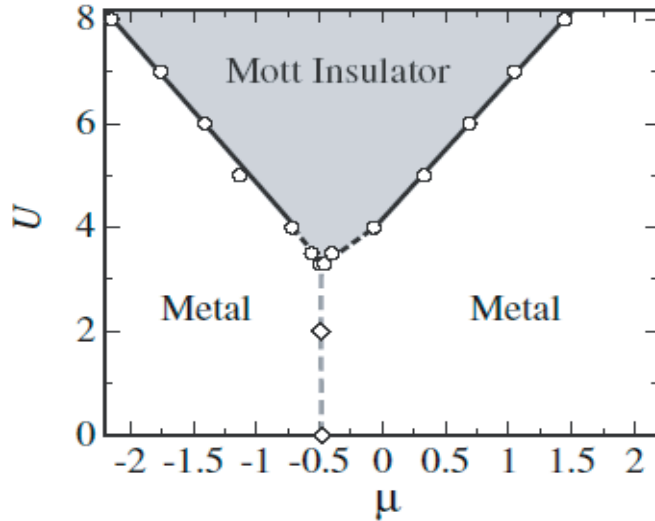


Figure 1.2: Ground-state phase diagram against  $U$  and  $\mu$  ( $\mu$ : chemical potential) for the two-dimensional single-orbital Hubbard model on the square lattice with nearest-neighbor hopping  $t = 1$  and next-nearest-neighbor hopping  $t' = -0.2$ , calculated by Watanabe and Imada [28] with the path-integral renormalization-group method. Half filling corresponds to  $\mu = -0.5$  (dashed line). (From Ref. [28].)

mean field theory (DMFT) [18]. It reproduces the insulating density of states as well as the divergence of the quasiparticle effective mass. The results are described in detail in §3.2.1. The DMFT is exact in the limit of the infinite spatial dimension, and for one, two and three dimensions the DMFT is an approximation which neglects spatial fluctuations. While the approximation is considered to be good for three dimensions, the spatial fluctuations would be significant in one and two dimensions.

The two-dimensional Hubbard model has attracted much attention since the discovery of high- $T_c$  superconductivity in cuprates which have a layered structure [1]. Because the superconductivity has been found in a hole- or electron-doped region for Mott's insulators (e.g.,  $\text{La}_2\text{CuO}_4$ ), a study for carrier-doped Mott's insulators has a special importance.

The filling-control Mott metal-insulator transitions have been studied by many authors [14], [18]-[28]. Watanabe and Imada [28] investigated the two-dimensional Hubbard model with the path-integral renormalization-group method [29], which projects a system onto its ground state through a renormalization process. They obtained the ground-state phase diagram in the plane of  $U$  and the chemical potential  $\mu$  (Fig. 1.2). The Mott transition at half filling is found to be the first order while the filling-control Mott transition is continuous, in agreement with quantum Monte Carlo studies [19].

## 1.2.2 Itinerant Ferromagnetism

The single-orbital Hubbard model (1.1) was originally introduced as a model for itinerant ferromagnetism in transition metals such as Fe, Co and Ni [10, 30, 31]. Although

the Hartree-Fock approximation provides a ferromagnetic ground state for a large  $U$ , the approximation obviously overestimates the ferromagnetic instability since electron correlation effects, which destabilize the ferromagnetic ground state [10], are neglected. To take account of the correlation effects, many approximate theories have been developed (see §5.1.2). The studies indicate that lattice structures are crucial for stabilizing ferromagnetism.

In some restricted situations, the ground state is rigorously shown to be ferromagnetic [32]. The first rigorous proof in the single-orbital Hubbard model was provided by Nagaoka [33]. He showed that the ground state in the strong-coupling limit ( $U = \infty$ ) is ferromagnetic when a single hole is doped to a half-filled band. An intuitive picture of this ferromagnetism is that the doped hole hops around the lattice, aligning electron spins localized by the infinitely large Coulomb interaction.

Another rigorous example showing ferromagnetism is a bipartite lattice with different number of sublattice sites. Lieb [34] proved that, in the ground state at half filling, each sublattice has totally aligned spins with the antiparallel sublattice magnetizations for arbitrary magnitudes of the repulsion  $U$ . Then, the different numbers of the sublattice sites result in a ferrimagnetic ground state. From the viewpoint of the momentum space, the different numbers of sublattice sites imply the existence of a flat band, where, roughly, the absence of the loss of the kinetic energy is a cause of the ferromagnetism. Mielke [35] and Tasaki [36, 37] have proved the existence of ferromagnetic ground states for a class of lattices constructed to have flat bands.

However, for more ordinary lattices and for couplings comparable to bandwidths, which is the real situation in transition metals and their oxides, the occurrence of a ferromagnetic order in the single-orbital Hubbard model is still an open question. In other words, ingredients neglected in the single-orbital Hubbard model may be important for explaining ferromagnetism in transition-metal-based materials. In §1.3 and in Chap. 5, we shall discuss the importance of the  $d$ -orbital degrees of freedom, which has been pointed out by many authors [38, 39].

### 1.2.3 Superconductivity

The discovery of high- $T_c$  superconductivity in cuprates [1] has also aroused much interest in the single-orbital Hubbard model. Since cuprates have a layered perovskite structure, the two-dimensional Hubbard model has attracted most intensive attentions. The symmetry of the gap function was experimentally identified as  $d_{x^2-y^2}$  [40]. Although a full consensus on the mechanism of high- $T_c$  superconductivity has not been achieved yet, it is expected to be explained with the mechanisms caused by electron-electron interactions.

The  $d$ -wave superconductivity mediated by spin fluctuations [41, 42] was theoretically suggested with various methods including the random phase approximation [43], the fluctuation-exchange approximation [44], and the self-consistent renormalization theory [45]. Quantum Monte Carlo simulations [46, 47, 48] for the two-dimensional Hubbard model indicate that the  $d_{x^2-y^2}$ -wave pair correlation becomes most dominant for a region slightly doped from half filling, although the superconducting transition point itself has

not been detected. Recently, Maier *et al.* [49] reported a finite  $T_c$  for the  $d_{x^2-y^2}$ -wave superconductivity in the two-dimensional Hubbard model, based on the dynamical cluster approximation (DCA) [50], which is an extension of the DMFT to incorporate spatial fluctuations (see §3.2.3). In two-dimensional systems the Mermin-Wagner theorem [51] precludes any continuous transition at finite temperatures, except for a topological transition of Kosterlitz-Thouless type [52]. Maier *et al.* discussed the relevance of their DCA result with the Kosterlitz-Thouless transition.

Since the discovery of cuprate superconductors, intensive experimental researches have found many unconventional superconductors, for example,  $\text{Sr}_2\text{RuO}_4$  [2] and a hydrated cobaltate,  $\text{Na}_x\text{CoO}_2 \cdot y\text{H}_2\text{O}$  [53]. While  $\text{Sr}_2\text{RuO}_4$  has the same crystal structure as cuprates, the superconducting symmetry was identified as spin triplet [54]. On the other hand, in  $\text{Na}_x\text{CoO}_2 \cdot y\text{H}_2\text{O}$ , Co forms a triangular lattice, in contrast to the square lattice of Cu in cuprates. The diversity of unconventional superconductors has attracted both experimental and theoretical interests.

## 1.3 Orbital degrees of freedom

Although the single-orbital Hubbard model has provided remarkably various phenomena in spite of its simplicity, the validity of the model for general transition metals and transition-metal oxides has still been an open question. An important ingredient neglected in the single-orbital Hubbard model is the orbital degrees of freedom of  $d$  electrons, i.e., the degrees of freedom of orbital angular momentum of  $d$  electrons in a transition-metal atom.

The importance of the  $d$ -orbital degeneracy, in particular of Hund's exchange coupling on ferromagnetism, was already pointed out by Slater [38] as early as in the 1930s. A vast amount of experimental and theoretical studies in the past decades have revealed the pivotal role of orbitals in transition-metal-based materials, not only on ferromagnetism but also on metal-insulator transitions and unconventional superconductivities [6]. Also a variety of new phenomena, which are not captured in the single-orbital Hubbard model, have been uncovered in multiorbital systems; for example, the colossal magnetoresistance and orbital orderings.

In §1.3.1 we explain the crystal-field effect on  $d$  orbitals. In §1.3.2 we examine some notable effects of interorbital interactions in a perturbation theory. We introduce a variety of multiorbital phenomena in real materials in §1.3.3, particularly taking  $\text{Ca}_{2-x}\text{Sr}_x\text{RuO}_4$  as a typical example.

### 1.3.1 $d$ orbitals in crystals

There is a five-fold degeneracy for the  $d$  electrons in a spherical field, according to the orbital angular momentum from  $l_z = -2$  to 2. The wave functions of the orbitals are

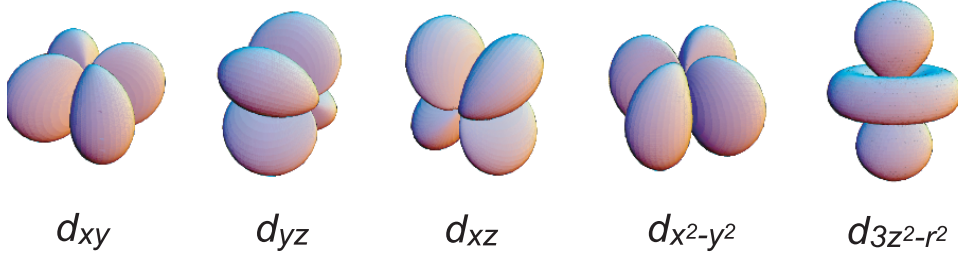


Figure 1.3: Five  $d$  orbitals are displayed with equi-amplitude contours.

$$\begin{aligned}
 \phi_{xy}(\mathbf{r}) &= \sqrt{\frac{15}{4\pi}} R(r) \frac{xy}{r^2}, \\
 \phi_{yz}(\mathbf{r}) &= \sqrt{\frac{15}{4\pi}} R(r) \frac{yz}{r^2}, \\
 \phi_{xz}(\mathbf{r}) &= \sqrt{\frac{15}{4\pi}} R(r) \frac{zx}{r^2}, \\
 \phi_{x^2-y^2}(\mathbf{r}) &= \sqrt{\frac{15}{16\pi}} R(r) \frac{x^2 - y^2}{r^2}, \\
 \phi_{3z^2-r^2}(\mathbf{r}) &= \sqrt{\frac{5}{16\pi}} R(r) \frac{3z^2 - r^2}{r^2},
 \end{aligned} \tag{1.2}$$

where  $r \equiv |\mathbf{r}| = \sqrt{x^2 + y^2 + z^2}$  and  $R(r)$  is a radial distribution function.  $R(r)$  for  $3d$  orbits is

$$\begin{aligned}
 R(r) &= \frac{4}{81\sqrt{30}} \left(\frac{Z}{a_0}\right)^{\frac{3}{2}} \rho^2 e^{-\frac{\rho}{3}}, \\
 \rho &\equiv \frac{Z}{a_0} r,
 \end{aligned} \tag{1.3}$$

where  $a_0$  is the Bohr radius and  $Z$  is the atomic number. The above  $d$  orbitals are schematically shown in Fig. 1.3. Hereafter we call these wave functions  $d_{xy}$ ,  $d_{yz}$ ,  $d_{xz}$ ,  $d_{x^2-y^2}$  and  $d_{3z^2-r^2}$ .

In crystals the degeneracy of the  $d$  orbitals is (partially) lifted due to the Coulomb potential from surrounding ions. How the degeneracy is lifted depends on a crystal structure. Here we consider the case that a crystal field has the cubic symmetry, that is, a transition-metal atom is surrounded by ions at the same distance in the  $\pm x$ ,  $\pm y$  and  $\pm z$  directions. This situation is realized in perovskite-type transition-metal oxides, where a transition metal is surrounded by six  $O^{2-}$  ions [Fig. 1.4(a)]. The cubic crystal field elevates the energy of  $d_{x^2-y^2}$  and  $d_{3z^2-r^2}$  orbitals, which are extending to the ligand oxygen ions, compared to that of  $d_{xy}$ ,  $d_{yz}$  and  $d_{xz}$  orbitals, which are extending in the direction

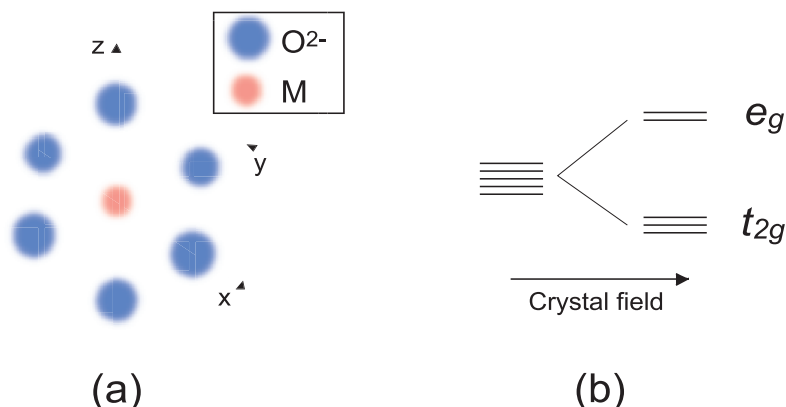


Figure 1.4: An example of a crystal-field effect in transition-metal oxides. (a) A scheme for a transition metal ion (M) surrounded by six oxygen ions. (b) Level scheme for the cubic crystal-field effect.

between the oxygen ions. Hence the five  $d$  orbitals split into a two-fold degenerate subset,  $e_g \equiv \{d_{x^2-y^2}, d_{3z^2-r^2}\}$ , and a three-fold degenerate subset,  $t_{2g} \equiv \{d_{xy}, d_{yz}, d_{xz}\}$  [Fig. 1.4(b)].

Since the energy split between  $e_g$  and  $t_{2g}$  is typically of order of 1 eV for  $3d$  transition-metal oxides, usually only one of the subsets,  $e_g$  or  $t_{2g}$ , crosses the Fermi energy.<sup>1</sup> In  $\text{SrVO}_3$ , for example,  $\text{V}^{4+}$  has only one  $d$  electron, so that only the  $t_{2g}$  bands traverses the Fermi energy and the  $e_g$  bands are empty. Therefore a model for low-energy phenomena in transition-metal oxides usually requires two or three orbitals.

In elemental transition metals such as Fe and Ni, however, the crystal-field effect is relatively small because of weak ionic potentials, so that the five  $d$  orbitals are almost degenerate and all the  $d$  bands are partially filled.

### 1.3.2 Coulomb-matrix elements between $d$ electrons

When we consider the  $d$ -orbital degrees of freedom, the on-site Coulomb interactions between  $d$  electrons are not characterized by a single parameter  $U$  as in the single-orbital Hubbard model. We introduce three parameters for the Coulomb interactions in multi-orbital systems<sup>2</sup> as

$U$ : between two electrons in the same orbital with antiparallel spins,

<sup>1</sup>In some materials, both  $e_g$  and  $t_{2g}$  bands are partially filled. A typical example is  $\text{LaMnO}_3$  (see §1.3.3), where Hund's coupling is larger than the crystal-field splitting so that the four  $d$  electrons occupy four different orbitals, i.e., three  $t_{2g}$  orbitals and one  $e_g$  orbital.

<sup>2</sup>We discriminate between 'multi-orbital' and 'multiband'. 'Multibands' derive from multiple atoms in the unit cell while 'multi-orbitals' derive from orbital degeneracy on one atom. The crucial difference is in the strength of interactions. In multi-orbital models the interorbital interactions are as strong as the intraorbital Coulomb interaction  $U$  while in multiband models intersite interactions are much weaker than the intrasite Coulomb interaction  $U$ . The strong interorbital interactions make multi-orbital problems much more difficult than multiband ones.

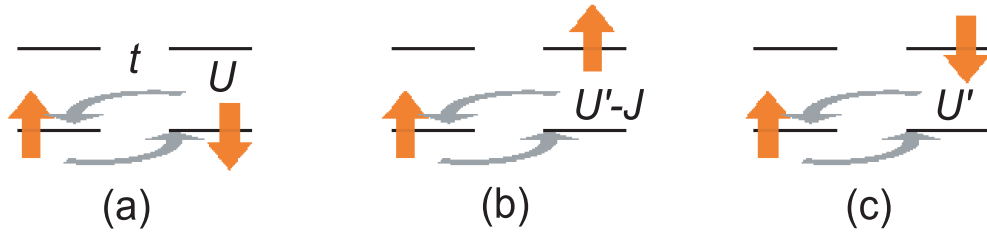


Figure 1.5: The kinetic exchange processes. The horizontal lines represent orbitals on each site, up and down arrows denote electron spins, and gray arrows virtual transfers.

$U'$ : between two electrons in different orbitals with antiparallel spins,

$U' - J$ : between two electrons in different orbitals with parallel spins.

We give more precise definition of  $U$ ,  $U'$  and  $J$  in §2.1.

Since overlaps of wave functions in different orbitals are smaller than those in the same orbital,  $U'$  is smaller than  $U$ . Also, because two electrons with parallel spins cannot occupy the same space due to the Pauli exclusion principle, the two electrons keep away from each other. This means that  $U' - J$  should be a weaker repulsion than  $U'$ , so that  $0 < J < U'$  is concluded. We can immediately see that the Hund coupling  $J$  favors on-site spin polarizations.<sup>3</sup>

The presence of the interorbital interactions,  $U'$  and  $J$ ,<sup>4</sup> makes multiorbital systems completely different from single-orbital systems. Although the above interactions are local (i.e., on site), they can affect bulk properties through electron transfers between sites. To obtain some intuitive picture for the effect, it is instructive to consider an effective interaction between neighboring electron spins in the strong coupling limit.

Considering a system with one electron per site in the strong coupling limit, we evaluate the energy reduction in the second-order perturbation with respect to the nearest-neighbor transfer  $t$  [57]. In single-orbital systems the effective interaction (kinetic exchange interaction) works antiferromagnetically on neighboring electron spins, since the electron transfer is possible only when the neighboring electrons have antiparallel spins. When we consider orbital degrees of freedom, the situation is completely changed. The simplest example is a two-orbital system with one electron per site (quarter filling) [57, 58]. When the electron on a neighboring site occupies the same orbital [Fig. 1.5(a)], the transfer is only allowed for antiparallel spins, then the second-order contribution to the total energy is

$$-\frac{t^2}{U}. \quad (1.4)$$

When the electron on a neighboring site occupies a different orbital, the second-order contribution is different for parallel and antiparallel spins: For a parallel spin [Fig. 1.5(b)]

<sup>3</sup>It has been pointed out that the reduction of the interaction energy between nuclei and electrons, which is not taken into account in the above discussion, is important to account for Hund's rule in real materials [55, 56].

<sup>4</sup>As we explain in §2.1, there is a relation  $U' = U - 2J$  for  $d$  orbitals when the crystal field has a cubic symmetry. In that case only two among  $U$ ,  $U'$  and  $J$  are independent parameters.

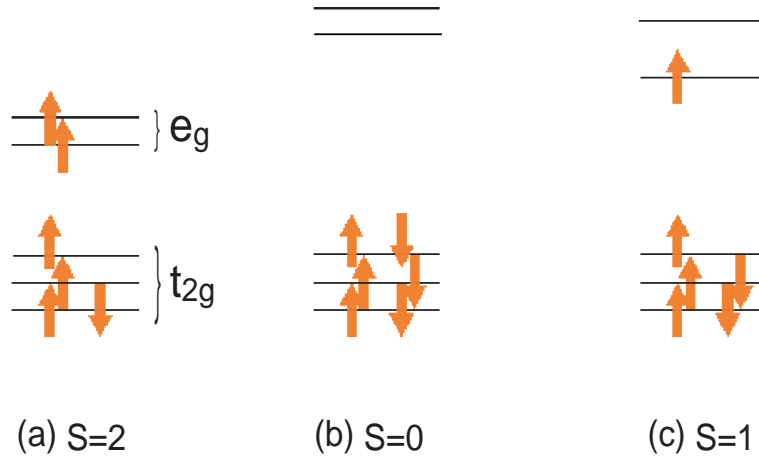


Figure 1.6: (a) The high-spin and (b) the low-spin states in  $\text{LaCoO}_3$  are schematically shown. (c) The intermediate-spin state suggested by Korotin *et al.* [59]

it is

$$-\frac{t^2}{U' - J}, \quad (1.5)$$

while for an antiparallel spin [Fig. 1.5(c)] it is

$$-\frac{t^2}{U'}. \quad (1.6)$$

These results mean that a neighboring electron tends to occupy a different orbital with a parallel spin [Fig. 1.5(b)]. Then, if a lattice is bipartite, a ferromagnetic order with antiferro-orbital ordering (i.e., electrons occupying two orbitals alternately) is expected for two-orbital systems at quarter filling. In fact, such orderings have been found in various numerical calculations for the double-orbital Hubbard model (see §5.1.2).

For general band fillings and for the interactions comparable to bandwidths, the above discussion does not apply straightforwardly. The effect of interorbital interactions is more involved there, and this provides various intriguing phenomena. We see such examples in Mott's transition, ferromagnetism and superconductivity in §3.3.

### 1.3.3 Example for real materials

Orbital degrees of freedom play important roles in most transition-metal-based materials.

The colossal negative magnetoresistance in manganites [3, 4, 5] is basically understood in terms of a strong Hund's coupling between  $d$  electrons. In manganites,  $\text{Mn}^{3+}$  has  $d^4$  configuration. Three of the  $d$  electrons occupy  $t_{2g}$  orbitals with a parallel spin and form a localized spin  $S = \frac{3}{2}$ , while the remaining one electron occupies one of the  $e_g$  orbitals, which are more dispersive than  $t_{2g}$  orbitals. The  $e_g$  electrons move around the crystal feeling a strong Hund's coupling to the localized  $t_{2g}$  spins. When a magnetic field is applied,

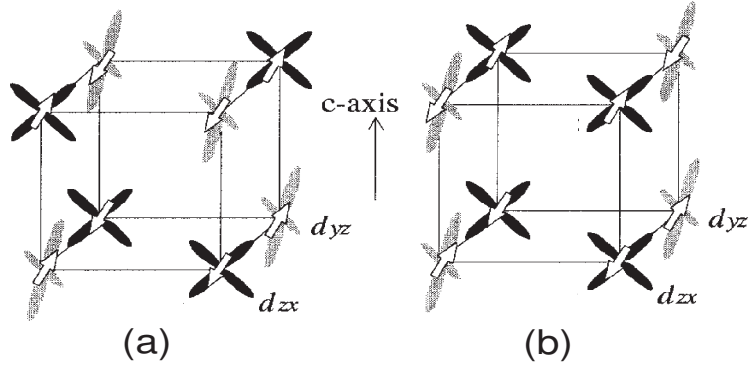


Figure 1.7: Schematic structures of spin and orbital ordered states in YVO<sub>3</sub>. (a) C-type spin ordering and G-type orbital ordering, (b) G-type spin ordering and C-type orbital ordering. Open arrows indicate spins and gray and black lobes indicate occupied  $d_{yz}$  and  $d_{zx}$  orbitals on vanadium ions, respectively. The commonly occupied  $d_{xy}$  orbital is not shown for clarity. (From Ref. [65].)

the localized  $t_{2g}$  spins are aligned in the direction of the field. Then the conducting  $e_g$  electrons can move in the crystal smoothly, which causes an extraordinary reduction of electronic resistance.

LaCoO<sub>3</sub> has a spin-state transition from a high-spin ( $S = 2$ ) state [Fig. 1.6(a)] at high temperatures ( $\gtrsim 100$  K) to a low-spin ( $S = 0$ ) state [(b)] at low temperatures ( $\lesssim 100$  K) [7, 8, 9]. This transition is caused by a competition of Hund's rule and level splitting by lattice distortions, which depends on temperature. At high temperatures, Hund's coupling is larger than the crystal-field splitting, so that the six  $d$  electrons at Co<sup>3+</sup> ion occupy the five spin-up states, and the remaining one electron occupies a spin-down state in the lower  $t_{2g}$  orbitals, then the  $S = 2$  state is realized. On the other hand, at low temperatures the lattice distortion changes and the crystal-field splitting exceeds Hund's coupling, so that the six  $d$  electrons fill the  $t_{2g}$  orbitals, then the total spin at Co<sup>3+</sup> disappears ( $S = 0$ ). Korotin *et al.* [59] suggested, based on an LDA+ $U$  calculation, that an intermediate-spin ( $S = 1$ ) state [Fig. 1.6(c)] exists between the high- and low-spin states. The possible existence of this state has been intensively discussed from both experimental and theoretical points of view [9], [59]-[62].

Orbital orderings have been found in many transition-metal oxides [6, 60], such as manganites [63], vanadates [64, 65, 66], and titanates [67, 68]. Orbital ordering sometimes accompanies a change of spin orders. Mott's insulator YVO<sub>3</sub> has two types of spin and orbital ordering patterns at low temperatures ( $T < 115$  K): Below 71 K the spin order is G-type antiferromagnetic (antiferromagnetic along the  $a, b, c$  axes) while the orbital order is C type (antiferro-orbital order in the  $ab$  plane and ferro-orbital order along the  $c$  axis) [Fig. 1.7(a)] [64, 65, 69]. For  $71 \text{ K} < T < 115 \text{ K}$  the order changes to C type for spin and into G type for orbitals [Fig. 1.7(b)]. The band calculation with the local spin-density approximation cannot explain the band gap of YVO<sub>3</sub>. While the generalized gradient approximation provides a band gap, it cannot explain the G-type spin ordering

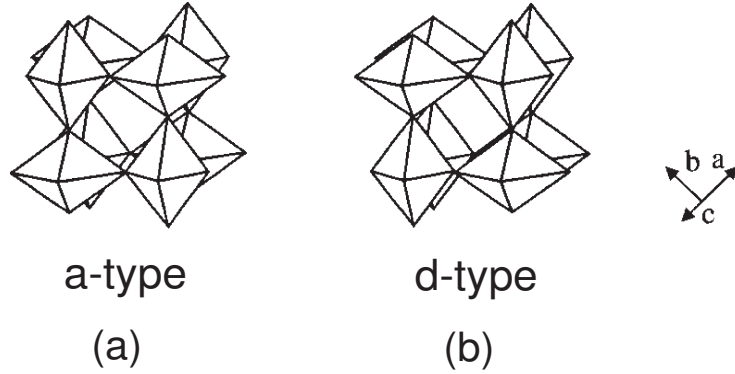


Figure 1.8: Two types of lattice distortion in  $\text{YVO}_3$  (after Ref. [60]).

in the ground state [66]. A realistic Hartree-Fock calculation by Mizokawa and Fujimori [60] reproduced the band gap, as well as the G-type antiferromagnetic ground state on the assumption of d-type distortion of the lattice [Fig. 1.8(b)], which is experimentally observed. However, the a-type distortion [Fig. 1.8(a)] is more favored than the d-type one in the Hartree-Fock calculation, in contradiction to the real structure. Also the calculated band gap is larger by 1-2 eV than the experimental values. These results indicate significant correlation effects.

The unconventional superconductor  $\text{Na}_x\text{CoO}_2 \cdot y\text{H}_2\text{O}$  has also been studied as a multi-orbital system. Mochizuki *et al.* [73] and Yanase *et al.* [74] implemented the fluctuation-exchange and a perturbative calculations for the multiorbital Hubbard model with a realistic bandstructure, and suggested that a spin-triplet superconductivity can be realized due to Hund's coupling. While some Knight shift data [70] imply a triplet pairing, the symmetry of the Cooper pair is still controversial both in experiments [71, 72] and in theories [73]-[77].

$\text{Ca}_{2-x}\text{Sr}_x\text{RuO}_4$  has also drawn much interest on the roles of orbital degrees of freedom.  $\text{Ca}_{2-x}\text{Sr}_x\text{RuO}_4$  has a single-layered perovskite structure [Fig. 1.9(a)], where Ru- $d$  bands split into  $e_g$  and  $t_{2g}$  bands due to the crystal-field effect. The four  $d$  electrons at  $\text{Ru}^{4+}$  occupy the lower  $t_{2g}$  orbitals, where the Hund coupling aligns three of the four electron spins and remaining one electron has the opposite spin [see Fig. 1.9(b)].

A phase diagram experimentally obtained by Nakatsuji *et al.* [79] is shown in Fig. 1.10. In the following we explain the phase diagram in detail, as an introduction to multiorbital systems, as well as to the LDA+DMFT calculation for  $\text{Sr}_2\text{RuO}_4$  implemented in Chap. 6.

At  $x = 2$  ( $\text{Sr}_2\text{RuO}_4$ ) the material shows a spin-triplet superconductivity at low temperatures ( $T_c \sim 1$  K) [2, 78]. Above the transition temperature the material is a paramagnetic metal. The superconductivity disappears with a slight Ca doping, and  $\text{Ca}_{2-x}\text{Sr}_x\text{RuO}_4$  is a paramagnetic metal for  $0.7 < x < 2$ .

Around  $x = 0.5$  there is a ferromagnetic cluster glass phase at low temperatures. The phase has no long-range order, but has a ferromagnetic short-range order, which forms clusters.

$0.2 < x < 0.4$  is a metallic region with an antiferromagnetic correlation. In this region



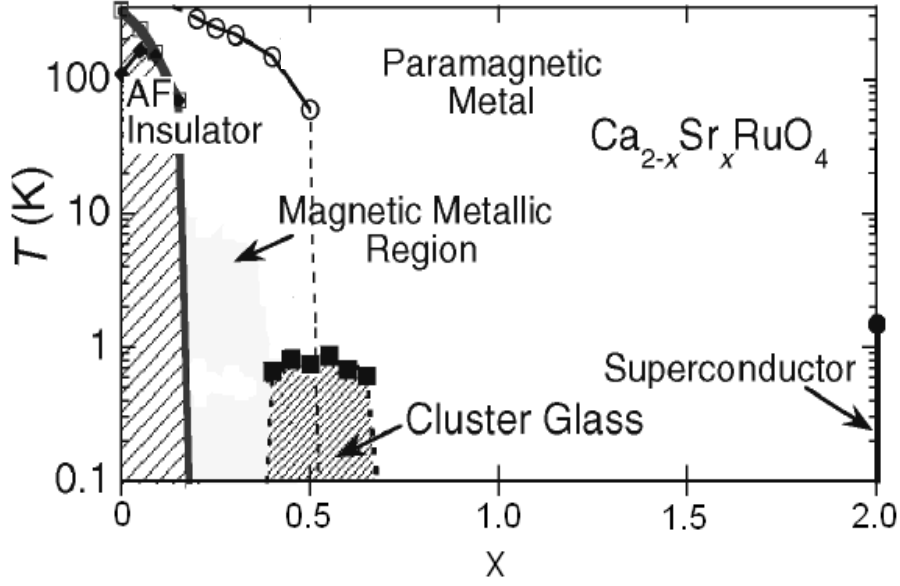


Figure 1.10: Phase diagram for  $\text{Ca}_{2-x}\text{Sr}_x\text{RuO}_4$ , experimentally obtained by Nakatsuji *et al.* [79]

while the  $d_{xy}$  orbital is band-insulating [82, 83]. The scenario, however, conflicts with the X-ray absorption measurement by Mizokawa *et al.* [84], which indicates that  $n_{xy} : (n_{xz} + n_{yz}) = 1 : 3$  ( $n_a$  is the electron number per site in orbital  $a$ ) at 300 K and  $n_{xy} : (n_{xz} + n_{yz}) = \frac{3}{2} : \frac{5}{2}$  at 90 K. While Mizokawa *et al.* discussed the result in terms of the spin-orbit interaction, Hotta and Dagotto [85] proposed an orbital ordered state with  $n_{xy} : (n_{xz} + n_{yz}) = \frac{3}{2} : \frac{5}{2}$  stabilized by electron-electron and electron-lattice couplings. However, the lattice distortion corresponding to the orbital order has not been observed in experiments. Fang *et al.* [86] emphasized, based on a first-principles calculation, the importance of the two-dimensional feature of the crystal field, which derives from the layered structure of  $\text{Ca}_2\text{RuO}_4$ , on the stability of the  $\frac{3}{2} : \frac{5}{2}$  configuration. Thus the ground state of  $\text{Ca}_2\text{RuO}_4$  is still controversial.

· *Paramagnetic metal* ( $0.7 < x < 2$ ) and *ferromagnetic cluster glass* ( $0.4 < x < 0.7$ )

The appearance of the ferromagnetic cluster glass phase around  $x = 0.5$  is expected to be related with a structural change at this filling: From  $x = 2$  to  $x = 0.5$ ,  $\text{RuO}_6$  octahedron rotates around the  $c$  axis, without any tilt of the basal plane, by up to  $\phi \sim 12^\circ$  at  $x = 0.5$  [Fig. 1.11(b)], while at  $x = 0.5$  it starts to tilt around an axis in the  $ab$  plane up to  $\theta \sim 12^\circ$  at  $x = 0$ , keeping  $\phi \sim 12^\circ$  [Fig. 1.11(c)].

Here we consider an interaction (superexchange interaction) between neighboring Ru- $d$  electrons through the  $pd\pi$  hybridizations with O- $p$  orbitals [87]. At  $x = 2$  the material has no rotational distortion [Fig. 1.11(a)], so that the superexchange interaction exists only between the same  $d$  orbitals, which works antiferromagnetically. As  $x$  decreases, the rotation of  $\text{RuO}_6$  octahedra increases [Fig. 1.11(b)]. Then the antiferromagnetic interaction decreases due to the reduction of the  $d$ - $p$  hybridizations while a ferromagnetic superex-

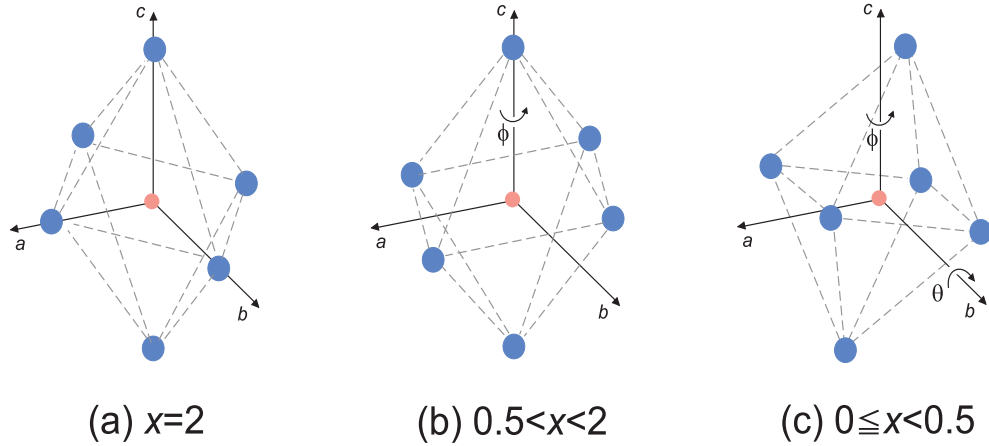


Figure 1.11: The distortions of a  $\text{RuO}_6$  octahedron in  $\text{Ca}_{2-x}\text{Sr}_x\text{RuO}_4$ . (a) Undistorted structure in  $\text{Sr}_2\text{RuO}_4$ . (b) Rotational distortion around the  $c$  axis ( $\phi$ ) for  $0.5 < x < 2$ . (c) Rotational distortion ( $\phi$ ) + tilt ( $\theta$ ) of the basal plane for  $0 \leq x < 0.5$ .

change interaction appears between neighboring  $d_{xy}$  orbitals through the Hund coupling at oxygen site. This may be a reason for the increasing ferromagnetic fluctuation down to  $x = 0.5$ .

· *Antiferromagnetic metallic region* ( $0.2 < x < 0.4$ )

When the tilt of the octahedra is introduced below  $x = 0.4$ , the  $pd\pi$  hybridizations are significantly reduced, then the  $t_{2g}$  bands become narrower. For the antiferromagnetic metallic region ( $0.2 < x < 0.4$ ), Anisimov *et al.* [83] proposed a novel phase where the  $d_{xz,yz}$  orbitals are Mott insulating with antiferromagnetic correlations while the  $d_{xy}$  orbital is metallic. This idea is based on the observation that  $d_{xy}$  band is wider than  $d_{xz,yz}$  bands because of the quasi-two-dimensional feature of the crystal structure (for more detail, see §6.2). Their proposition fuelled intensive studies for Mott's transition in multiorbital systems (see §3.3.4). However, it has still been controversial whether such a coexistence of metallic and Mott-insulating bands can be realized in the present material. Indeed, there are some experiments against Anisimov's picture; a polarized neutron diffraction experiment [88] indicates a larger magnetic moment for the wider  $d_{xy}$  orbital than that for the narrower  $d_{xz}, d_{yz}$  orbitals, and an optical conductivity analysis [89] suggests a larger effective mass for  $d_{xy}$  quasiparticles than that for  $d_{xz}, d_{yz}$  ones. These experiments imply that the  $d_{xy}$  orbital is more localized than the  $d_{xz,yz}$  orbitals, in conflict with Anisimov's picture. While more detailed researches are needed for the region  $0.2 < x < 0.4$  in  $\text{Ca}_{2-x}\text{Sr}_x\text{RuO}_4$ , Anisimov's proposal opened a new avenue for orbital-dependent physics.

## 1.4 Motivation and outline

The orbital degrees of freedom can be a key factor for understanding the diverse properties of transition-metal-based materials since the orbital degrees of freedom are involved

in most of the materials. In particular, Hund's coupling, which is directly related to the spin degrees of freedom, makes multiorbital physics substantially different from the one in single-orbital systems. However, the complexity of multiorbital systems has hampered theoretical studies, especially for intermediate-coupling ( $U \sim W$ ) regions with finite Hund's coupling, which are realized in transition metals and transition-metal oxides. Hence a development of reliable and efficient theoretical methods for multiorbital systems has a general importance, and many significant issues remain open in multiorbital systems.

In this thesis we investigate electron correlation problems in multiorbital systems, where our main interest is in the *role of Hund's coupling*. However, conventional schemes have difficulties in treating multiorbital systems, in particular in the presence of Hund's coupling. For example, the exact diagonalization method cannot treat large systems, therefore its application has been restricted to one-dimensional two-orbital systems. While the conventional quantum Monte Carlo (QMC) method can treat larger systems than the exact diagonalization method, the QMC method suffers from a severe negative sign problem (see §4.3) in the presence of Hund's coupling.

Here we develop a novel QMC method (Chap. 4) for multiorbital systems with the Hund coupling, and combine the algorithm with the dynamical mean-field theory (DMFT) (Chap. 3) to solve the problem in the thermodynamic limit. An important point of the present method is that it can treat spin-SU(2) symmetric Hund's coupling and the pair-hopping interaction, which are needed for *preserving spin and orbital rotational symmetries* in the multiorbital Hubbard Hamiltonian (see §2.1). Most of DMFT+QMC studies for multiorbital systems so far have only taken account of the  $z$  (Ising) component of Hund's coupling and neglected the  $x, y$  components and the pair-hopping interaction (§2.2), because the conventional Hirsch-Fye QMC method (§4.1) has difficulties in treating the  $x, y$  components of Hund's coupling and the pair-hopping interaction (§4.2). However, this treatment has no physical ground, and violates the spin and orbital rotational symmetries of the Hamiltonian. Our QMC method overcomes these difficulties.

Another important point in the present QMC method is that it is formulated for *general number of orbitals* while it has been difficult to formulate the conventional QMC method for more than two-orbital systems in the presence of SU(2)-symmetric Hund's coupling (§4.2, 4.5). Since there are many materials that involve more than two orbitals, such as  $t_{2g}$  orbitals in ruthenates and cobaltates, the present method has a wide applicable scope.

With the method we examine *itinerant ferromagnetism in multiorbital systems* (Chap. 5). Although importance of the orbital degrees of freedom, especially of Hund's coupling, on ferromagnetism has been discussed for a long time, most researches concentrate on the ferromagnetic *insulator* with an antiferro-orbital order in two-orbital models at quarter filling. Our interest is in the role of Hund's coupling in *itinerant ferromagnetism*, which is realized in transition metals and their compounds.

There are a large number of studies for itinerant ferromagnetism in the single-orbital Hubbard model, where lattice structure is a crucial factor for stabilizing the ferromagnetism. On the other hand, the importance of Hund's coupling has been pointed out for a long time, where most studies have been restricted to one-dimensional systems or to

drastic approximations e.g., strong-coupling limit. Our method allows for taking account of both lattice structure and Hund's coupling at the same time. Thereby we discuss a long standing issue; *whether ferromagnetism in transition-metal-based materials is attributed to either of lattice structure or Hund's coupling* (§5.3).

We also discuss the importance of spin-SU(2) symmetry of Hund's coupling (§5.2), by comparing the result with SU(2)-type Hund's coupling to that with Ising-type Hund's coupling, which has been extensively employed in studies for multiorbital systems.

In Chapter 6 we demonstrate that the present algorithm can be applied to the local density approximation (LDA) + DMFT for a three-orbital system,  $\text{Sr}_2\text{RuO}_4$ , where our aim is to compare the spectra between SU(2)- and Ising-type Hund's couplings, as well as to show the applicability of the present method. Since the Ising treatment of Hund's coupling has also been adopted extensively in recent LDA+DMFT studies, it is important to know how a spectrum changes when we take into account the spin and orbital rotational symmetries. We also discuss the importance of correlation effects in  $\text{Sr}_2\text{RuO}_4$ , by comparing the calculated results with experimental data.

# Chapter 2

## The multiorbital Hubbard model

### 2.1 Formulation

Theoretical study of multiorbital systems began to unfold with the proposal of the multiorbital Hubbard model<sup>1</sup> by Roth [58]. The model takes into account Hund's exchange coupling as well as the intra- and interorbital Coulomb interactions. However, the original model proposed by Roth omits some two-electron interactions such as the pair-hopping interaction and violates the real-space rotational symmetry of  $d$  orbitals.

The first systematic derivation of the multiorbital Hubbard model was done by Oleś [90]. We consider a general  $d$ -electron system such as a transition metal and a transition-metal oxide. In such a material, relatively narrow  $d$  bands and more dispersive  $s, p$  conduction bands cross the Fermi energy  $E_F$ . In order to construct an effective model for a low-energy region ( $E$  around  $E_F$ ), we use Wannier functions as the basis.<sup>2</sup> We concentrate on low-energy degrees of freedom, which cut across the Fermi level, and take account of contributions from orbitals below or above  $E_F$  only via the one-body potential for the electrons in focus and via a screening of the Coulomb interaction between the electrons.

Then a second-quantized Hamiltonian for the low-energy electrons is

$$\begin{aligned}\hat{H} &= \sum_{\sigma} \int d\mathbf{x} \psi_{\sigma}^{\dagger}(\mathbf{x}) \left[ -\frac{1}{2m} \nabla^2 + V_1(\mathbf{x}) \right] \psi_{\sigma}(\mathbf{x}) \\ &+ \frac{1}{2} \sum_{\sigma, \sigma'} \int d\mathbf{x} d\mathbf{x}' \psi_{\sigma}^{\dagger}(\mathbf{x}) \psi_{\sigma'}^{\dagger}(\mathbf{x}') V_2(\mathbf{x} - \mathbf{x}') \psi_{\sigma'}(\mathbf{x}') \psi_{\sigma}(\mathbf{x}),\end{aligned}\quad (2.1)$$

where  $\psi_{\sigma}(\mathbf{x})$  is the field operator for the electrons with a spin  $\sigma$ ,  $V_1(\mathbf{x})$  is the one-body potential composed of the ionic potentials, and  $V_2(\mathbf{x})$  is the electron-electron interaction screened by other electrons. Although  $V_2$  may depend on spins of the two electrons in general, that is, the screened Coulomb interaction may have a form  $V_2 + \sigma \cdot \sigma' V_3$ , we assume here that the spin-dependent part ( $V_3$ ) is small.

<sup>1</sup>We emphasize that the *multiorbital* model differs from *multiband* models, where the unit cell includes multiple atoms and intersite interactions are very weak. See the first footnote in §1.3.2.

<sup>2</sup>We assume that the Wannier functions in the low-energy region mainly consist of  $d$  orbitals, with a small mixture with  $s$  and  $p$  orbitals.

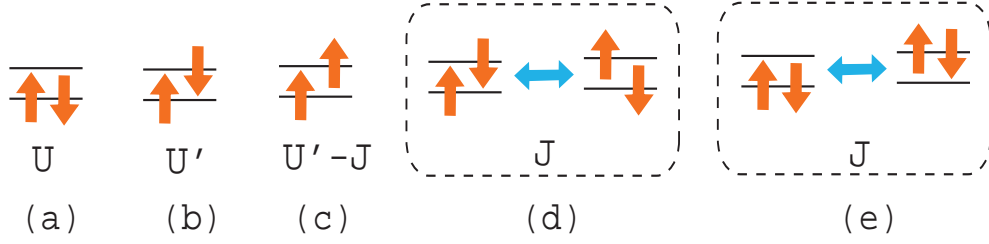


Figure 2.1: Electron-electron interactions in multiorbital systems; (a) intraorbital Coulomb interaction, (b)(c) interorbital Coulomb interactions, (d) spin-flip process, (e) pair-hopping process.

To obtain a tight-binding model we expand the operator  $\psi_\sigma(\mathbf{x})$  in terms of the low-energy Wannier orbitals at lattice sites  $i$ , that is,

$$\psi_\sigma(\mathbf{x}) = \sum_{im} \phi_{im}(\mathbf{x}) c_{im\sigma}, \quad (2.2)$$

where  $\phi_{im}(\mathbf{x})$  is the wave function of the  $m$ -th Wannier orbital at site  $i$ , and  $c_{im\sigma}$  the corresponding annihilation operator.

Here we define the hopping integral  $t_{ij}^{mm'}$  and the orbital-dependent on-site potential  $\mu_m$  as

$$t_{ij}^{mm'} (1 - \delta_{ij}) - \mu_m \delta_{mm'} \delta_{ij} \equiv \int d\mathbf{x} \phi_{im}^*(\mathbf{x}) \left[ -\frac{1}{2m} \nabla^2 + V_1(\mathbf{x}) \right] \phi_{jm'}(\mathbf{x}), \quad (2.3)$$

and the intrasite-interaction integrals,

$$\begin{aligned} U_{mm'} &\equiv \int d\mathbf{x} d\mathbf{x}' |\phi_{im}(\mathbf{x})|^2 V_2(\mathbf{x} - \mathbf{x}') |\phi_{im'}(\mathbf{x}')|^2, \\ J_{mm'} &\equiv \int d\mathbf{x} d\mathbf{x}' \phi_{im}^*(\mathbf{x}) \phi_{im'}^*(\mathbf{x}') V_2(\mathbf{x} - \mathbf{x}') \phi_{im}(\mathbf{x}') \phi_{im'}(\mathbf{x}) \quad (m \neq m'), \\ J'_{mm'} &\equiv \int d\mathbf{x} d\mathbf{x}' \phi_{im}^*(\mathbf{x}) \phi_{im}^*(\mathbf{x}') V_2(\mathbf{x} - \mathbf{x}') \phi_{im'}(\mathbf{x}') \phi_{im'}(\mathbf{x}) \quad (m \neq m'). \end{aligned} \quad (2.4)$$

We neglect the intersite interactions, which are expected to be much smaller than the intrasite ones because of the locality of low-energy Wannier orbitals. We assume hereafter that the Wannier functions hold  $d$ -orbital characters, namely the Wannier functions approximate spherical harmonic functions. Then the intrasite-interaction integrals other than  $U_{mm'}$ ,  $J_{mm'}$ , and  $J'_{mm'}$  can be shown to be zero due to the axial symmetry of  $d$  orbits.

With the above parameters the second term in Eq. (2.1) is written as

$$\begin{aligned}
& \sum_{i,m} U_{mm} n_{im\uparrow} n_{im\downarrow} \\
& + \sum_{i,m < m', \sigma} [U_{mm'} n_{im\sigma} n_{im', -\sigma} + (U_{mm'} - J_{mm'}) n_{im\sigma} n_{im'\sigma}] \\
& + \sum_{i,m \neq m'} J_{mm'} c_{im\uparrow}^\dagger c_{im'\downarrow}^\dagger c_{im\downarrow} c_{im'\uparrow} \\
& + \sum_{i,m \neq m'} J'_{mm'} c_{im\uparrow}^\dagger c_{im'\downarrow}^\dagger c_{im\downarrow} c_{im'\uparrow}
\end{aligned} \tag{2.5}$$

with  $n_{im\sigma} \equiv c_{im\sigma}^\dagger c_{im\sigma}$ . The first term expresses the Coulomb interaction between two electrons in the same orbital with opposite spins [Fig. 2.1(a)]. The second term is the Coulomb interaction between two electrons in different orbitals with opposite and parallel spins, including the  $z$  component of Hund's coupling ( $J_{mm'}$ ) [Fig. 2.1(b)(c)]. The third term is the  $x$  and  $y$  components of Hund's exchange, and is called the spin-flip term [Fig. 2.1(d)]. The last term is the pair-hopping term, which expresses two-electron transfers from an orbital to other orbitals [Fig. 2.1(e)].

We specifically consider  $d$  orbitals in a cubic lattice. Due to crystal-field effects, the five  $d$  orbitals split into three-fold degenerate orbitals ( $t_{2g}$ ) and two-fold degenerate orbitals ( $e_g$ ), so that we can usually construct a model for one of the sets of these degenerate orbitals. Since the degenerate orbitals are equivalent, the Coulomb and exchange interactions become orbitally independent, i.e.,

$$\begin{aligned}
U_{mm} & \equiv U, \\
U_{mm'} & \equiv U' \quad \text{for } m \neq m', \\
J_{mm'} & = J'_{mm'} \equiv J \quad \text{for } m \neq m',
\end{aligned} \tag{2.6}$$

where  $J_{mm'} = J'_{mm'}$  holds when the Wannier functions are taken to be real as for  $d$  orbitals. Further, since the equivalent  $d$  orbitals are interchanged with each other by rotations in real space, an additional condition,

$$U = U' + 2J, \tag{2.7}$$

should hold. Typical values of  $U$  and  $J$  are

$$\begin{aligned}
U & \sim 4 - 6 \text{ eV}, \\
J & \sim 0.5 - 0.7 \text{ eV}
\end{aligned} \tag{2.8}$$

for  $3d$  transition metals and transition-metal oxides, and somewhat smaller values ( $U \sim 1-3$  eV) are expected for  $4d$  transition-metal systems such as ruthenates. These values are experimentally estimated from Auger-electron [91, 92] and photoemission spectroscopy [93], and also theoretically from constrained LDA (local density approximation) calcu-

lations [94]-[99], which is the LDA with a constraint on the number of  $d$  electrons at a site.<sup>3</sup>

Thus we end up with the multiorbital tight-binding Hubbard Hamiltonian,

$$\begin{aligned}
\hat{H} &= \hat{H}_0 + \hat{H}_{\text{int}}, \\
\hat{H}_0 &= \sum_{ij} \sum_{mm'\sigma} t_{ij}^{mm'} c_{im\sigma}^\dagger c_{jm'\sigma} - \sum_{im\sigma} \mu_m n_{im\sigma}, \\
\hat{H}_{\text{int}} &= U \sum_{im} n_{im\uparrow} n_{im\downarrow} + \sum_{i,m<m',\sigma} [U' n_{im\sigma} n_{im'\sigma} + (U' - J) n_{im\sigma} n_{im'\sigma}] \\
&\quad + J \sum_{i,m<m'} (c_{im\uparrow}^\dagger c_{im'\downarrow}^\dagger c_{im\downarrow} c_{im'\uparrow} + c_{im\downarrow}^\dagger c_{im'\uparrow}^\dagger c_{im\uparrow} c_{im'\downarrow} + \text{H.c.}). \tag{2.9}
\end{aligned}$$

The first term in  $\hat{H}_{\text{int}}$  is the intraorbital Coulomb interaction, and the second term the interorbital Coulomb interactions including Ising ( $z$ ) component of Hund's coupling. The last term is the spin-flip and pair-hopping interactions.

The spin-rotational invariance of the Hamiltonian (2.9) can be seen explicitly if we rewrite the interaction part as

$$\begin{aligned}
\hat{H}_{\text{int}} &= \frac{U}{2} \sum_i \left[ \left( \sum_m n_{im} \right)^2 - \sum_m n_{im} \right] - \frac{5}{2} J \sum_{i,m<m'} n_{im} n_{im'} \\
&\quad - 2J \sum_{i,m<m'} \hat{\mathbf{S}}_{im} \cdot \hat{\mathbf{S}}_{im'} + \frac{J}{2} \sum_{i,m \neq m'} \left( \sum_{\sigma} c_{im\sigma}^\dagger c_{im'\sigma} \right)^2, \tag{2.10}
\end{aligned}$$

where  $n_{im} \equiv \sum_{\sigma} n_{im\sigma}$  is the on-site number operator for orbital  $m$  and  $\hat{\mathbf{S}}_{im} \equiv (\hat{S}_{im}^x, \hat{S}_{im}^y, \hat{S}_{im}^z)$  is the on-site spin operator for orbital  $m$ , defined by

$$\hat{S}_{im}^a \equiv \frac{1}{2} \sum_{ss'} c_{ims}^\dagger \sigma_{ss'}^a c_{ims'} \quad \text{for } a = x, y, z, \quad \sigma : \text{Pauli matrix.} \tag{2.11}$$

## 2.2 Hund's coupling

We stress here that the above derivation of the multiorbital Hubbard model (2.9) naturally conduces to SU(2)-symmetric Hund's spin-spin coupling,

$$-2J \hat{\mathbf{S}}_{im} \cdot \hat{\mathbf{S}}_{im'}. \tag{2.12}$$

However, Hund's coupling has often been treated as an Ising type,

$$-2J \hat{S}_{im}^z \hat{S}_{im'}^z = -\frac{J}{2} \sum_{\sigma\sigma'} \sigma\sigma' n_{im\sigma} n_{im'\sigma'}, \tag{2.13}$$

<sup>3</sup>Recent calculations [100, 101, 102] based on the *ab initio* random phase approximation [100, 103] suggest substantially smaller  $U$  ( $\sim 2$ -4 eV) for 3d transition metals. So values of  $U$  for real materials are still controversial.

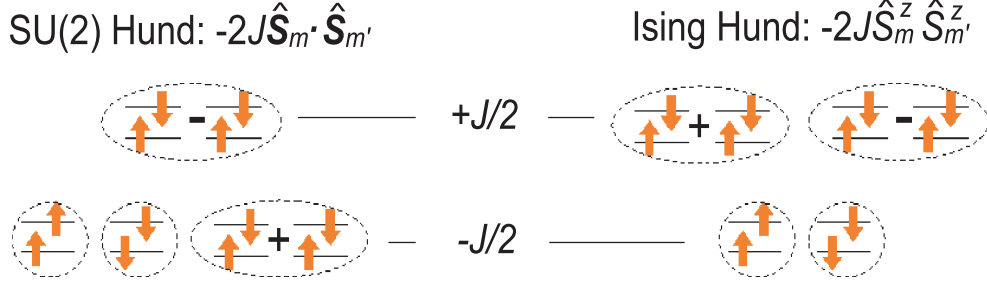


Figure 2.2: Level scheme for the two-electron energy states in multiorbital systems coupled with SU(2)- or Ising-Hund's exchange interaction.

especially in quantum Monte Carlo studies, because the part,  $-2J(\hat{S}_{im}^x \hat{S}_{im'}^x + \hat{S}_{im}^y \hat{S}_{im'}^y)$ , in (2.12), which cannot be written as a density-density coupling, is intractable in the conventional quantum Monte Carlo algorithm. Although the Ising treatment of Hund's coupling has been widely employed, there is no physical basis to justify it.

In fact, the most fatal defect of this treatment is the neglect of quantum fluctuations. For example, when we consider the two-electron states at a site  $i$ , SU(2) Hund lowers the energy of the spin-triplet states,

$$\begin{aligned}
& c_{im\uparrow}^\dagger c_{im'\uparrow}^\dagger, \\
& c_{im\downarrow}^\dagger c_{im'\downarrow}^\dagger, \\
& \frac{1}{\sqrt{2}}(c_{im\uparrow}^\dagger c_{im'\downarrow}^\dagger + c_{im'\uparrow}^\dagger c_{im\downarrow}^\dagger) \quad (m \neq m'), \tag{2.14}
\end{aligned}$$

compared with the singlet state,

$$\frac{1}{\sqrt{2}}(c_{im\uparrow}^\dagger c_{im'\downarrow}^\dagger - c_{im'\uparrow}^\dagger c_{im\downarrow}^\dagger) \quad (m \neq m'), \tag{2.15}$$

while Ising Hund lowers the doublet,  $c_{im\uparrow}^\dagger c_{im'\uparrow}^\dagger$  and  $c_{im\downarrow}^\dagger c_{im'\downarrow}^\dagger$  compared with the other doublet  $\frac{1}{\sqrt{2}}(c_{im\uparrow}^\dagger c_{im'\downarrow}^\dagger \pm c_{im'\uparrow}^\dagger c_{im\downarrow}^\dagger)$  (Fig. 2.2). This causes not only quantitative but qualitative differences in the low-energy physics.

For example, Pruschke and Bulla showed that the criticality of Mott's metal-insulator transition is different between SU(2) and Ising Hund's couplings [104]. They investigated ground-state property around Mott's transition in the half-filled two-orbital Hubbard model, using the dynamical mean-field theory (DMFT) + numerical renormalization-group method with an orbitally-asymmetric truncation scheme (see §3.5). Their calculation for the mass renormalization factor and for the local spin moment indicates that the Mott transition is first order in Ising case while it is continuous in SU(2) case (Fig. 2.3).

In Chapter 4 we develop a quantum Monte Carlo method which can handle the full interaction  $\hat{H}_{\text{int}}$ , including the spin-flip and pair-hopping interactions. With the method we demonstrate that a significant difference exists for ferromagnetic instability between Ising and SU(2) Hund's couplings in §5.2. We also show a remarkable difference in

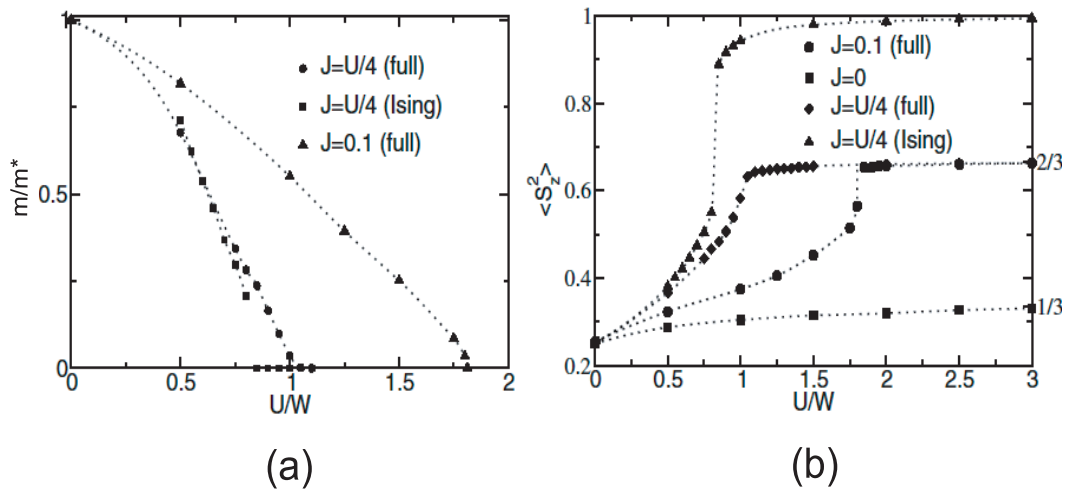


Figure 2.3: The behavior of (a) the mass renormalization factor and of (b) the local moment against  $U/W$  ( $U$ : intrasite Coulomb interaction,  $W$ : bandwidth) around Mott's transition in the half-filled two-orbital Hubbard model with  $SU(2)$ (full) and Ising Hund's couplings  $J = 0, 0.1$ , and  $U/4$  (after Ref. [104]).

quasiparticle spectra between the two treatments for a three-orbital system,  $Sr_2RuO_4$ , in §6.4.1.

# Chapter 3

## The dynamical mean-field theory

The dynamical mean-field theory (DMFT) is one of the most successful methods for investigating the physics of strongly correlated electron systems [18]. The DMFT gives the exact electron self-energy in the limit of infinite spatial dimensions in a self-consistent way. For finite dimensions, it gives an approximate solution which neglects spatial fluctuations. However, it takes full account of temporal fluctuations, so that it becomes a good approximation in the case where the spatial fluctuations are not important; for example, systems with large coordination numbers.

In the DMFT, lattice models, such as the Hubbard model, are mapped onto an effective impurity model which includes the same on-site interactions on an impurity site and an infinite number of bath sites which are coupled to the impurity site through a hybridization (hopping). The impurity model is solved in a self-consistent way. Although the impurity problem is much more tractable than the original lattice model, it still requires a reliable numerical solver.

We review the general formalism of the DMFT and its applications to the single- and multiorbital Hubbard models in §3.1-3.3. Applications to real materials are reviewed in §3.4. In §3.5 we compare various DMFT solvers developed so far.

### 3.1 General formalism

The partition function  $Z$  of an electron system is written with the Grassmann variables, which are a set of c-numbers with an anticommutation relation, as

$$\begin{aligned} Z &= \int \prod_i Dc_i^\dagger Dc_i e^{-S}, \\ S &= \int_0^\beta d\tau \left( \sum_i c_i^\dagger(\tau) \partial_\tau c_i(\tau) - \hat{H}[c^\dagger(\tau), c(\tau)] \right), \end{aligned} \quad (3.1)$$

where  $\hat{H}$  is the Hamiltonian of the system,  $S$  is the action,  $\beta$  is the inverse temperature, and  $c^\dagger, c$  are the Grassmann variables.  $\int Dc$  means the integration over all the path of  $c(\tau)$  along the imaginary time  $\tau$ .

Integrating out all the degrees of freedom except for a representative site  $o$  (called the impurity), we can define the effective action  $S_{\text{eff}}$  as

$$\frac{1}{Z_{\text{eff}}} e^{-S_{\text{eff}}[c_o^\dagger, c_o]} \equiv \frac{1}{Z} \int \prod_{i \neq o} Dc_i^\dagger Dc_i e^{-S}, \quad (3.2)$$

$$Z_{\text{eff}} \equiv \int Dc_o^\dagger Dc_o e^{-S_{\text{eff}}}.$$

In this section we describe the DMFT for the single-orbital Hubbard Hamiltonian,

$$\hat{H} = t \sum_{ij\sigma} c_{i\sigma}^\dagger c_{j\sigma} - \mu \sum_{i\sigma} n_{i\sigma} + U \sum_i n_{i\uparrow} n_{i\downarrow}, \quad (3.3)$$

for simplicity, while more complex lattice fermion models can be discussed in a similar way.

Metzner and Vollhardt [105] first pointed out that lattice fermion models have a non-trivial limit of large spatial dimension  $d \rightarrow \infty$ , when one scales the transfer  $t$  as  $t \sim d^{-\frac{1}{2}}$ . In this limit, the fourth or higher order terms in the fermion operators in the effective action  $S_{\text{eff}}$  can be neglected, since they are higher order in  $d^{-1}$ . Hence we can write the effective action in a form

$$S_{\text{eff}} = - \int_0^\beta d\tau \int_0^\beta d\tau' \sum_\sigma c_{o\sigma}^\dagger(\tau) [g_{0\sigma}(\tau - \tau')]^{-1} c_{o\sigma}(\tau') + U \int_0^\beta d\tau n_{o\uparrow}(\tau) n_{o\downarrow}(\tau), \quad (3.4)$$

where  $[g_{0\sigma}(\tau - \tau')]^{-1}$  is the mean-field (Weiss) function that includes retarded effects from local quantum fluctuations [20, 106, 107].

It is much easier to solve this impurity model than to solve the original model defined on a lattice. We have several numerically exact solvers to the impurity problem: The quantum Monte Carlo method and the exact diagonalization, etc. We will discuss these methods in §3.5.

After we solve the impurity problem and obtain the electron self-energy, we come back to the original lattice model. Because the electron self-energy  $\Sigma$  has no  $\mathbf{k}$  dependence in the infinite-dimension limit [108], Green's function for the interacting electron becomes

$$G_\sigma(\mathbf{k}, i\omega_n) = \{[g_\sigma(\mathbf{k}, i\omega_n)]^{-1} - \Sigma_\sigma(i\omega_n)\}^{-1}, \quad (3.5)$$

where  $\omega_n \equiv \frac{(2n+1)\pi}{\beta}$  is the Matsubara frequency for fermions, and  $g_\sigma$  is the noninteracting electron Green function,

$$g_\sigma(\mathbf{k}, i\omega_n) = \frac{1}{i\omega_n + \mu - \epsilon_{\mathbf{k}}}. \quad (3.6)$$

The local Green function is then given by

$$G_{oo,\sigma}(i\omega_n) \equiv \sum_{\mathbf{k}} G_\sigma(\mathbf{k}, i\omega_n) = \int d\epsilon \frac{D(\epsilon)}{i\omega_n + \mu - \epsilon - \Sigma_\sigma(i\omega_n)}, \quad (3.7)$$

where  $D(\epsilon)$  denotes the noninteracting density of electron states in the infinite dimension. When we consider the Bethe lattice,  $D(\epsilon)$  is a semielliptical function,

$$D(\epsilon) = \frac{4}{\pi W} \sqrt{1 - \left(\frac{2\epsilon}{W}\right)^2}, \quad (3.8)$$

where  $W$  is a bandwidth. For the hypercubic lattice we have a Gaussian function,

$$D(\epsilon) = \frac{2\sqrt{2}}{\sqrt{\pi}W_{\text{eff}}} e^{-\frac{8\epsilon^2}{W_{\text{eff}}^2}}. \quad (3.9)$$

Although this function has infinitely long tails, contributions from the high energy parts are exponentially small. Hence, in Eq. (3.9) we defined an effective bandwidth  $W_{\text{eff}}$  as

$$W_{\text{eff}} \equiv 4 \sqrt{\int_{-\infty}^{\infty} \epsilon^2 D(\epsilon) d\epsilon}, \quad (3.10)$$

to give the same second moment as that for semielliptical density of states (3.8) with  $W = W_{\text{eff}}$ .

We can reproduce the Weiss function  $g_0$  from the local Green function (3.7) and the local self-energy  $\Sigma_\sigma(i\omega_n)$  as

$$[g_{0\sigma}(i\omega_n)]^{-1} = [G_{oo,\sigma}(i\omega_n)]^{-1} + \Sigma_\sigma(i\omega_n). \quad (3.11)$$

This equation provides a new Weiss function for the effective action (3.2) through the Fourier transformation,

$$g_{0\sigma}(\tau) = \frac{1}{\beta} \sum_{\omega_n} g_{0\sigma}(i\omega_n) e^{-i\omega_n \tau}. \quad (3.12)$$

Eqs. (3.4), (3.5), (3.7), (3.11), and (3.12) constitute a self-consistent loop, which can be solved numerically.

### · Susceptibilities

We can also calculate the two-particle Green functions in the limit of the infinite dimension. The two-particle Green functions are needed to calculate response functions such as the charge, spin, orbital, and superconducting susceptibilities. Here we take for example the spin susceptibilities  $\chi^{ab}(\mathbf{q}, i\nu)$  ( $a, b = x, y, z$ ), which are calculated in Chap. 5. Although we take a single-orbital model for simplicity in this section, the extension to multiorbits is straightforward. The charge, orbital, and superconducting susceptibilities can be calculated in a similar way.

The spin susceptibility on a lattice is defined by

$$\chi^{ab}(\mathbf{q}, i\nu) \equiv \frac{1}{\beta} \int_0^\beta d\tau \int_0^\beta d\tau' \langle T_\tau S_{\mathbf{q}}^a(\tau) S_{-\mathbf{q}}^b(\tau') \rangle e^{i\nu(\tau-\tau')} \quad (3.13)$$

with  $S^a_{\mathbf{q}}(\tau) \equiv \frac{1}{2} \sum_{\mathbf{k}_{ss'}} c_{\mathbf{k}_s}^\dagger \sigma_{ss'}^a c_{\mathbf{k}+\mathbf{q}_{s'}}$ . With the two-particle Green functions,

$$\begin{aligned} \chi(\mathbf{q}, iv; \mathbf{k}, i\omega; \mathbf{k}', i\omega') &\equiv \int_0^\beta d\tau_1 \int_0^\beta d\tau_2 \int_0^\beta d\tau_3 \int_0^\beta d\tau_4 e^{-i[(\omega+\nu)\tau_1 - \omega\tau_2 + \omega'\tau_3 - (\omega'+\nu)\tau_4]} \\ &\times \frac{1}{4} \sum_{\sigma\sigma'} \sigma\sigma' \langle T_\tau c_{\mathbf{k}+\mathbf{q}\sigma}^\dagger(\tau_1) c_{\mathbf{k}\sigma}(\tau_2) c_{\mathbf{k}'\sigma'}^\dagger(\tau_3) c_{\mathbf{k}'+\mathbf{q}\sigma'}(\tau_4) \rangle, \end{aligned} \quad (3.14)$$

defined on a lattice, the  $zz$  component of the spin susceptibility is written as

$$\chi^{zz}(\mathbf{q}, iv) = \frac{1}{\beta^3} \sum_{\omega\omega'} \sum_{\mathbf{k}\mathbf{k}'} \chi(\mathbf{q}, iv; \mathbf{k}, i\omega; \mathbf{k}', i\omega'). \quad (3.15)$$

We calculate the two-particle Green functions through the Bethe-Salpeter equation,

$$\chi^{-1}(\mathbf{q}, iv; \mathbf{k}, i\omega; \mathbf{k}', i\omega') = \chi_0^{-1}(\mathbf{q}, iv; \mathbf{k}, i\omega; \mathbf{k}', i\omega') - \Gamma(\mathbf{q}, iv; \mathbf{k}, i\omega; \mathbf{k}', i\omega'), \quad (3.16)$$

where  $\chi_0$  is the irreducible lattice Green function defined by

$$\chi_0(\mathbf{q}, iv; \mathbf{k}, i\omega; \mathbf{k}', i\omega') \equiv -\frac{\beta^2}{4} \delta_{\mathbf{k}\mathbf{k}'} \delta_{\omega\omega'} \sum_{\sigma} G_{\sigma}(\mathbf{k} + \mathbf{q}, i\omega + iv) G_{\sigma}(\mathbf{k}, i\omega), \quad (3.17)$$

and  $\Gamma$  is the vertex function.

In the limit of the infinite dimension, the vertex function can be replaced with the local one [108, 109],

$$\Gamma(\mathbf{q}, iv; \mathbf{k}, i\omega; \mathbf{k}', i\omega') = \Gamma(iv; i\omega, i\omega') = \chi_{\text{loc},0}^{-1}(iv; i\omega, i\omega') - \chi_{\text{loc}}^{-1}(iv; i\omega, i\omega'), \quad (3.18)$$

where  $\chi_{\text{loc},0}$  is the irreducible local Green function

$$\chi_{\text{loc},0}(iv; i\omega, i\omega') \equiv -\frac{\beta^2}{4} \delta_{\omega\omega'} \sum_{\sigma} G_{\text{loc},\sigma}(i\omega + iv) G_{\text{loc},\sigma}(i\omega), \quad (3.19)$$

and  $\chi_{\text{loc}}$  is defined by

$$\begin{aligned} \chi_{\text{loc}}(iv; i\omega, i\omega') &\equiv \int_0^\beta d\tau_1 \int_0^\beta d\tau_2 \int_0^\beta d\tau_3 \int_0^\beta d\tau_4 e^{-i[(\omega+\nu)\tau_1 - \omega\tau_2 + \omega'\tau_3 - (\omega'+\nu)\tau_4]} \\ &\times \frac{1}{4} \sum_{\sigma\sigma'} \sigma\sigma' \langle T_\tau c_{\sigma}^\dagger(\tau_1) c_{\sigma}(\tau_2) c_{\sigma'}^\dagger(\tau_3) c_{\sigma'}(\tau_4) \rangle. \end{aligned} \quad (3.20)$$

$G_{\text{loc},\sigma}(i\omega)$  and  $\chi_{\text{loc}}(iv; i\omega, i\omega')$  are the one- and two-particle Green functions, respectively, which are numerically calculated for the impurity model (3.2).

## 3.2 Application to the single-orbital Hubbard model

There exist a huge number of applications of the DMFT not only to the Hubbard model, but to a variety of models such as the periodic Anderson model [110]-[116], the Hubbard-Holstein model [117]-[123], etc. However, we only review the results for the single-orbital Hubbard model in this section, and those for the multi-orbital Hubbard model in the next section.

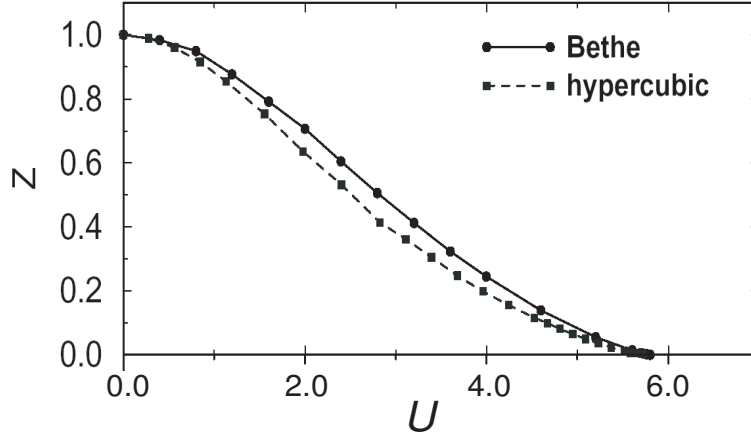


Figure 3.1:  $U$  dependence of the mass renormalization factor  $z$  for the Bethe(hypercubic) lattice with  $W(W_{\text{eff}})=4$ , calculated by Bulla with the DMFT+NRG method (after Ref. [132]).

### 3.2.1 Mott's transition

The first prominent result obtained with the DMFT is the description of Mott's metal-insulator transition in the single-orbital Hubbard model [14, 18, 20, 21, 22, 24, 26, 27], [124]-[139]. As mentioned in Chap. 1 the Mott transition has been a challenge in the field of correlated electron systems. The DMFT provided the first unified framework for describing the transition from both metallic and insulating sides.

From the metallic side the transition is characterized by the disappearance of the mass renormalization factor, i.e., the divergence of the quasiparticle effective mass. Within the DMFT the renormalization factor continuously approaches to zero as  $U$  is increased from weak-coupling region, and it vanishes at a critical coupling  $U_{c2}$  (Fig. 3.1), which is estimated to be  $\sim 1.47W(1.45W_{\text{eff}})$  at  $T = 0$  for the Bethe(hypercubic) lattice [132]. On the other hand an insulating solution is found above  $U_{c1} \sim 1.2W(< U_{c2})$ , so that the metallic and insulating solutions coexist in the range  $U_{c1} < U < U_{c2}$ .

Figure 3.2 is the  $U - T$  phase diagram of the single-orbital Hubbard model at half filling obtained by DMFT studies, where magnetic orders are excluded. We can see that the two lines  $U_{c1}(T)$  and  $U_{c2}(T)$  merge at a critical end point  $(U_c, T_c)$ . The first-order transition line  $U^*(T)$  below  $T_c$  merges again with  $U_{c2}(T)$  line at  $T = 0$ , which means that the transition is of second order at  $T = 0$ .

We can also study the Mott transition in terms of the density of electron states. Figure 3.3 is the density of states  $A(\omega)$  obtained with the DMFT + numerical renormalization-group (NRG) method by Bulla [132]. In the metallic region close to the Mott transition ( $U \lesssim U_c$ ), there is a three peak structure: The broad peaks at around  $\omega = \pm 0.7W$  are considered to be a precursor of the lower and upper Hubbard bands in terms of the Hubbard picture [10], while the sharp quasiparticle peak at  $\omega = 0$  is interpreted as a Kondo resonance peak, which is commonly seen in the Anderson models at low temperatures. As  $U$  increases, the quasiparticle peak becomes narrower, keeping the height  $A(\omega = 0)$

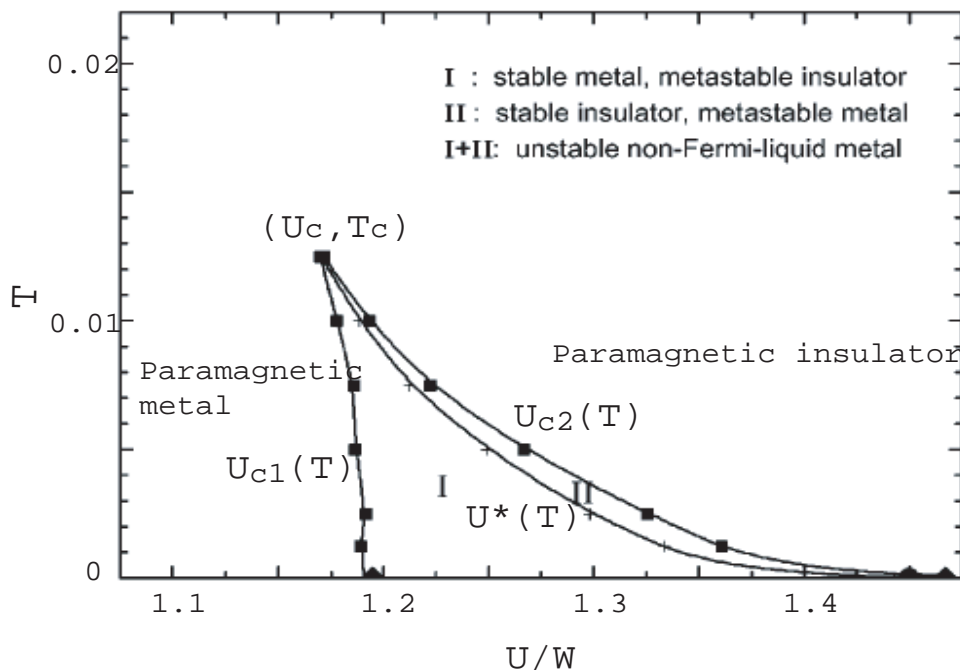


Figure 3.2: Phase diagram of the single-orbital Hubbard model at half-filling, where magnetic orders are excluded. The squares and crosses, calculated with the DMFT+ED method, mark the coexistence boundaries  $U_{c1}(T)$ ,  $U_{c2}(T)$  and the first-order transition line  $U^*(T)$ , respectively. Diamonds at  $T = 0$  denote the DMFT+NRG results. Curves are guide to the eye. (From Ref. [136].)

unchanged, to vanish at a critical coupling  $U_{c2}$ , where the density of states splits into the lower and upper Hubbard bands.

The filling-control Mott transition has also been studied by a number of other authors [14], [18]-[28]. For the two-dimensional Hubbard model, the ground-state phase diagram on the  $U - \mu$  ( $\mu$ : chemical potential) plane was obtained by Watanabe and Imada [28] with the path-integral renormalization-group method [29] (see §1.2.1). For the two-dimensional model, Furukawa and Imada [19] found that the charge compressibility diverges at the zero temperature transition point  $U^*(T = 0)$ . In the infinite dimension, Kotliar *et al.* [27] found a divergence of the charge compressibility at the critical end point  $(U_c, T_c)$ . They discussed the Ce  $\alpha - \gamma$  transition in this light.

### 3.2.2 Ferromagnetism

Ferromagnetism has been another subject of DMFT studies for the single-orbital Hubbard model. Since the DMFT can take account of electron correlations exactly in the infinite dimensional limit, the interest is whether ferromagnetism is realized in the single-orbital model with strong electron correlations.

For the hypercubic lattice no ferromagnetism has been found except for the large

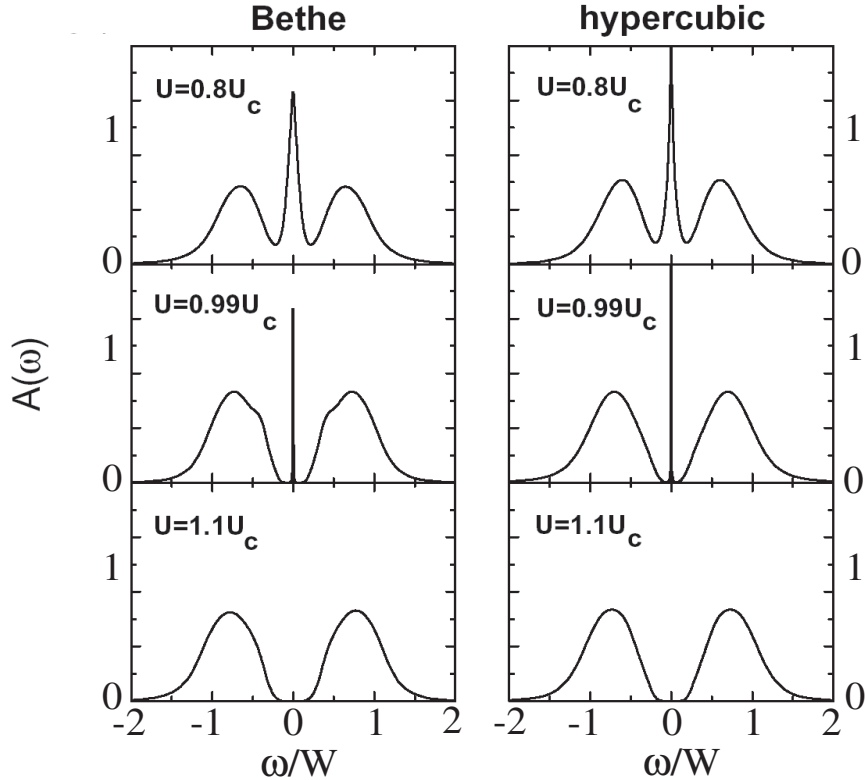


Figure 3.3: Change of the density of states  $A(\omega)$  around Mott's transition, calculated by Bulla with the DMFT+NRG method (after Ref. [132]).

$U$  limit [22, 124, 140, 141]. Ulmke, on the other hand, examined a face-centered cubic (fcc) lattice, which has an asymmetric density of states [142]. He showed, with the DMFT+QMC, that metallic ferromagnetism appears for intermediate  $U$  ( $\sim W$ ) at low temperatures in a rather wide range of filling ( $0.2 \lesssim n \lesssim 0.9$ ). This reminds us of the result obtained by Arita *et al.* [143], who showed, with the fluctuation-exchange and the two-particle self-consistent approximations in the weak coupling regime for three-dimensional lattices, that fcc lattices are favorable for ferromagnetism as compared to simple cubic and body-centered cubic (bcc) lattices.

We focus on this topic in §5.1.2.

### 3.2.3 Superconductivity

Superconductivity is also an important and intriguing issue of electron correlation. Since the DMFT is a mapping on a single-site problem, it cannot treat anisotropic pairings. There have been, however, a variety of generalizations of the DMFT to include spatial correlations [26], [50], [144]-[154].

The  $d$ -wave superconductivity in the two-dimensional (2D) Hubbard model, which is a simple model for high- $T_c$  cuprates, has been studied with cluster extensions of the

DMFT such as the dynamical cluster approximation (DCA) [49, 50, 144, 146, 155]. The DCA takes account of the  $\mathbf{k}$  dependence of the self-energy by mapping the original lattice problem onto a periodic cluster of size  $N_c$ . Maier *et al.* [49] found a finite-temperature transition to the  $d_{x^2-y^2}$ -wave superconductivity in the 2D Hubbard model on a square lattice, using DCA calculations up to  $N_c = 26$ . Because in 2D systems the Mermin-Wagner theorem [51] precludes long-range orders with a broken continuous symmetry at finite temperatures, the superconducting transition, if it still exists in the  $N_c \rightarrow \infty$  limit, is expected to be a Kosterlitz-Thouless transition [52]. The relevance of the DCA result to the Kosterlitz-Thouless transition was discussed by Maier *et al.* [49]

### 3.3 Application to the multiorbital Hubbard model

There are also a large number of DMFT studies for multiorbital systems. However, there has been a discrepancy in the studied models, that is, Hund's exchange and the pair-hopping interactions have been treated differently by authors. It is mainly due to the technical reason that the conventional Hirsch-Fye QMC method, which is a standard solver for the multiorbital DMFT, has difficulties in treating these interactions, while other solvers like the exact diagonalization (ED) or the QMC algorithm proposed by the present authors [156] can handle these interactions. We review these studies, paying a special attention to the treatment of the Hund exchange and pair-hopping interactions.

#### 3.3.1 Mott's transition

The first application of the DMFT to multiorbital systems was done by Rozenberg [157]. He investigated, with the DMFT+QMC, the two-fold degenerate Hubbard model on the Bethe lattice for  $U = U'$  and  $J = 0$  at finite temperatures, and found the first-order metal-insulator transitions at integer fillings ( $n = 1, 2, 3$ ,  $n$ : density of electrons) and a relation  $U_c(n = 2) > U_c(n = 1) = U_c(n = 3)$ . For this type of interactions (i.e.,  $U = U'$  and  $J = 0$ ), the critical coupling  $U_c$  at half filling ( $n = M$ ) increases as the orbital degeneracy  $M$  is increased [158]-[162]. In real  $d$ -electron systems, however, the situation would be more complex since the each  $d$  orbital has different dispersions. The Mott transition for more realistic dispersions, which are constructed from the doubly degenerate  $e_g$  orbitals and the triply degenerate  $t_{2g}$  orbitals on simple cubic and body-centered cubic lattices in three dimensions, has been discussed by Miura and Fujiwara [163] with the DMFT+ the iterative perturbation theory (IPT). They concluded that the critical  $U$  depends significantly on the lattice structure and the shape of the orbitals. The relation of  $U_c$  and  $d$ -orbital degeneracy  $M$  in real materials is still an open question.

The situation is completely changed from the  $U = U'$  model when we take Hund's coupling into account ( $J > 0$ ). In order to see the effect of Hund's coupling the multiorbital Hubbard model without the spin-flip and pair-hopping interactions (in other words, the model with Ising-type Hund's coupling  $-2J\hat{S}_{im}^z\hat{S}_{im'}^z$ , see §2.2) has been studied extensively [159], [164]-[169]. In these studies, the Hirsch-Fye QMC method, which has difficulties in treating SU(2) Hund's coupling  $-2J\hat{\mathbf{S}}_{im} \cdot \hat{\mathbf{S}}_{im'}$  and the pair-hopping interac-

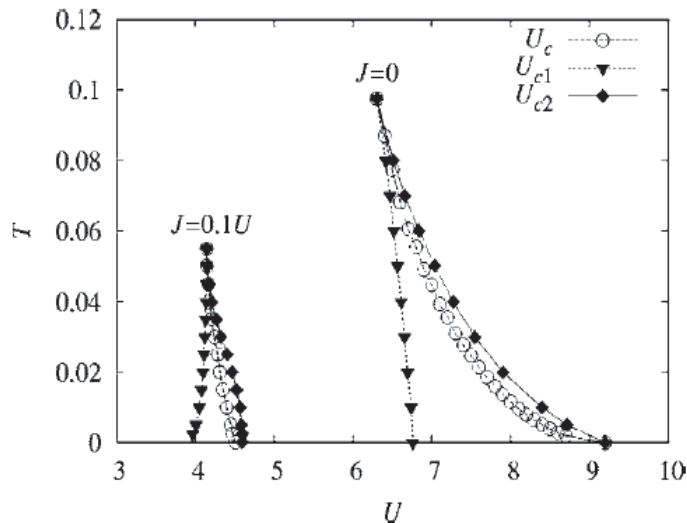


Figure 3.4:  $U - T$  phase diagram for the two-fold degenerate Hubbard model with the  $SU(2)$  Hund coupling  $J = 0.1U$  or with  $J = 0$  for  $U = U' + 2J$  and  $W = 4$ , obtained by Inaba *et al.* [162] Closed symbols denote lower ( $U_{c1}$ ) and upper ( $U_{c2}$ ) critical couplings for the Mott transition while open circles ( $U_c$ ) denote the first-order transition points. Curves are guide to the eye. (From Ref. [162].)

tion, has mainly been employed as a DMFT solver. The critical  $U$  for the Mott transition is considerably decreased when the Ising-type Hund coupling is introduced [159]. The spin and orbital rotational symmetries have been destroyed in these studies.

Koga *et al.* [170] investigated a two-orbital model with  $SU(2)$  Hund's coupling but without the pair-hopping interaction by means of the DMFT+ED method. They discussed the stability of a metallic phase in the model in terms of orbital fluctuations: For small  $J$  (i.e.,  $U \sim U'$ ) a large orbital fluctuation stabilizes metallic states while Hund's coupling suppresses the fluctuation and stabilizes an insulating state. Ōno *et al.* [171] studied the same model, using the linearized DMFT method [133], to show that the inclusion of ( $SU(2)$ -)Hund's exchange coupling changes the nature of the Mott transition at  $T = 0$  from continuous (at  $J = 0$ ) to discontinuous one (for  $J > 0$ ). The same conclusion was obtained by Inaba *et al.* [162] for the two-orbital model with  $SU(2)$  Hund's coupling and the pair-hopping interaction (Fig. 3.4), by means of the self-energy-functional approach [151], which is based on a variational principle for the Luttinger-Ward functional.

Pruschke and Bulla [104] extended the numerical renormalization-group method to two orbits, and applied it to the DMFT. Although their algorithm can treat the spin-flip and pair-hopping interactions, an asymmetric truncation for orbital degrees of freedom, that is, a sequential addition of each orbital space, is needed to repress the increase of the Hilbert space in the iterative diagonalizations. As is described in §2.2, they showed that the Mott transition at ground state is first order for Ising Hund's coupling while second order for  $SU(2)$  Hund's coupling. This result for  $SU(2)$  Hund's coupling conflicts with Inaba's result [162], which suggests a first-order transition. The discrepancy may be due

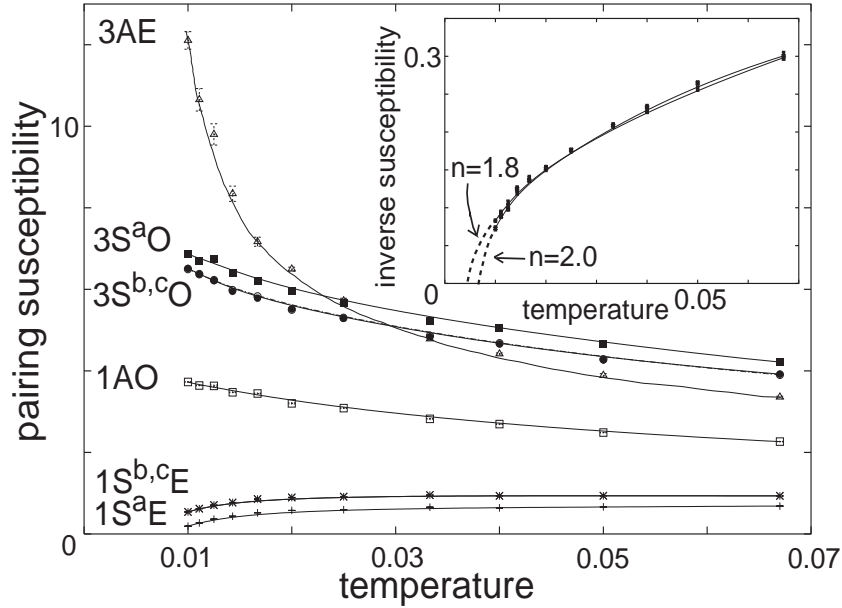


Figure 3.5: Temperature dependence of the  $s$ -wave superconducting susceptibilities in the two-orbital Hubbard model on the hypercubic lattice.  $n = 1.8$ ,  $W_{\text{eff}} = 2\sqrt{2}$ ,  $U = 1.5$ ,  $U' = 0.7$  and  $J = 0.4$  are used. Pairing symmetries are 1: spin-singlet, 3: triplet;  $S^{a,b,c}$ : orbital-symmetric [Eq. (3.21)], A: antisymmetric [Eq. (3.22)]; E: even-, O: odd-frequency. Solid curves are guides to the eye. Inset: Temperature dependence of the inverse susceptibilities of 3AE pairing for  $n = 1.8$  and 2.0. Dashed curves are extrapolations. (From Ref. [156].)

to the different parameterizations for the interactions between the two calculations, while it requires further studies.

### 3.3.2 Ferromagnetism

Ferromagnetism in multiorbital systems has also been explored in the DMFT.

Held and Vollhardt [164] found an itinerant ferromagnetism for the Bethe lattice in the presence of Ising Hund's coupling. However, the absence of the spin and orbital rotational symmetries in this calculation may result in an overestimation of the ferromagnetic instability, as elaborated in §5.2.

Momoi and Kubo [172] applied the DMFT+ED method to the two-orbital Hubbard Hamiltonian including  $SU(2)$  Hund's coupling and the pair-hopping interaction. They investigated the hypercubic lattice around quarter filling ( $n \sim 1$ ) and found a ferromagnetic ground state in the insulating phase at  $n = 1$  and in the electron-doped case at  $n = 1.2$ .

We shall discuss the ferromagnetism in detail in §5.1.3.

### 3.3.3 Superconductivity

Although the single-site nature of the DMFT prohibits to investigate anisotropic pairings like  $p$  and  $d$  waves, we can still discuss a variety of possible pairings in multiorbital systems with the DMFT.

Han [173] and Sakai *et al.* [156] considered the symmetry of Cooper pairs with respect to the orbital degrees of freedom. They studied  $s$ -wave pairing symmetries in the  $d = \infty$  two-orbital degenerate Hubbard model on the Bethe [173] and the hypercubic [156] lattices, developing different QMC schemes (described in §4.2) to take full account of Hund's coupling and the pair-hopping interaction. Since the total symmetry in this case consists of spin  $\otimes$  orbital  $\otimes$  frequency,

Notation	Spin	Orbital	Frequency
1SE	singlet	symmetric	even
3AE	triplet	antisymmetric	even
1AO	singlet	antisymmetric	odd
3SO	triplet	symmetric	odd

are the possibilities. The pairs that are formed across different orbitals are especially interesting. The orbital-symmetric pairs are

$$\begin{aligned}
S^a &: c_{1\uparrow}c_{1\downarrow} + c_{2\uparrow}c_{2\downarrow}, \\
S^b &: c_{1\uparrow}c_{1\downarrow} - c_{2\uparrow}c_{2\downarrow}, \\
S^c &: c_{1\uparrow}c_{2\downarrow} + c_{2\uparrow}c_{1\downarrow},
\end{aligned} \tag{3.21}$$

where  $c_{1\uparrow}c_{1\downarrow}$  and  $c_{2\uparrow}c_{2\downarrow}$  are combined into bonding and antibonding states due to the pair-hopping interaction, while the orbital-antisymmetric pairs are

$$\begin{aligned}
A &: c_{1\uparrow}c_{2\uparrow}, \\
& c_{1\downarrow}c_{2\downarrow}, \\
& c_{1\uparrow}c_{2\downarrow} - c_{2\uparrow}c_{1\downarrow},
\end{aligned} \tag{3.22}$$

which are triply degenerate.

The calculated superconducting susceptibilities (Fig. 3.5) indicate that spin-triplet  $\otimes$  orbital-antisymmetric  $\otimes$  even-frequency pairing is favored in the presence of Hund's coupling, and further the susceptibility diverges at a finite temperature (Fig. 3.5, inset).

However, we should compare this result to that for anisotropic pairings, since in the single-orbital systems a superconductivity from electron-electron repulsions is dominant only when the gap function has nodes in the Brillouin zone. Anisotropic pairings can be treated in principle with the cluster DMFT methods, although the calculation would be too heavy to implement at present.

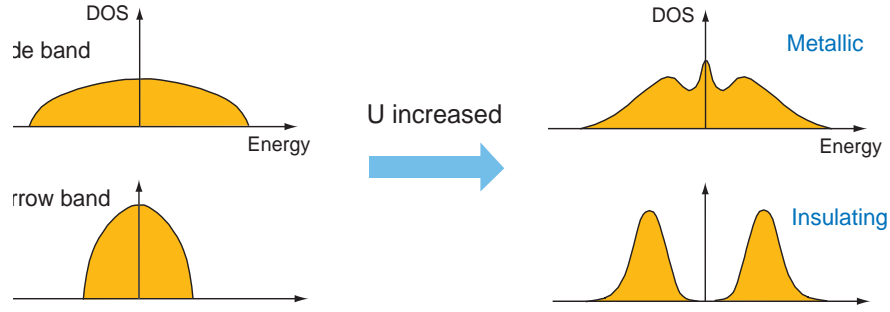


Figure 3.6: A schematic representation of the orbital-selective Mott transition. In  $\text{Ca}_{2-x}\text{Sr}_x\text{RuO}_4$ , the wide and narrow bands correspond to  $d_{xy}$  and  $d_{xz,yz}$ , respectively.

### 3.3.4 Orbital-selective Mott's transition

Another topic specific to multiorbital systems is the orbital selective Mott transition. The phenomenon was first proposed by Anisimov *et al.* [83] to explain an anomalous phase in  $\text{Ca}_{2-x}\text{Sr}_x\text{RuO}_4$ , where strong antiferromagnetic correlations are observed in the metallic region of  $0.2 < x < 0.4$  [79] (see §1.3.3). Considering that the material is a  $t_{2g}$  three-orbital system consisting of one wide band and two narrow bands, Anisimov *et al.* proposed that the wide band has metallic properties while the narrow bands are insulating with the antiferromagnetic correlation (Fig. 3.6). They confirmed this idea with the LDA+DMFT calculation, using the non-crossing approximation as the impurity solver.

After Anisimov's proposal Liebsch [165] claimed a single Mott transition in multiorbital systems, that is, the absence of the orbital-selective Mott transition, based on the DMFT+iterative perturbation theory and the DMFT+QMC study for the two-orbital Hubbard model with one wide and one narrow bands, where he ignored the spin-flip and pair-hopping interactions. Koga *et al.* [174] took account of these interactions by means of the DMFT+exact diagonalization (ED) method, and showed the existence of the orbital-selective Mott phase, in contrast to Liebsch's suggestion. Further studies on this system has been carried over by many authors [166, 167, 168], [175]-[179]. Knecht *et al.* [166] showed, with a high-precision DMFT+QMC simulation, the existence of two distinct Mott transitions even for Ising Hund's coupling, where the two transitions were not discriminated in the accuracy of Liebsch's calculation [165]. Recently a non-Fermi-liquid behavior in the orbital-selective Mott phase was discovered for Ising Hund's coupling by Biermann *et al.* [168] and the problem attracts renewed interests [169].

We note that, despite the evidence for the orbital-selective Mott transitions in the two-orbital Hubbard model with unequal bandwidths, it is still controversial that the transitions really occur in  $\text{Ca}_{2-x}\text{Sr}_x\text{RuO}_4$ . Indeed, there have been some experiments that conflict with the orbital-selective Mott picture, as described in §1.3.3. Hence more realistic calculations are clearly required for this system.

For such a purpose the multiorbital DMFT has been playing an important role, through the so-called local density approximation+DMFT method. We review this method in the next section.

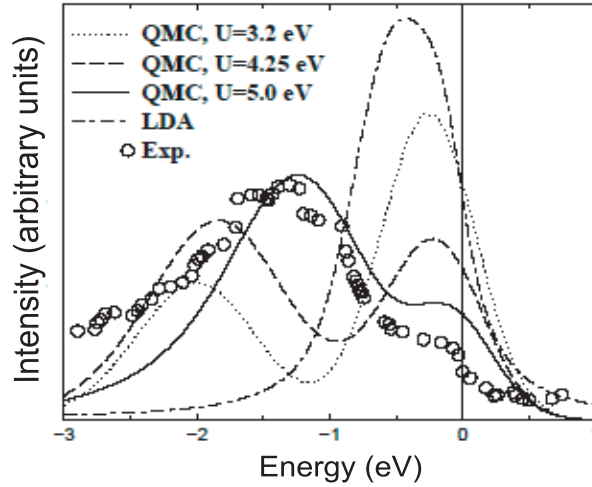


Figure 3.7: Comparison of the one-electron spectra for  $\text{La}_{0.94}\text{Sr}_{0.06}\text{TiO}_3$  obtained from a photoemission experiment [182], an LDA calculation, and an LDA+DMFT(+QMC) calculation (after Ref. [197]).

### 3.4 The LDA+DMFT method

One of the most notable achievements in the quantum chemistry and condensed-matter physics is the density functional theory [180, 181], which has enabled us to calculate electronic structure of real materials from first principles. In order to calculate the exchange-correlation potential, which includes the exchange interaction and correlation effects, the local density approximation (LDA) has been successfully employed in the density functional theory for materials such as light metals and semiconductors. However, the LDA cannot reproduce the electronic structure of strongly-correlated electron systems such as transition-metal oxides; for example,  $\text{LaTiO}_3$  is a Mott insulator experimentally [182, 183], but a metal in the LDA calculation [184]. This is because the LDA does not take account of the strong correlation of localized  $d$  electrons in these materials.

Much effort has been made to incorporate these effects into *ab initio* calculations [181, 185, 186]. A promising approach is to combine the first principles calculations with tight-binding-model calculations which can treat electron correlations [186, 187]. The LDA+DMFT method [188, 189, 190] is one of such methods. In this method the tight-binding model, which is solved with the DMFT, is constructed by the LDA calculation. The multiorbital Hubbard model (2.9) is usually adopted for this purpose, where  $U$ ,  $U'$ ,  $J$ , and the band structure (that is, the one-electron part of the Hamiltonian) are determined by the LDA. The DMFT result can produce a revised electron density for the next input for the LDA calculation. This gives a self-consistent loop for the LDA and the DMFT calculations, although, in practice, most LDA+DMFT calculations reported heretofore, except for Refs. [191]-[196], do not feedback the DMFT result to the LDA. The LDA+DMFT method is promising because the DMFT treats strong correlations, so that it can handle the Mott metal-insulator transition, in particular.

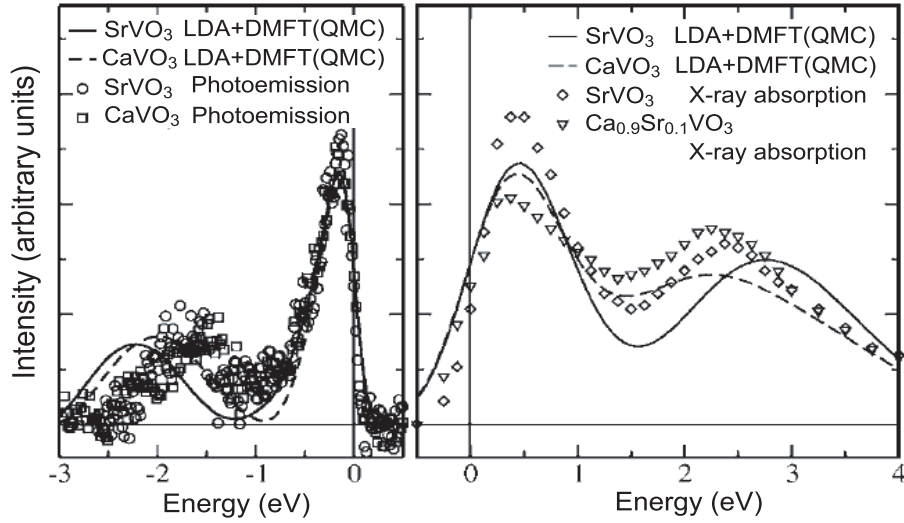


Figure 3.8: Comparison of the one-electron spectra for  $\text{SrVO}_3$  and  $\text{CaVO}_3$  obtained from a photoemission experiment (left panel) [202], an X-ray absorption experiment (right panel) [200] and an LDA+DMFT(+QMC) calculation [202] (after Ref. [202]).

The LDA+DMFT was started by Anisimov *et al.* with an application to the doped Mott insulator  $\text{La}_{1-x}\text{Sr}_x\text{TiO}_3$  [188]. The result for  $x = 0.06$  agrees well with the experimentally obtained photoemission spectra [182], which is not reproduced by the LDA alone (Fig. 3.7 [197]). See also Refs. [198, 199]). Also, the insulating behavior of the above mentioned  $\text{LaTiO}_3$  was reproduced with an LDA+DMFT calculation [199].

Various vanadium compounds have been investigated with the LDA+DMFT method. Especially, a strongly correlated metal  $\text{Sr}_{1-x}\text{Ca}_x\text{VO}_3$  has attracted much attention because of its simple  $3d^1$  electronic configuration. The photoemission spectra (Fig. 3.8, left panel), below the Fermi energy  $E_F$ , of this material have a pronounced quasiparticle peak at around  $E_F$  and a lower Hubbard peak at about  $-1.5$  eV, while the X-ray absorption spectra (Fig. 3.8, right panel), above  $E_F$ , have a quasiparticle peak at around  $E_F$  and an upper Hubbard peak at about  $2.5$  eV [182, 200, 201, 202]. The spectra calculated with the LDA+DMFT reproduce well this spectral structure [199], [201]-[204]. The mechanism of the Mott metal-insulator transition in  $\text{V}_2\text{O}_3$  [130, 205, 206, 207],  $\text{VO}_2$  [196] and  $\text{BaVS}_3$  [204, 208], and a heavy-fermion behavior in  $\text{LiV}_2\text{O}_4$  [209] have also been discussed within this framework.

Lichtenstein *et al.* [210] investigated ferromagnetic Fe and Ni in this scheme, and obtained a Curie temperatures which is close to, but somewhat higher than, the experimental results. We discuss their results in §5.2.

Yamasaki *et al.* [211] investigated the pressure-induced insulator-to-metal transition in  $\text{LaMnO}_3$ . They suggested that the transition is not a Mott-Hubbard type, but is caused by an  $e_g$  orbital splitting due to the interplay of a Jahn-Teller distortion and the Coulomb interaction.

Liebsch and Lichtenstein [212] studied the normal state of the spin-triplet supercon-

ductor  $\text{Sr}_2\text{RuO}_4$  (see §1.3) with this method, where they discussed effects of Hund’s coupling on the normal-state electron spectra. Recently, Pchelkina *et al.* [195] reinvestigated this material, comparing the LDA+DMFT result with photoemission and X-ray absorption experiments, and concluded the presence of strong electron correlations in this material. In §6.1.2 we focus on these applications. For Ca-doped  $\text{Sr}_2\text{RuO}_4$  the LDA+DMFT study [83] fuelled intensive studies on the orbital-selective Mott transition, as described in the previous section.

Many other intriguing transition-metal compounds have been explored with the LDA+DMFT so far; a half-metallic ferromagnet  $\text{CrO}_2$  and a dilute ferromagnetic semiconductor  $\text{Ga}_{1-x}\text{Mn}_x\text{As}$  by Craco *et al.* [213], and the host material of a hydrated superconductor  $\text{Na}_{0.3}\text{CoO}_2$  by Ishida *et al.* [53, 214], among others. The Mott insulating state in alkali-metal loaded zeolites was also studied by Arita *et al.* [215].

The LDA+DMFT has also been applied to  $f$ -electron systems. For example, Savrasov *et al.* [191] suggested, by means of the self-consistent LDA+DMFT method, that the volume change between  $\alpha$ - and  $\delta$ -phases in the metallic plutonium is originated from electron correlations. Held *et al.* [192] discussed the Ce  $\gamma$ -to- $\alpha$  volume collapse transition in terms of the volume dependence of the correlation energy (see also Ref. [216].) McMahan [193] extended this argument to other lanthanides, Pr and Nd.

Despite these successes, there are some obvious defects in the LDA+DMFT method. First, the DMFT, due to its mean-field nature, cannot treat spatial anisotropy, or neglects spatial fluctuations. To improve this point, Sun and Kotliar [148], Zein and Antropov [149], and Biermann *et al.* [150] proposed to combine the GW method, which approximates the electron self-energy with a product of the Green function and a screened Coulomb interaction, and the DMFT, instead of the LDA+DMFT. In this scheme we can expect that the spatial fluctuations at the RPA (random phase approximation) level are incorporated. Another natural solution to this problem is to adopt the cluster-DMFT methods [50, 217] (see §3.2.3). However, because most strongly-correlated materials have the orbital degrees of freedom, we must solve a multiorbital cluster problem in these cases. The Hirsch-Fye QMC method, which has been a standard and the only exact solver for the single-orbital cluster problems, can handle only very small clusters in multiorbital cases; four sites with two orbitals may be the limit of computation, when we include full Hund’s coupling. Since cluster-DMFT methods suffer finite-size effects for a small cluster size [49], some breakthrough is required to proceed in this direction.

Second flaw in the existing LDA+DMFT studies are the following: Since most LDA+DMFT studies have employed the Hirsch-Fye QMC method as the impurity solver, the spin-flip and the pair-hopping interactions in the Hamiltonian (2.9) have been neglected so far. This violation of the spin and orbital rotational symmetries of the Hamiltonian may lead to wrong conclusions.

We develop in §4.5 a numerically exact quantum Monte Carlo method preserving these rotational symmetries. In §6.4.1 we apply the algorithm to the LDA+DMFT calculation for  $\text{Sr}_2\text{RuO}_4$ , and show that qualitative differences do indeed exist between the quasiparticle spectra obtained with the conventional Hirsch-Fye QMC algorithm (for Ising Hund’s coupling ) and those with our new algorithm (for full Hund’s coupling).

### 3.5 Comparison of impurity solvers

To extend applicability of the DMFT various solvers have been developed for the impurity models. These solvers have their pros and cons, and are accordingly favorable in different situations.

The iterative perturbation theory [107, 161, 218, 219] and the non-crossing approximation [22, 125, 220] solve the impurity problem approximately, assuming some analytic form for the self-energy. These methods are computationally inexpensive, and are conveniently applied to large number of orbits, although they cannot treat electron correlations accurately. The linearized DMFT [133] has an analytic solution of the self-consistent loop but it can treat only the vicinity of Mott’s transition.

There are some numerically exact<sup>1</sup> methods such as the exact diagonalization (ED), the Hirsch-Fye quantum Monte Carlo (HFQMC) method, and the numerical renormalization-group (NRG) method.

The ED [128] maps the effective impurity problem (3.2) onto the Anderson impurity Hamiltonian [see Eq. (4.1) below] with finite number of conduction bath orbitals. The method becomes exact in the limit of large number of the bath orbitals. The ED has the advantage that it can easily handle all the multiorbital interactions including Hund’s exchange and the pair-hopping term. However, it cannot treat large numbers of bath orbitals because the dimension of the Hilbert space increases exponentially with the number of bath orbitals. The orbital degree of freedom at impurity site further increases the dimension and decreases the number of tractable bath orbitals (in practice 4-6 bath sites are taken for two-orbital impurity models). Therefore the DMFT+ED studies have been usually limited to two-orbital systems.

The NRG method [132] is also powerful for  $T = 0$  or very low temperatures. The method discretizes conduction-bath electron’s space on a logarithmic energy scale, and takes contributions from lower-energy parts through recursive diagonalizations. It becomes exact in the limit of fine discretization. Although the NRG can take account of infinite number of bath sites as opposed to the ED, it has a difficulty in treating large degrees of freedom at the impurity site because of increasing size of the Hilbert space. So it has been mainly applied to the single-orbital DMFT. An extension to two orbitals was recently made by Pruschke and Bulla [104], but an asymmetric truncation with respect

Solver	Spectrum	Temperature	3 orbitals	SU(2) Hund
ED	discrete	$T \sim 0$	intractable	tractable
NRG	continuous	$T \sim 0$	intractable	possible [104]
HFQMC	continuous	high $T$ or $T = 0$ [225]	possible only for Ising Hund	possible [156, 173]

Table 3.1: Comparison of numerically exact impurity solvers.

<sup>1</sup>Here the word ‘numerically exact’ means that the method becomes exact in some limit which is independent of the parameters in the Hamiltonian.

to the orbital degrees of freedom has to be done to treat SU(2) Hund's coupling and the pair-hopping interaction.

The HFQMC method [221, 222, 223] decomposes the original many-body system into a sum of one-body systems with the Trotter decomposition and the Hubbard-Stratonovich transformation, and samples the one-body systems according to the stochastic weight (for detail, see § 4.1). The method becomes exact in the limit of large Trotter number. The HFQMC can handle not only two but more orbitals in contrast to the ED and the NRG, and also produces continuous spectra. The former is important since there are various intriguing systems having three or more orbitals, especially  $t_{2g}$ -electron transition-metal oxides exemplified by the spin-triplet superconductor  $\text{Sr}_2\text{RuO}_4$  [2, 78]. The latter (spectrum) is crucial for comparing results with experiments like photoemission spectroscopy. For these reasons the HFQMC method has been by far the most widely employed impurity solver, especially for the LDA+DMFT method.

The HFQMC has, however, some difficulties. First, it is difficult to reach low temperatures because lower temperatures require larger Trotter time-discretization numbers, which results in much heavier computations. Second, it requires some contrivance to treat two-body interactions that cannot be written in a density-density form, such as the spin-flip and pair-hopping interactions in the multiorbital Hubbard Hamiltonian (2.9). Moreover, even if we succeed in incorporating these interactions into the HFQMC, there appears the so-called negative sign problem, which further makes low-temperature studies difficult.

For these reasons, in most HFQMC studies<sup>2</sup> including the LDA+DMFT calculations, only the Ising ( $z$ ) component of Hund's exchange coupling has been considered, with the spin-flip ( $x$  and  $y$ ) and pair-hopping terms neglected. This treatment is of course unphysical: It violates the spin and orbital rotational symmetries of the Hamiltonian (2.9).

In order to overcome these adversities in the HFQMC, we develop in the next chapter a new QMC method which can treat the rotationally symmetric Hamiltonian (2.9). The method introduced in §4.5 greatly suppresses the sign problem compared with the HFQMC and can treat more than two orbital systems.

---

<sup>2</sup>Exceptions are Refs. [156, 173, 175] and [176].

# Chapter 4

## The auxiliary-field quantum Monte Carlo methods

We propose an auxiliary-field quantum Monte Carlo (QMC) method for multiorbital systems, especially as a solver for the multiorbital DMFT. The algorithm is based on the Trotter decomposition and a series expansion.

Before embarking on our algorithm we first review the conventional Hirsch-Fye QMC method for the single-orbital Anderson impurity model in §4.1. Next we extend the Hirsch-Fye algorithm to multiorbital models in §4.2, and discuss the sign problem, caused by the spin-flip and pair-hopping interactions, in §4.3. In §4.4 recent developments in QMC methods based on series expansions are reviewed. Our algorithm is introduced in §4.5 and its applicable scope is discussed in §4.6.

### 4.1 The Hirsch-Fye algorithm for the single-orbital case

The Hirsch-Fye QMC method [221, 222, 223] is a well-established, numerically exact solver for the Anderson impurity problem, and it has also been the most widely-used solver for the DMFT [18]. The key ingredients of this method are the Trotter decomposition and the discrete auxiliary-field decoupling (the Hubbard-Stratonovich transformation [221]).

#### · *General formalism*

We start with the single-orbital Anderson impurity model,

$$\begin{aligned}\hat{H}_{\text{AIM}} &= \hat{H}_0 + \hat{H}_{\text{int}}, \\ \hat{H}_0 &\equiv \sum_{p=1}^{n_c} \sum_{\sigma} \epsilon_p c_{p\sigma}^\dagger c_{p\sigma} + \sum_{p=1}^{n_c} \sum_{\sigma} (V_p c_{p\sigma}^\dagger c_{d\sigma} + \text{H.c.}) + \left( \epsilon_d + \frac{U}{2} \right) \sum_{\sigma} n_{d\sigma}, \\ \hat{H}_{\text{int}} &\equiv U \left( n_{d\uparrow} n_{d\downarrow} - \frac{n_{d\uparrow} + n_{d\downarrow}}{2} \right),\end{aligned}\tag{4.1}$$

where  $p = 1, \dots, n_c$  represent the conduction-bath orbitals,  $d$  represents the impurity site, and  $\epsilon_p$  and  $\epsilon_d$  are the corresponding one-electron energies.

The partition function of this system is

$$Z = \text{Tr} e^{-\beta \hat{H}_{\text{AIM}}}. \quad (4.2)$$

In order to implement a numerical calculation, the imaginary time interval  $[0, \beta]$  is discretized into  $L$  time slices,

$$\begin{aligned} \tau_l &= l\Delta\tau \quad (l = 1, \dots, L), \\ \Delta\tau &= \beta/L. \end{aligned} \quad (4.3)$$

With the Trotter decomposition, the partition function (4.2) becomes

$$Z = \text{Tr} \prod_{l=1}^L e^{-\Delta\tau(\hat{H}_0 + \hat{H}_{\text{int}})} = \text{Tr} \prod_{l=1}^L e^{-\Delta\tau\hat{H}_0} e^{-\Delta\tau\hat{H}_{\text{int}}} + O(\Delta\tau^2), \quad (4.4)$$

where the exponential of the original Hamiltonian  $\hat{H}_{\text{AIM}}$  was decoupled into a product of non-interacting part  $e^{-\Delta\tau\hat{H}_0}$  and interacting part  $e^{-\Delta\tau\hat{H}_{\text{int}}}$ .

Hirsch and Fye [221, 222] applied the discrete Hubbard-Stratonovich transformation,

$$\begin{aligned} e^{-a[n_\uparrow n_\downarrow - \frac{1}{2}(n_\uparrow + n_\downarrow)]} &= \begin{cases} \frac{1}{2} \sum_s^{\pm 1} e^{\lambda s(n_\uparrow - n_\downarrow)} & (a \geq 0) \\ \frac{1}{2} \sum_s^{\pm 1} e^{\lambda s(n_\uparrow + n_\downarrow - 1) + \frac{a}{2}} & (a < 0) \end{cases}, \\ \lambda &\equiv \ln\left(e^{\frac{|a|}{2}} + \sqrt{e^{|a|} - 1}\right), \end{aligned} \quad (4.5)$$

to the interacting part at every time slice. Then the partition function (4.2) is written as

$$Z = \frac{1}{2^L} \sum_{s_1, \dots, s_L} Z_{s_1, \dots, s_L}, \quad (4.6)$$

where

$$\begin{aligned} Z_{s_1, \dots, s_L} &\equiv \prod_{\sigma} Z_{s_1, \dots, s_L}^{\sigma}, \\ Z_{s_1, \dots, s_L}^{\sigma} &\equiv \text{Tr} \prod_{l=1}^L e^{-\Delta\tau\hat{H}_0^{\sigma}} e^{\lambda\sigma s_l n_{\sigma}}, \\ \hat{H}_0 &= \sum_{\sigma} \hat{H}_0^{\sigma}. \end{aligned} \quad (4.7)$$

The above equations are interpreted as a decomposition of the many-particle problem into a sum of single-particle problems, which are specified by the auxiliary fields  $s_1, \dots, s_L$ . After this decomposition, we can obtain the expectation value of an arbitrary operator  $\hat{A}$  as

$$\langle \hat{A} \rangle = \frac{1}{2^L} \sum_{s_1, \dots, s_L} \frac{Z_{s_1, \dots, s_L} \langle \hat{A} \rangle_{s_1, \dots, s_L}}{Z} = \frac{\sum_{s_1, \dots, s_L} Z_{s_1, \dots, s_L} \langle \hat{A} \rangle_{s_1, \dots, s_L}}{\sum_{s_1, \dots, s_L} Z_{s_1, \dots, s_L}}, \quad (4.8)$$

where  $\langle \rangle_{s_1, \dots, s_L}$  denotes the averaging in the single-particle system specified by the values of  $s_1, \dots, s_L$ .

If we were to take the sum completely, we had to calculate the expectation values of  $\hat{A}$  in  $2^L$  single-particle systems. That is impossible in actuality when  $L$  takes a large number. Therefore, the stochastic Monte Carlo sampling is used, where  $Z_{s_1, \dots, s_L}$  is interpreted as a stochastic weight. Namely, we replace the right hand side of Eq. (4.8) with

$$\frac{\sum_{\text{QMC}} Z_{s_1, \dots, s_L} \langle \hat{A} \rangle_{s_1, \dots, s_L}}{\sum_{\text{QMC}} Z_{s_1, \dots, s_L}}, \quad (4.9)$$

where  $\sum_{\text{QMC}}$  denotes the sum over Monte Carlo samples.

#### · *Single-particle Green's function*

To carry out the DMFT self-consistency cycle we evaluate Green's function  $G^\sigma(\tau, \tau') \equiv \langle T_\tau c_\sigma(\tau) c_\sigma^\dagger(\tau') \rangle$  in the Monte Carlo sampling, where  $T_\tau$  is the time ordering operator. Applying the formula (4.8) we can see that

$$G_\sigma(\tau, \tau') = \frac{1}{2^L} \sum_{s_1, \dots, s_L} \frac{Z_{s_1, \dots, s_L}}{Z} g_{s_1, \dots, s_L; \sigma}(\tau, \tau'),$$

$$g_{s_1, \dots, s_L; \sigma}(\tau, \tau') \equiv \langle T_\tau c_\sigma(\tau) c_\sigma^\dagger(\tau') \rangle_{s_1, \dots, s_L}, \quad (4.10)$$

where  $g_{s_1, \dots, s_L; \sigma}$  is the Green function of a noninteracting particle in the time-dependent external potential  $s_1, \dots, s_L$ .

These Green functions  $\{g_{s_1, \dots, s_L; \sigma}\}$  for different set of values of  $(s_1, \dots, s_L)$  are combined with each other by an  $L \times L$  matrix equation [222, 223],

$$\begin{aligned} g' &= g + (g - 1)(e^{-V} e^{V'} - 1)g', \\ (e^V)_{ij} &= e^{\sigma \lambda s_i} \delta_{ij}, \\ (g)_{ij} &= g(\tau_i, \tau_j), \end{aligned} \quad (4.11)$$

where we abbreviated  $g \equiv g_{s_1, \dots, s_L; \sigma}$  and  $g' \equiv g_{s'_1, \dots, s'_L; \sigma}$ , etc. For  $s_1 = s_2 = \dots = s_L = 0$  we have  $e^V = 1$ . Thus the above equation enables us to compute the Green function  $g_{s_1, \dots, s_L}$  for any auxiliary-field configuration from the noninteracting Green function  $g_0$ . So we can obtain the Green function  $G$  directly from the Weiss function  $g_0$ , without determining the parameters  $\epsilon_p$ ,  $V_p$ , and  $\epsilon_d$  in the Hamiltonian (4.1).

## 4.2 Extension to multiorbital systems

Sakai *et al.* [156] extended the Hirsch-Fye algorithm to multiorbital Anderson models that include the spin-flip and pair-hopping terms,

$$\begin{aligned} \hat{H}_{\text{int}} &= \hat{H}_U + \hat{H}_J, \\ \hat{H}_U &\equiv U \sum_m n_{m\uparrow} n_{m\downarrow} + \sum_{m < m', \sigma} [U' n_{m\sigma} n_{m'-\sigma} + (U' - J) n_{m\sigma} n_{m'\sigma}], \\ \hat{H}_J &\equiv J \sum_{m < m'} (c_{m\uparrow}^\dagger c_{m'\downarrow}^\dagger c_{m\downarrow} c_{m'\uparrow} + c_{m\uparrow}^\dagger c_{m\downarrow}^\dagger c_{m'\downarrow} c_{m'\uparrow} + \text{H.c.}), \end{aligned} \quad (4.12)$$

where the main contrivance is in the auxiliary-field decoupling of the spin-flip and pair-hopping interactions  $\hat{H}_J$  [156]. Although there have been many DMFT+QMC studies for multiorbital systems, including the LDA+DMFT calculations, all of them before Ref. [156, 173] had neglected the spin-flip and pair-hopping interactions  $\hat{H}_J$  because the Hubbard-Stratonovich transformation (4.5) is only applicable for the density-density interaction  $\hat{H}_U$  while the practical decoupling formula for  $\hat{H}_J$  had been lacking. As mentioned in §2.2 the neglect of  $\hat{H}_J$  may give rise to unphysical results because of the absence of the spin and orbital rotational symmetries, so that a scheme to take in  $\hat{H}_J$  has been desired.

There had been several efforts in this direction.

· *Held and Vollhardt (1998)*

Held and Vollhardt [164] attempted the following transformation,

$$e^{J\Delta\tau c_1^\dagger c_2 c_3^\dagger c_4} = \frac{1}{2} \sum_s^{\pm 1} e^{s\alpha(c_1^\dagger c_2 - c_3^\dagger c_4)},$$

$$\alpha \equiv \sqrt{J\Delta\tau}, \quad (4.13)$$

for  $\hat{H}_J$  term. However, this type of transformation has serious problems: First, in order to apply this transformation to  $e^{-\Delta\tau\hat{H}_J}$ , we must decompose

$$e^{-\Delta\tau\hat{H}_J} = \exp[-\Delta\tau J \sum_{m \neq m'} (c_{m\uparrow}^\dagger c_{m'\downarrow}^\dagger c_{m\downarrow} c_{m'\uparrow} + c_{m\uparrow}^\dagger c_{m\downarrow}^\dagger c_{m'\downarrow} c_{m'\uparrow})] \quad (4.14)$$

into a product of the exponentials of the form (4.13), i.e.,

$$\prod_{m \neq m'} \exp(-\Delta\tau J c_{m\uparrow}^\dagger c_{m'\downarrow}^\dagger c_{m\downarrow} c_{m'\uparrow}) \exp(-\Delta\tau J c_{m\uparrow}^\dagger c_{m\downarrow}^\dagger c_{m'\downarrow} c_{m'\uparrow}). \quad (4.15)$$

This decomposition not only causes an error of the order  $O(\Delta\tau^2)$ , which is summed up into  $O(\Delta\tau)$  by collecting over the imaginary time, but violates the equality of the spins and of the orbitals in the interaction terms. Second, even if we allow the above decomposition, the implementation of this algorithm encounters a severe sign problem, as pointed by Held and Vollhardt [164]. Third, this transformation requires four auxiliary fields for each two-orbital part of  $\hat{H}_J$ , which results in a heavy computation.

· *Motome and Imada (1997)*

A more practical way to treat these interactions was developed by Motome and Imada [224]. They wrote the two-body interaction Hamiltonian of the  $M$ -orbital Hubbard model in a quadratic form,

$$\hat{H}_{\text{int}} = \frac{U'}{2}(n - M)^2 + \frac{J}{2} \sum_{m < m'} \hat{A}_{mm'}^2 + (U - U') \sum_m n_{m\uparrow} n_{m\downarrow},$$

$$\hat{A}_{mm'} \equiv \sum_{\sigma} (c_{m\sigma}^\dagger c_{m'\sigma} + c_{m'\sigma}^\dagger c_{m\sigma}), \quad (4.16)$$

where  $U$  and  $U'$  are the intra- and interorbital Coulomb interactions, and  $J$  is Hund's rule coupling. As mentioned in §2.1,  $U$ ,  $U'$  and  $J$  are related by  $U' = U - 2J$ .

Motome and Imada applied the general formula for an arbitrary operator  $\hat{f}$ ,

$$\begin{aligned} e^{-\alpha \hat{f}^2} &= \sum_{l,s}^{\pm 1} \frac{\gamma_l}{4} e^{i s \eta_l \sqrt{\alpha} \hat{f}} + O(\Delta\tau^4), \\ \alpha &\geq 0, \\ \gamma_l &\equiv 1 + \frac{\sqrt{6}}{3} l, \\ \eta_l &\equiv \sqrt{2(3 - \sqrt{6}l)}, \end{aligned} \quad (4.17)$$

to the quadratic terms in the Hamiltonian (4.16).

An important point in this method is that, when there exists an electron-hole symmetry and when the third term of  $\hat{H}_{\text{int}}$ ,  $(U - U') \sum_m n_{m\uparrow} n_{m\downarrow}$ , in Eq. (4.16) is neglected, no negative weight appears. In such a case,  $Z_{\{s_l\}}^\uparrow$  becomes the complex conjugate of  $Z_{\{s_l\}}^\downarrow$  with a particle-hole transformation, so the weight (4.7) becomes positive.

However, this situation is not realized when we take account of the third term in Eq. (4.16), because this term has to be transformed with the usual H-S transformation (4.5), where the auxiliary fields are real and opposite sign for the opposite spin components, as contrasted with a complex field in (4.17), so that  $Z_{\{s_l\}}^\uparrow = Z_{\{s_l\}}^\downarrow$  cannot hold. For this reason, Motome and Imada considered an unphysical situation,  $U = U'$  and  $J > 0$ , and neglected the third term in Eq. (4.16), but this treatment breaks the orbital rotational symmetry of the interaction.

· *Han (2004)*

Contrary to these discrete auxiliary-field transformations (4.13) and (4.16), Han [173] exploited a continuous auxiliary field transformation

$$e^{\hat{f}^2} = \int dx \exp(-\pi x^2 + 2\sqrt{\pi} \hat{f} x). \quad (4.18)$$

He expressed  $\hat{H}_J$  for two orbits in a form

$$-\frac{J}{2} \left[ \sum_{\sigma} \sigma (c_{1\sigma}^\dagger c_{2\sigma} + c_{2\sigma}^\dagger c_{1\sigma}) \right]^2 + \frac{J}{2} \sum_{m\sigma} n_{m\sigma} - J \sum_{\sigma} n_{1\sigma} n_{2\sigma}, \quad (4.19)$$

and applied Eq. (4.18) to the first term while he decoupled the last term with the discrete Hubbard-Stratonovich transformation (4.5).

Since, as he showed, this transformation largely improves sign problem compared with the transformation (4.13), this method would be promising, although we must pick out the values of (continuous) auxiliary fields from infinite sample space at each time slices.

· *Sakai et al. (2004)*

Sakai *et al.* [156] proposed a *real and discrete* decoupling formula for  $\hat{H}_J$  for two orbits in a form,

$$e^{-\Delta\tau\hat{H}_J} = \frac{1}{2} \sum_r^{\pm 1} e^{\lambda r(\hat{f}_\uparrow - \hat{f}_\downarrow)} e^{a(\hat{N}_\uparrow + \hat{N}_\downarrow) + b\hat{N}_\uparrow\hat{N}_\downarrow}, \quad (4.20)$$

where

$$\begin{aligned} \lambda &\equiv \frac{1}{2} \ln \left( e^{2J\Delta\tau} + \sqrt{e^{4J\Delta\tau} - 1} \right), \\ a &\equiv -\ln[\cosh(\lambda)], \\ b &\equiv \ln[\cosh(J\Delta\tau)], \\ \hat{f}_\sigma &\equiv c_{1\sigma}^\dagger c_{2\sigma} + c_{2\sigma}^\dagger c_{1\sigma}, \\ \hat{N}_\sigma &\equiv n_{1\sigma} + n_{2\sigma} - 2n_{1\sigma}n_{2\sigma}. \end{aligned} \quad (4.21)$$

The key points are the relation for  $\hat{f}_\sigma$ ,

$$\hat{f}_\uparrow\hat{f}_\downarrow = \hat{f}_\downarrow\hat{f}_\uparrow = \frac{1}{J}\hat{H}_J, \quad (4.22)$$

and the property of  $\hat{N}_\sigma$ ,

$$\hat{N}_\sigma^2 = \hat{N}_\sigma. \quad (4.23)$$

Although the term  $\hat{N}_\uparrow\hat{N}_\downarrow$  on the right hand side of equation (4.20) is forth order in  $n$ , we can apply the Hubbard-Stratonovich transformation (4.5) to this term, due to the property (4.23). The resulting terms of the form  $nn$  can be combined with  $\hat{H}_U$  terms. Therefore, we need *only two* auxiliary fields for  $\hat{H}_J$ .

With the transformation (4.20) we can assign the values of  $U$ ,  $U'$ , and  $J$  independently, so that we can also hold the real-space rotational symmetry of orbitals ( $U = U' + 2J$ ). Moreover, we found that the sign problem is largely relaxed with this transformation compared with the transformation (4.13) and (4.17).

Using the transformation (4.20) we investigated superconductivity in multiorbital systems within the dynamical mean-field approximation. Although the DMFT cannot treat anisotropic pairings, the symmetry of Cooper pairs with respect to the orbital degrees of freedom gives various type of pairings, as elaborated in §3.3.3. Actually we found that the spin-triplet orbital-antisymmetric pairing is most dominant among  $s$ -wave pairings in a rather wide range of filling [156].

Koga *et al.* [175] implemented the DMFT+QMC calculation with the transformation (4.20) to study the orbital-selective Mott transition, where the rotational symmetry of Hund's coupling plays a crucial role. They revealed important roles of orbital fluctuations on the Mott transitions. Arita and Held [176] incorporated the transformation (4.20) into the DMFT+projective QMC method, which can address ground-state properties [225]. They elucidated the existence of the orbital-selective Mott transition at zero temperature.

Despite these successes, some problems remain to be solved. One is the sign problem, which is much improved with the transformation (4.20), but still hampers studies at low

temperatures. Another is the difficulty to extend the transformation (4.20) [and other transformations (4.17) and (4.18)] to three or more orbitals. Since the distinct two-orbital parts  $\hat{H}_J^{mm'}$ 's in  $\hat{H}_J$  do not commute with each other, we cannot decouple the exponential of  $\hat{H}_J \equiv \sum_{m<m'} \hat{H}_J^{mm'}$  for three or more orbitals into the simple product of two-orbital parts. In other words, we have

$$e^{-\Delta\tau\hat{H}_J} \neq \prod_{m<m'} e^{-\Delta\tau\hat{H}_J^{mm'}}, \quad (4.24)$$

where the right hand side violates the equality of the orbital degrees of freedom in  $\hat{H}_J$ .<sup>1</sup> Therefore, if we want to decouple  $e^{-\Delta\tau\hat{H}_J}$  for more than two orbitals, we must construct a formula decoupling all the  $\hat{H}_J$  terms simultaneously, without separating it into each two orbital part  $\hat{H}_J^{mm'}$ . It seems, however, almost impossible.

In §4.5 we see that these difficulties can be overcome by use of a series expansion, instead of the Trotter decomposition, for  $\hat{H}_J$ .

### 4.3 Negative-sign problem

Quantum Monte Carlo methods have often been plagued by the so-called negative-sign problem [226, 227]. This problem comes from the fact that the weight of decoupled systems,  $Z_{s_1, \dots, s_L}$  in Eq. (4.7), is not positive definite, which associates with the anticommutative property of electrons, and the cancellation of negative and positive weights makes QMC simulations inefficient.

When a negative weight appears in Eq. (4.8), we must change the weight  $Z_{\{s_l\}}$  into  $|Z_{\{s_l\}}|$  and accordingly, the observable  $\hat{A}$  into  $\text{sign}Z_{\{s_l\}}\hat{A}$ , to retain a probability interpretation of the weight. Then Eq. (4.8) is rewritten as

$$\begin{aligned} \langle \hat{A} \rangle &= \frac{\sum_{\{s_l\}} Z_{\{s_l\}} \langle \hat{A} \rangle_{\{s_l\}}}{\sum_{\{s_l\}} |Z_{\{s_l\}}|} \cdot \frac{\sum_{\{s_l\}} |Z_{\{s_l\}}|}{\sum_{\{s_l\}} Z_{\{s_l\}}} = \frac{\langle \text{sign}Z_{\{s_l\}} \langle \hat{A} \rangle_{\{s_l\}} \rangle_{\text{abs}}}{\langle \text{sign}Z_{\{s_l\}} \rangle_{\text{abs}}}, \\ \langle \dots \rangle_{\text{abs}} &\equiv \frac{\sum_{\{s_l\}} |Z_{\{s_l\}}| \dots}{\sum_{\{s_l\}} |Z_{\{s_l\}}|}. \end{aligned} \quad (4.26)$$

---

<sup>1</sup>It is possible to recover the equality of orbitals in the interaction by summing over the order in which the each two-orbital part  $e^{-\Delta\tau\hat{H}_J^{mm'}}$  appears. Namely, considering  $e^{-\Delta\tau\hat{H}_J}$  for three orbitals for example, we can decompose it as

$$\begin{aligned} e^{-\Delta\tau\hat{H}_J} &= \frac{1}{6} \left( e^{-\Delta\tau\hat{H}_J^{12}} e^{-\Delta\tau\hat{H}_J^{23}} e^{-\Delta\tau\hat{H}_J^{13}} + e^{-\Delta\tau\hat{H}_J^{12}} e^{-\Delta\tau\hat{H}_J^{13}} e^{-\Delta\tau\hat{H}_J^{23}} \right. \\ &\quad + e^{-\Delta\tau\hat{H}_J^{23}} e^{-\Delta\tau\hat{H}_J^{12}} e^{-\Delta\tau\hat{H}_J^{13}} + e^{-\Delta\tau\hat{H}_J^{23}} e^{-\Delta\tau\hat{H}_J^{13}} e^{-\Delta\tau\hat{H}_J^{12}} \\ &\quad + e^{-\Delta\tau\hat{H}_J^{13}} e^{-\Delta\tau\hat{H}_J^{12}} e^{-\Delta\tau\hat{H}_J^{23}} + e^{-\Delta\tau\hat{H}_J^{13}} e^{-\Delta\tau\hat{H}_J^{23}} e^{-\Delta\tau\hat{H}_J^{12}} \left. \right) \\ &\quad + O(\Delta\tau^3). \end{aligned} \quad (4.25)$$

However, this decomposition will not be suitable because the severe sign problem will occur and also the large volume of the sample space will lead to a heavy computation.

In general as temperature is lowered or interaction is strengthened, the number of negative weights appearing in QMC samples approaches to that of positive weights, and the average sign,

$$\frac{\sum_{\text{QMC}} Z_{\{s_l\}}}{\sum_{\text{QMC}} |Z_{\{s_l\}}|}, \quad (4.27)$$

decays to zero. Because this decay is exponential, it becomes quite difficult at low temperatures to obtain averaged quantities with sufficient accuracies. This problem has been a serious obstacle to QMC calculations for the finite-dimensional Hubbard model, where the transfer of electrons between sites is a source of negative weights.

In the DMFT, however, no negative weights appear in calculation for the single-orbital Hubbard model. This is because the DMFT replaces the hopping between sites by a mean field, so that there are no particle-interchanging terms in this approximation [228]. The sign problem does not occur in the DMFT even for the multiorbital Hubbard model with Ising-type Hund's coupling. Nevertheless, when we include  $\hat{H}_J$ , the sign problem arises because this interaction exchanges electrons having different spins and orbitals. The severity of the sign problem depends on how to decompose the original system into one-body systems. Although there is no firm guiding principle to reduce negative weights, we semiempirically know that negative weights are suppressed (i) when nondiagonal parts, corresponding to  $\hat{H}_J$ , of the interaction matrix ( $e^V$  in Eq. (4.11)) is small, or (ii) when the nondiagonal parts appear less frequently.

In §4.5 we propose a novel QMC algorithm based on a series expansion. The algorithm remedies the sign problem to a large extent (see §4.6). We consider that the point (ii) is, in particular, relevant to this relaxation of the sign problem, since the series expansion gives  $\hat{H}_J$  less chance to appear than the conventional Trotter decomposition does.

Before turning to our algorithm, in the next section we review recent progress in QMC methods based on series expansions.

## 4.4 Series-expansion algorithms

A series-expansion QMC method for electron systems was first proposed by Rombouts *et al.* [229] These authors employed a perturbation series expansion,

$$\begin{aligned} e^{-\beta\hat{H}+\alpha} &= e^{-\beta\hat{H}_0+\alpha-\beta\hat{H}_{\text{int}}} \\ &= e^{-\beta\hat{H}_0} + \sum_{k=1}^{\infty} \int_0^1 dt_k \int_0^{t_k} dt_{k-1} \cdots \int_0^{t_2} dt_1 \\ &\quad \times e^{-t_1\beta\hat{H}_0} (\alpha - \beta\hat{H}_{\text{int}}) e^{(t_1-t_2)\beta\hat{H}_0} (\alpha - \beta\hat{H}_{\text{int}}) \cdots e^{(t_{k-1})\beta\hat{H}_0}, \end{aligned} \quad (4.28)$$

instead of the Trotter decomposition (4.4), to separate out the two-body interaction in the partition function, where they added a constant  $\alpha$  to the Hamiltonian and expanded the Boltzmann factor with respect to  $\alpha - \beta\hat{H}_{\text{int}}$ . While the factor  $\alpha$  does not affect the physics since it just shifts the origin of energy, introduction of  $\alpha$  makes it possible to decouple the

two-body interaction part with auxiliary fields. Namely, when we consider the Hubbard-type interaction,  $\hat{H}_{\text{int}} \equiv U \sum_i [n_{i\uparrow}n_{i\downarrow} - \frac{1}{2}(n_{i\uparrow} + n_{i\downarrow})]$ , for example,  $\alpha - \beta\hat{H}_{\text{int}}$  is decoupled with the Hubbard-Stratonovich transformation (4.5) through

$$\begin{aligned}\alpha - \beta\hat{H}_{\text{int}} &= \frac{\alpha}{N} \sum_i e^{-\tilde{a}[n_{i\uparrow}n_{i\downarrow} - \frac{1}{2}(n_{i\uparrow} + n_{i\downarrow})]}, \\ \tilde{a} &\equiv \ln\left(1 + \frac{N\beta U}{2}\right),\end{aligned}\quad (4.29)$$

where  $N$  is the system size and we used an equation,  $(n_{i\uparrow} + n_{i\downarrow} - 2n_{i\uparrow}n_{i\downarrow})^2 = n_{i\uparrow} + n_{i\downarrow} - 2n_{i\uparrow}n_{i\downarrow}$ . Rombouts *et al.* [230] showed that the algorithm can be applied to a class of interactions such as the Hubbard interaction and the pairing interaction for atomic nuclei. An application to the finite-size single-orbital Hubbard model succeeded in obtaining results without time-discretization errors with less computational time than the conventional, Trotter-decomposition algorithm [223]. Although the method uses a perturbation series expansion, it takes account of all the contributions of the interaction, since the maximum perturbation order taken into account is higher than the order of the samples above which the weight is virtually zero. So the scheme is essentially nonperturbative.

Rubtsov *et al.* [231] proposed another algorithm to evaluate a series expansion of the partition function and applied it to the DMFT. The algorithm does not involve any auxiliary fields but uses Wick's theorem. Although the algorithm suffers sign problem even in the single-orbital DMFT, it has advantages in treating interactions nonlocal in space and in time. Recently Werner *et al.* [232] proposed to use a perturbation series expansion with respect to the hybridization function. Since the algorithm can treat strong-coupling region efficiently, it is also a powerful method for multiorbital systems.

In previous work [233], the present author first extended Rombouts' algorithm to the multiorbital Hubbard Hamiltonian (2.9), i.e., we expanded the Boltzmann operator with respect to the total interaction  $\hat{H}_U + \hat{H}_J$  shifted by a constant, which we decoupled with the Hubbard-Stratonovich transformation for  $\hat{H}_U$  and with a similar transformation as in Ref. [156] [Eq. (3)] for  $\hat{H}_J$ . Then we discretized the imaginary time  $\beta = L\Delta\tau$  and used a Hirsch-Fye-like updating algorithm for solving the impurity problem in the DMFT context. Although the method significantly relaxes the sign problem and can handle, in principle, more than two orbitals, it turned out that the calculations are too heavy at low temperatures or for strong couplings, especially for more than two orbitals. That is because the computational effort increases with perturbation orders of samples appearing in the Monte Carlo simulation. This order can become very large (see Fig. 4.4 below) in multiorbital systems since there are many interactions:  $(2M - 1)M$  terms in  $\hat{H}_U$  and  $2(M - 1)M$  terms in  $\hat{H}_J$  per site, where  $M$  is the number of orbitals.

To overcome this difficulty, in the next section we propose to combine the HFQMC and the series expansion (SE) QMC methods, i.e., to adopt the series expansion for  $\hat{H}_J$ , while the standard Trotter decomposition for  $\hat{H}_U$ . This algorithm enables us not only to handle three or more orbitals but also to reach much lower temperatures or stronger couplings than HFQMC (Ref. [156]) or SEQMC calculations (Ref. [233]), even for two-orbital models.

## 4.5 The (Trotter + Series-expansion) algorithm

We start with the series expansion of the Boltzmann factor after Ref. [229]. However, here we perform this only for  $\hat{H}_J$  (Fig. 4.5) [234], i.e.,

$$\begin{aligned} e^{\gamma - \beta \hat{H}} &= e^{-\beta(\hat{H}_0 + \hat{H}_U) + \gamma - \beta \hat{H}_J} \\ &= e^{-\beta(\hat{H}_0 + \hat{H}_U)} + \sum_{k=1}^{\infty} \int_0^1 dt_k \cdots \int_0^{t_2} dt_1 \prod_{i=1}^k \left[ e^{-t_i \beta(\hat{H}_0 + \hat{H}_U)} (\gamma - \beta \hat{H}_J) e^{t_i \beta(\hat{H}_0 + \hat{H}_U)} \right] e^{-\beta(\hat{H}_0 + \hat{H}_U)}, \end{aligned} \quad (4.30)$$

where we have shifted the Boltzmann factor by a constant  $\gamma$  for  $\beta \hat{H}_J$  to apply the auxiliary-field transformation (4.37) below.

Now we discretize the imaginary-time integrals and with the notation  $\hat{X}_1 \equiv \gamma - \beta \hat{H}_J$ , Eq. (4.30) equals to

$$e^{-\beta(\hat{H}_0 + \hat{H}_U)} + \sum_{k=1}^{\infty} L^{-k} \sum_{j_k=1}^L \cdots \sum_{j_1=1}^{j_2} \prod_{i=1}^k \left[ e^{-j_i \Delta \tau (\hat{H}_0 + \hat{H}_U)} \hat{X}_1 e^{j_i \Delta \tau (\hat{H}_0 + \hat{H}_U)} \right] e^{-\beta(\hat{H}_0 + \hat{H}_U)} + O(\Delta \tau). \quad (4.31)$$

We now show that this sum can be rewritten as

$$\sum_{s_1, \dots, s_L}^{0,1} F(k; s_1, s_2, \dots, s_L) \prod_{i=1}^L \left[ e^{-\Delta \tau (\hat{H}_0 + \hat{H}_U)} \hat{X}_{s_i} \right] + O(\Delta \tau), \quad (4.32)$$

where  $F$  is a positive weight factor,  $k \equiv \sum_{i=1}^L s_i$ , and  $\hat{X}_0 \equiv 1$ . To obtain the representation (4.32), we first cut off the  $k$  summation in Eq. (4.31) at  $L$ . This cutoff is justified if  $L$  is taken to be greater than the maximum perturbation order  $k_{\max}$  (defined and displayed below) appearing in the Monte Carlo samples, so that there are no contributions from higher-order terms. In practice, we can make  $L$  much larger than  $k_{\max}$  (see Fig. 4.4 below):  $k_{\max}$  depends on Hund's coupling  $J$ , where  $J$  is physically not so large, whereas we can choose  $L$  to satisfy  $L > \beta U$ .

Second, we replace those terms having consecutive  $\hat{X}_1$ 's in Eq. (4.31) by proximate terms including only one  $\hat{X}_1$  per imaginary time interval  $\Delta \tau$ . For example,  $\cdots \hat{X}_1 \hat{X}_1 e^{-\Delta \tau (\hat{H}_0 + \hat{H}_U)} \cdots$  is replaced by  $\cdots \hat{X}_1 e^{-\Delta \tau (\hat{H}_0 + \hat{H}_U)} \hat{X}_1 \cdots$ . This replacement reduces the number of possible configurations remarkably and casts the summation (4.31) into the form (4.32) similar to the Trotter decomposition, which enables us to employ their standard Hirsch-Fye algorithm with only a slightly more complicated auxiliary field at each time slice. The error involved in this approximation (commutation) is  $O(\Delta \tau)$ , i.e., of the same order as the time discretization, as long as the average order of the series expansion  $\langle k \rangle$  is sufficiently smaller than  $L$ . This is simply because the terms having two or more consecutive  $\hat{X}_1$ 's rarely appear for  $\langle k \rangle \ll L$ . For example, consider the second-order terms in Eq. (4.31). There are altogether  $L(L+1)/2$  second-order terms, but only  $L$  of these terms have two consecutive  $\hat{X}_1$ 's in the same imaginary time interval. Hence the error is

$$\begin{aligned}
& e^{-\beta(\hat{H}_0 + \hat{H}_U) + \gamma - \beta \hat{H}_J} \\
&= \sum_k \int d\tau \int d\tau' \dots \left[ e^{-(\tau' - \tau)(\hat{H}_0 + \hat{H}_U)} (\gamma - \beta \hat{H}_J) e^{-(\tau' - \tau)(\hat{H}_0 + \hat{H}_U)} (\gamma - \beta \hat{H}_J) \dots \right] \\
& \quad \swarrow \quad \quad \quad \nwarrow \quad \quad \quad \nearrow \\
& \text{Series expansion} \quad \quad \quad \simeq \prod e^{-\Delta\tau \hat{H}_0} e^{-\Delta\tau \hat{H}_U} : \text{Trotter decomposition} \\
& \text{in } \gamma - \beta \hat{H}_J
\end{aligned}$$

Figure 4.1: The (Trotter + Series-expansion) QMC method.

at most  $O(2\Delta\tau/L)$ . Similar argument for higher orders justify the replacement as long as  $\langle k \rangle \ll L$ . Since we do not simply drop the terms with two or more consecutive  $\hat{X}_1$ 's, but replace them by terms where the  $\hat{X}_1$ 's are shifted to neighboring imaginary time intervals, we have to multiply the Boltzmann factor by a factor  $F$  to account for these replacements. The detailed derivation of  $F$  is given in the Appendix.

Now, we separate out  $\hat{H}_U$  in Eq. (4.32) using the Trotter decomposition as

$$e^{-\Delta\tau(\hat{H}_0 + \hat{H}_U)} = e^{-\Delta\tau \hat{H}_0} e^{-\Delta\tau \hat{H}_U} + O(\Delta\tau^2), \quad (4.33)$$

so that Eq. (4.32) has a similar form to the standard HFQMC method. The  $e^{-\Delta\tau \hat{H}_U}$  term is then decoupled, as usual, into a sum of one-body exponentials with the Hubbard-Stratonovich transformation,

$$e^{-\Delta\tau V [n_\alpha n_\beta - \frac{1}{2}(n_\alpha + n_\beta)]} = \frac{1}{2} \sum_s^{\pm 1} \begin{cases} e^{\lambda_V s (n_\alpha - n_\beta)} & (V \geq 0), \\ e^{\lambda_V s (n_\alpha + n_\beta - 1) + \frac{q}{2}} & (V < 0), \end{cases} \quad (4.34)$$

where  $V$  stands for  $U$ ,  $U'$  or  $U' - J$ , and  $\lambda_V \equiv \ln(e^{|\Delta\tau V|/2} + \sqrt{e^{|\Delta\tau V|} - 1})$ . We have also displayed the case of attractive interaction ( $V < 0$ ), which we shall require when we do the procedure described in the footnote below Eq. (4.40). Including all the  $(2M - 1)M$  interactions of density-density type, the decoupling for  $e^{-\Delta\tau \hat{H}_U}$  is given by

$$\begin{aligned}
e^{-\Delta\tau \hat{H}_U} &= \sum_{P=1}^{N_U} \hat{Q}_P^U, \\
\hat{Q}_P^U &\equiv \frac{1}{N_U} \prod_{m=1}^M e^{\lambda_U p_m (n_{m\uparrow} - n_{m\downarrow})} \prod_{\sigma < \sigma', \sigma} e^{\lambda_{U'} q_\sigma^{mm'} (n_{m\sigma} - n_{m',-\sigma}) + \lambda_{U'-J} r_\sigma^{mm'} (n_{m\sigma} - n_{m'\sigma})},
\end{aligned} \quad (4.35)$$

where  $P [= 1, \dots, N_U \equiv 2^{(2M-1)M}]$  designates a configuration of the auxiliary-field set  $(\{p_m\}, \{q_\sigma^{mm'}\}, \{r_\sigma^{mm'}\})$  with  $p_m$ ,  $q_\sigma^{mm'}$  and  $r_\sigma^{mm'} (= \pm 1)$  denoting the fields for the  $U$ ,  $U'$  and  $U' - J$  terms, respectively.

For  $\hat{X}_1 = \gamma - \beta\hat{H}_J$  in Eq. (4.32) we construct an auxiliary-field transformation as follows [233]. We first decompose  $\hat{X}_1$  into the sum of all distinct two-orbital parts as

$$\begin{aligned}\gamma - \beta\hat{H}_J &= \sum_{m < m'} (\gamma^{mm'} - \beta\hat{H}_J^{mm'}), \\ \gamma &\equiv \sum_{m < m'} \gamma^{mm'}.\end{aligned}\quad (4.36)$$

We then apply the decoupling

$$\gamma^{mm'} - \beta\hat{H}_J^{mm'} = \frac{\gamma^{mm'} - \beta J}{8} \sum_{s, t_\uparrow, t_\downarrow}^{\pm 1} \prod_{\sigma} e^{\tilde{\lambda}_J [\sigma s \hat{f}_{\sigma}^{mm'} + t_{\sigma} (n_{m\sigma} + n_{m'\sigma} - 1)]} \quad (4.37)$$

to every pair of orbitals, where

$$\begin{aligned}\hat{f}_{\sigma}^{mm'} &\equiv c_{m\sigma}^{\dagger} c_{m'\sigma} + c_{m'\sigma}^{\dagger} c_{m\sigma}, \\ \tilde{\lambda}_J &\equiv \frac{1}{2} \ln \frac{1 + \kappa}{1 - \kappa}, \\ \kappa &\equiv \sqrt{\frac{\beta J}{\gamma^{mm'}}} < 1.\end{aligned}\quad (4.38)$$

Combining Eqs. (4.36) and (4.37), we end up with

$$\begin{aligned}\gamma - \beta\hat{H}_J &= \sum_{S=1}^{N_J} \hat{Q}_S^J, \\ \hat{Q}_S^J &\equiv \frac{\gamma^{mm'} - \beta J}{8} \prod_{\sigma} e^{\tilde{\lambda}_J [\sigma s \hat{f}_{\sigma}^{mm'} + t_{\sigma} (n_{m\sigma} + n_{m'\sigma} - 1)]},\end{aligned}\quad (4.39)$$

where  $S [= 1, \dots, N_J \equiv 4M(M-1)]$  corresponds to the set  $(s, t_{\uparrow}, t_{\downarrow})$  for all the  $M(M-1)/2$  pairs of orbitals  $(m, m')$ . We stress here that the decoupling (4.39) treats every two-orbital parts,  $\hat{H}_J^{mm'}$ 's, in  $\hat{H}_J$  on an equal footing. This is not achieved by the HFQMC based on the Trotter decomposition because of the noncommutativity of  $\hat{H}_J^{mm'}$ 's. Namely, in the HFQMC, even if we rewrite  $e^{-\Delta\tau\hat{H}_J}$  into the form  $\prod_{m < m'} e^{-\Delta\tau\hat{H}_J^{mm'}}$  at the expense of an error  $O(\Delta\tau^2)$ , the unequal treatment of the interorbital interactions  $\hat{H}_J^{mm'}$  may cause a problem. This difficulty is lifted in Eq. (4.36), so that we can readily deal with more than two orbitals.

Collecting the addenda from the decoupled  $\hat{H}_U$  and  $\hat{H}_J$  terms, we finally obtain

$$e^{\gamma - \beta\hat{H}} = \sum_{S_1, \dots, S_L}^{0, \dots, N_J} F(k; \tilde{s}_1, \tilde{s}_2, \dots, \tilde{s}_L) \sum_{P_1, \dots, P_L}^{1, \dots, N_U} \prod_{i=1}^L e^{-\Delta\tau\hat{H}_0} \hat{Q}_{P_i}^U \hat{Q}_{S_i}^J + O(\Delta\tau), \quad (4.40)$$

with  $\hat{Q}_0^J \equiv 1$ , where we have extended the region of the value of  $S_i$  as  $\tilde{s}_i \equiv 0$  for  $S_i = 0$ , and  $\tilde{s}_i \equiv 1$  for  $S_i = 1, \dots, N_J$ .<sup>2</sup> Note that because  $F(0; 0, \dots, 0) = 1$ , the zeroth-order

<sup>2</sup>In practice we can further reduce the number of auxiliary fields:  $t_{\uparrow}$  and  $t_{\downarrow}$  in Eq. (4.37) are not necessary when we combine these terms with  $U' - J$  terms in Eq. (4.35) to decouple them simultaneously.

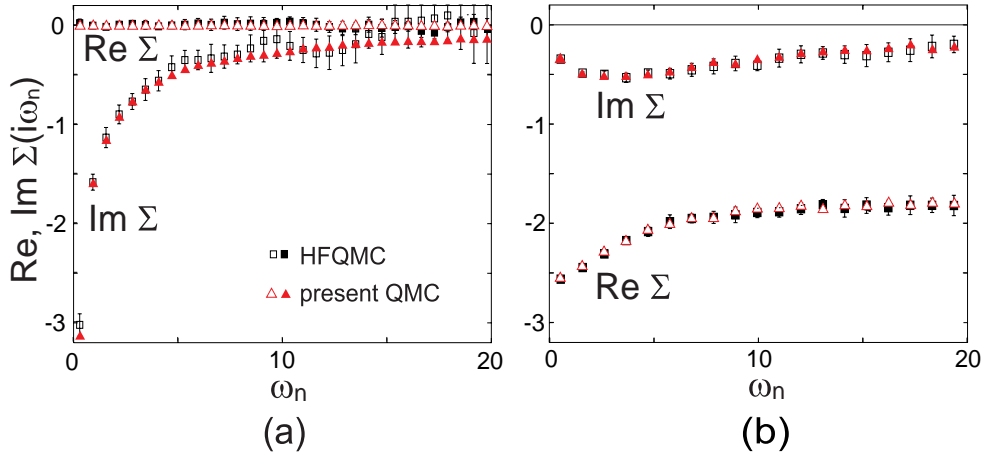


Figure 4.2: Real and imaginary parts of the self-energy against the Matsubara frequency  $\omega_n$  for the two-orbital Hubbard model for (a) an insulating case with  $n = 2$ ,  $\beta = 10$ ,  $U' = 2$ ,  $J = 0.4$ , and (b) a metallic case with  $n = 1$ ,  $\beta = 6$ ,  $U' = 2$ ,  $J = 1$ . Result with the Hirsch-Fye algorithm (Ref. [156]) is shown with black squares, and the present QMC result with red triangles. (From Ref. [234].)

term in Eq. (4.40) reproduces the Hirsch-Fye algorithm with Ising-type Hund's coupling. Owing to the form of Eq. (4.40), which is similar to the Trotter decomposition formula (4.4), we can apply the same algorithm as in HFQMC for the Monte Carlo sampling. Even the updating equations for single auxiliary-field flips are the same.

## 4.6 Applicable region for the algorithm

As a benchmark, we compare in Fig. 4.2 the electron self-energy obtained with our algorithm to that with the HFQMC method in Ref. [156] for the two-orbital Hubbard model [234]. We chose the hypercubic lattice with the effective bandwidth  $W_{\text{eff}} = 2\sqrt{2}$ , and took  $6 \times 10^6$  Monte Carlo samples for both methods. We can see that the two results agree with each other within error bars for both (a) an insulating case at half filling  $n = 2$  with  $\beta = 10$ ,  $U' = 2$ ,  $J = 0.4$ ,  $L = 100$ , and (b) a metallic case at  $n = 1$ ,  $\beta = 6$ ,  $U' = 2$ ,  $J = 1$ ,  $L = 64$ .

We notice, however, that the statistical error is much smaller in the present QMC than in the HFQMC. This is because the number of negative signs is greatly reduced in the present scheme: The sign problem is mitigated. Quantitatively, the average sign (4.27) in the QMC weights is 0.01(0.03) for HFQMC methods while they are increased to 0.30(0.50) in the present algorithm in case (a)[(b)]. This also implies that the present method can reach much lower temperatures. We note that, while  $\gamma (> \beta V)$  is arbitrary, the computation becomes more efficient when  $\gamma - \beta V$  is small. However, since too small  $\gamma - \beta V$  causes a large round-off error, we adopted in these and following calculations  $\gamma - \beta V \sim 0.1-0.3$ , which has turned out to suppress both the error and the computational time.

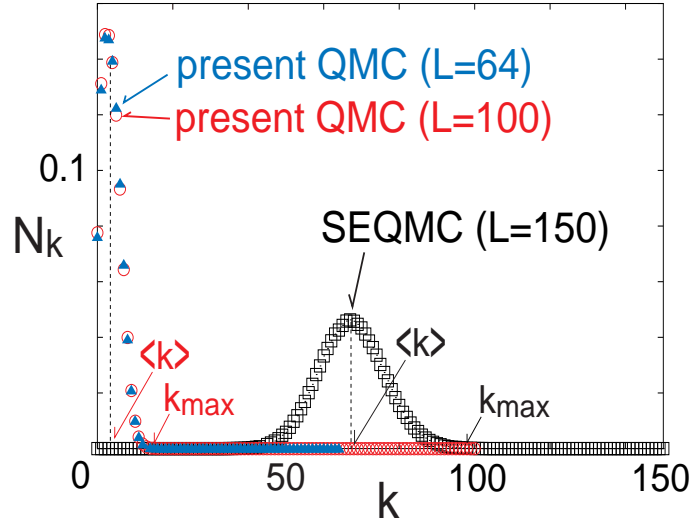


Figure 4.3: The distribution  $N_k$  of the order of perturbation  $k$  for the two-orbital Hubbard model with  $n = 1.9$ ,  $\beta = 8$ ,  $U' = 4$ ,  $J = 0.2$  obtained with the present algorithm ( $L = 64$  or  $100$ ) and with the SEQMC algorithm ( $L = 150$ , Ref. [233]) (from Ref. [234]).

Figure 4.3 depicts a typical distribution  $N_k$  of the order of perturbation  $k$  contributing in the Monte Carlo simulation for  $n = 1.9$ ,  $\beta = 8$ ,  $U' = 4$ ,  $J = 0.2$ . In the SEQMC, a peak in the distribution resides at around  $k = 70$ . On the other hand, the present (Trotter+SE) QMC has a peak at around  $k = 2$ , which is much smaller than that in SEQMC. This is natural, since the present method uses the expansion only with respect to  $\hat{H}_J$ , while the SEQMC method expands with respect to the total interaction  $\hat{H}_U + \hat{H}_J$ . The maximum order in the distribution is found to be  $k_{\max} \sim 100$  for the SEQMC method, while  $k_{\max} \sim 15$  is much lowered for the present QMC method. This means that  $L$  must be taken to be  $> 100$  for the SEQMC method to take care of all orders, while  $L > \beta U \sim 35$  suffices for the present algorithm to take care of all orders. Such a smaller value of  $L$  dramatically reduces the computational effort in QMC simulations, which increases proportionately to  $L^3$ . The weight is virtually zero above  $k_{\max}$ , in actual simulations, so that, although the method exploits the perturbation-series expansion, it takes account of *all orders* in fact. Moreover, the average order  $\langle k \rangle$  is as low as 4 for the present QMC, which means that the approximation employed to obtain the form (4.32) has only a very minor effect on the results, and hence is justifiable. This can also be confirmed from the fact that the results do not significantly depend on  $L$ .

Figure 4.4 shows the computable regions for the present QMC and for the HFQMC methods (Ref. [156]) when  $\hat{H}_J$  is included. Here we define the region as computable when the average sign is greater than 0.01. We can see that a much wider parameter region becomes computable in the present algorithm than in the HFQMC method. For small  $J$  ( $\lesssim 0.2$ ), we can explore  $\frac{1}{5}$  to  $\frac{1}{10}$  times lower temperatures. We attribute this improvement to the fact that  $\hat{H}_J$  (which is the source of negative weights) appears  $L$  times for every sample in the HFQMC method, while we have only  $\langle k \rangle$  such terms on average

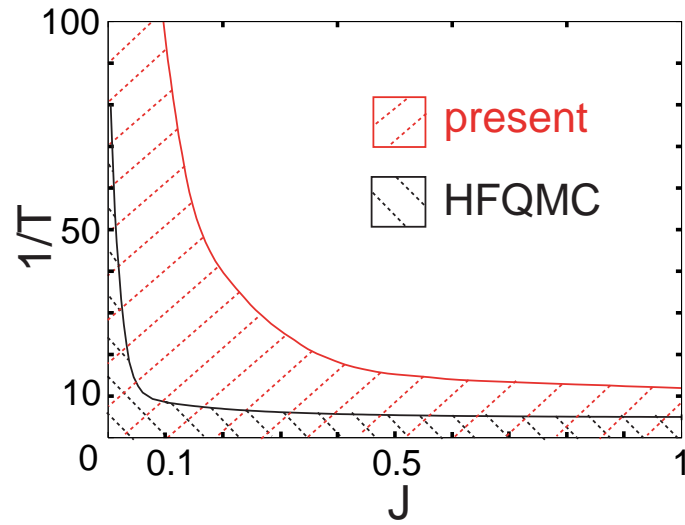


Figure 4.4: Computable regions (hatched) in the  $T$ (temperature)- $J$ (Hund's coupling) parameter space that can be computed with the present and with the Hirsch-Fye QMC methods (Ref. [156]) for the two-orbital Hubbard model with  $U' = 4$ ,  $W_{\text{eff}} = 2\sqrt{2}$ . Here we define the computability by requiring the average sign to be greater than 0.01. (From Ref. [234].)

in the present QMC algorithm.

# Chapter 5

## Itinerant ferromagnetism in multiorbital systems

We applied the QMC algorithm developed in §4.5 to the study of itinerant ferromagnetism in multiorbital systems.

In §5.1.1 we elaborate our motivation. We review preceding studies on ferromagnetism in the single- and multiorbital Hubbard models in §5.1.2 and in §5.1.3, respectively. §5.2 is devoted to the comparison of the results between Ising and SU(2) Hund's couplings. We discuss effects of Hund's coupling on ferromagnetic instability in §5.3. We summarize the results in §5.4.

### 5.1 Introduction

#### 5.1.1 Motivation

In this chapter, we explore metallic ferromagnetism in the multiorbital Hubbard model (2.9) on an fcc lattice, with our eyes set on the itinerant ferromagnetism in transition metals and transition-metal oxides, especially in fcc Ni.

As we shall describe in detail in §5.1.2, the single-orbital Hubbard model has long been studied as the minimum microscopic model that includes the essence of itinerant ferromagnetism in transition-metal-based materials. However, as a consequence of vast research, it has been recognized that the single-orbital Hubbard model on simple lattices does not easily show ferromagnetism for realistic values of interaction  $U$ . Then, in order to explain itinerant ferromagnetism in real materials, many authors have considered ingredients other than the Hubbard interaction  $U$ . The two factors are now considered to be significant; *lattice structures and the degeneracy of  $d$  orbits*.

Kanamori [30] suggested that a lattice structure (in particular, the shape of the density of states), as well as the Coulomb interaction, is crucial for the stability of ferromagnetism. He discussed the itinerant ferromagnetism in fcc Ni, whose density of states has a peak at the upper band edge, and suggested that this peak structure of the DOS stabilizes the ferromagnetism. (This topic is discussed in more detail in §5.1.2.)

On the other hand, the importance of the degeneracy of  $d$  orbitals has long been emphasized for transition-metal-based ferromagnets [38, 39], where Hund's exchange coupling is considered to stabilize the ferromagnetism. However, the complexity of the multiorbital Hubbard model has restricted studies only in one dimension or with drastic approximations such as strong-coupling limit. (This topic is discussed in more detail in §5.1.3.) Hence, we do not have a reasonable estimate for the effect of the orbital degeneracy in three-dimensional systems in an intermediate-coupling ( $U \sim W$ ) region, which corresponds to transition metals and their compounds.

Here we discuss the long standing issue whether either lattice structure or orbital degeneracy can explain itinerant ferromagnetism in transition-metal-based materials. To address the problem, we study the double-orbital Hubbard model on the simple cubic and the fcc lattices, using the DMFT combined with the QMC algorithm proposed in §4.5.

Before turning to the problem, we discuss in §5.2 a difference in the ferromagnetic instability between Ising and SU(2) Hund's couplings. The result explicitly shows the importance of the spin and orbital rotational symmetries in the Hamiltonian (2.9), which are difficult to treat with the conventional Hirsch-Fye QMC method but become tractable in the QMC algorithm developed in §4.5.

### 5.1.2 Metallic ferromagnetism in the single-orbital Hubbard model

As mentioned in §1.2.2, there are several rigorous proofs of the existence of ferromagnetism in the single-orbital Hubbard model [32]; Nagaoka ferromagnetism, ferrimagnetism and flat-band ferromagnetism. However, these are proved only in a few restricted situations. Hence it is still an open question whether ferromagnetism exists in the single-orbital Hubbard model for an intermediate coupling on an ordinary lattice. We review here some approximate theories for this problem.

#### · *Hartree-Fock approximation*

The Hartree-Fock approximation for the single-orbital Hubbard model leads to the Stoner criterion for ferromagnetism [10],

$$UD(E_F) > 1, \quad (5.1)$$

where  $D(E_F)$  is the density of noninteracting electron states at the Fermi energy  $E_F$ . However, the Hartree-Fock approximation considerably overestimates the stability of ferromagnetism since electron correlation effects, which lower the energy of paramagnetic states against the ferromagnetism, are neglected in this approximation.

#### · *Gutzwiller approximation*

In order to discuss correlation effects in the single-orbital Hubbard model, Gutzwiller [31] introduced a variational wave function,

$$\psi = \prod_i [1 - (1 - g)n_{i\uparrow}n_{i\downarrow}] \psi_0, \quad (5.2)$$

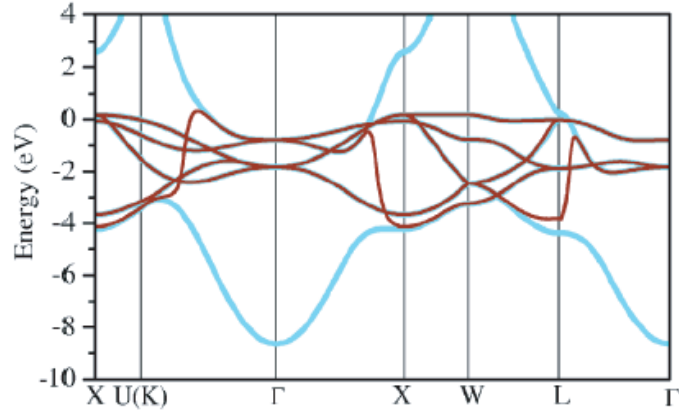


Figure 5.1: The bandstructure of (paramagnetic) fcc Ni calculated by Solovyev and Imada [236]. The LDA bands are shown with light color while the GW bands, which are described by five pseudo-Wannier orbitals of predominantly  $3d$  character, are shown with dark color. (After Ref. [236].)

where  $g$  is a variational parameter ( $0 \leq g \leq 1$ ) controlling the number of doubly occupied sites, and  $\psi_0$  is the ground state for  $U = 0$ . Gutzwiller determined  $g$  in a statistical consideration, and applied the approximation to the model on a three-dimensional face-centered cubic (fcc) lattice whose density of states (DOS) has a peak near the upper band edge. He found a ferromagnetic state only for nearly full bands for a rather large  $U$  ( $\gtrsim 2W$ ,  $W$ : bandwidth). For a square lattice in two and three dimensions, the Gutzwiller approximation leads to ferromagnetism only for very large  $U$  ( $\gtrsim 7W$ ) [235]. These results show that, in the presence of electron correlations, ferromagnetism requires much severer condition than (5.1), and that the occurrence of ferromagnetism strongly depends on lattice structures.

· *Kanamori theory (T-matrix approximation)*

Similar conclusion was obtained by Kanamori [30], who discussed the ferromagnetism in Ni with the  $T$ -matrix approximation. Nickel has an fcc structure with eight electrons in five  $3d$  orbitals. Since the  $d$  orbitals are almost degenerate (see Fig. 5.1), each  $d$  band has about 0.4 holes in total of up and down spins. While the density of electron states in Ni has a peak at the upper band edge, in the following discussion, we consider the DOS which has a peak at the lower band edge (Fig. 5.2).

Kanamori investigated the single-orbital Hubbard model with 0.4 particles on an fcc lattice, which corresponds to the Ni case after the electron-hole transformation. The  $T$ -matrix approximation takes account of multiple scatterings between electrons only through a two-particle propagator in the particle-particle (pp) channel (the Feynman diagrams as represented in Fig. 5.3),

$$\chi^{\text{pp}}(q) = \frac{T}{N} \sum_k G(k+q)G(-k), \quad (5.3)$$

where  $N$  is the system size, and  $k$  and  $q$  denote  $(\mathbf{k}, i\omega)$  and  $(\mathbf{q}, i\nu)$ , respectively. Then the

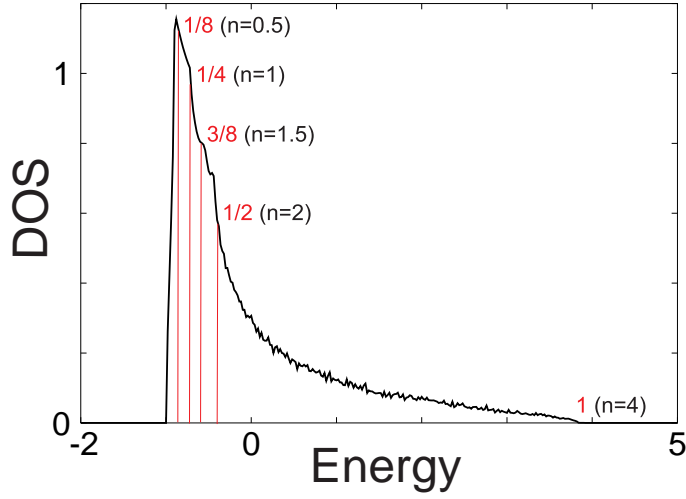


Figure 5.2: The density of states for noninteracting electrons on the fcc lattice considered in this section. The red numbers represent the filling of the band. The black numbers denote the corresponding total band filling for two-orbital systems.

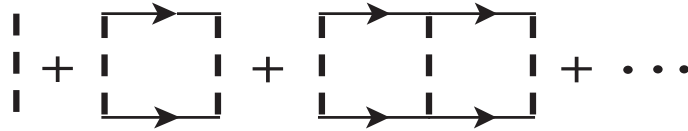


Figure 5.3: The Feynman diagrams for the particle-particle scatterings included in the  $T$ -matrix approximation. A dashed line represents the Hubbard interaction  $U$ , and a full line represents Green's function for a non-interacting electron.

electron self-energy is written as

$$\begin{aligned}\Sigma(k) &= \frac{T}{N} \sum_q G(-k+q) V^{\text{pp}}(q), \\ V^{\text{pp}}(q) &\equiv -U^2 \chi^{\text{pp}}(q) \left[ \frac{1}{1 + U \chi^{\text{pp}}(q)} - 1 \right].\end{aligned}\quad (5.4)$$

This approximation becomes exact in the dilute limit because the contribution from holes is neglected in this limit.

The particle-particle scattering modifies the condition (5.1) into

$$\frac{U}{1 + U \chi^{\text{pp}}(0)} D(E_F) > 1, \quad (5.5)$$

where we approximated  $\chi^{\text{pp}}(q)$  by  $\chi^{\text{pp}}(0)$ . The condition (5.5) means that a large  $U$  alone does not guarantee ferromagnetism, unlike the Stoner condition (5.1), and that it depends strongly on shapes of the DOS. Kanamori discussed the ferromagnetism in fcc Ni, and concluded that the shape of the fcc DOS is favorable for the condition (5.5), since it

has both a peak at around  $E_F$  and a relatively wide bandwidth, which reduces  $\chi^{\text{pp}}$  in the denominator on the left hand side of the condition (5.5).

In the Kanamori theory, the degeneracy of  $d$  orbitals has been neglected since the degeneracy has only minor effects on the stability of ferromagnetism in the  $T$ -matrix approximation. Following the discussion by Kanamori, let us consider the energy shift, induced by interactions  $U$ ,  $U'$  and  $J$ , for an electron pair added onto the Fermi sphere. First we consider a spin-triplet pair in the momentum space across different orbitals  $m$  and  $m'$ . In the  $T$ -matrix approximation the energy shift  $\Delta^{\text{triplet}}$  from the noninteracting state is given by

$$\Delta^{\text{triplet}} = \frac{1}{N} \frac{U' - J}{1 + (U' - J)\chi_{mm'}^{\text{pp}}}, \quad (5.6)$$

where we abbreviated the momentum dependence. On the other hand, the energy shift for a spin-singlet pair across orbitals is given by

$$\Delta^{\text{singlet}} = \frac{1}{2N} \left[ \frac{U' + J}{1 + (U' + J)\chi_{mm'}^{\text{pp}}} + \frac{U' - J}{1 + (U' - J)\chi_{mm'}^{\text{pp}}} \right]. \quad (5.7)$$

Then the energy reduction of the triplet from the singlet is

$$\begin{aligned} \Delta^{\text{triplet}} - \Delta^{\text{singlet}} &= \frac{1}{2N} \left[ \frac{U' + J}{1 + (U' + J)\chi_{mm'}^{\text{pp}}} - \frac{U' - J}{1 + (U' - J)\chi_{mm'}^{\text{pp}}} \right] \\ &\approx -\frac{1}{N} \frac{J}{(1 + U'\chi_{mm'}^{\text{pp}})^2} \quad (J \ll U'). \end{aligned} \quad (5.8)$$

Since the factor  $(1 + U'\chi_{mm'}^{\text{pp}})^{-2}$  is considered to be small (Kanamori [30] evaluated the factor to be less than 0.1), the contribution of  $J$  to ferromagnetism is negligible in the  $T$ -matrix approximation. This conclusion is, however, only applicable for sufficiently low band fillings, where *particle-hole scatterings* do not play a significant role. For a general band filling, Hund's coupling and the pair-hopping  $J$  can crucially contribute to ferromagnetism through the particle-hole scatterings, as we shall discuss in §5.3.1.

· *Fluctuation-exchange approximation*

Arita *et al.* [143] examined ferromagnetism in the single-orbital Hubbard model by means of the fluctuation-exchange (FLEX) approximation [44]. The FLEX takes into account multiple scatterings in the particle-hole channel (the bubble diagrams [Fig. 5.4(a)] and the particle-hole ladder diagrams [Fig. 5.4(b)]) as well as those in the particle-particle

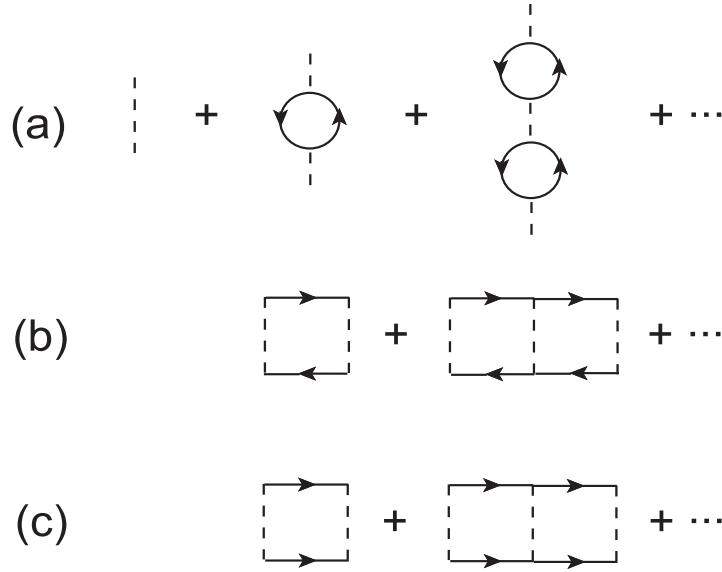


Figure 5.4: The Feynman diagrams included in the FLEX approximation: (a) Bubble, (b) particle-hole ladder, (c) particle-particle ladder diagrams.

channel [Fig. 5.4(c)]. Then the self-energy is given by

$$\begin{aligned}
\Sigma(k) &= \frac{T}{N} \sum_q \left[ G(k-q)V^{\text{ph}}(q) + G(-k+q)V^{\text{pp}}(q) \right], \\
V^{\text{ph}}(q) &\equiv \frac{U^2\chi^{\text{ph}}(q)}{1-U^2\chi^{\text{ph}}(q)^2} + U^2\chi^{\text{ph}}(q) \left[ \frac{1}{1-U\chi^{\text{ph}}(q)} - 1 \right] \\
&= \frac{3}{2}U^2 \frac{\chi^{\text{ph}}(q)}{1-U\chi^{\text{ph}}(q)} + \frac{1}{2}U^2 \frac{\chi^{\text{ph}}(q)}{1+U\chi^{\text{ph}}(q)} - U^2\chi^{\text{ph}}(q), \\
\chi^{\text{ph}}(q) &= -\frac{T}{N} \sum_k G(k+q)G(k). \tag{5.9}
\end{aligned}$$

Notice that in the particle-hole channel the effect of  $U$  is amplified by a factor  $(1-U\chi^{\text{ph}})^{-1}$ . Since the FLEX approximation omits vertex corrections for the self-energy (e.g., Fig. 5.5), it is only reliable for weak-coupling regions. Arita *et al.* compared a ferromagnetic and an antiferromagnetic instabilities in a weak-coupling region for the fcc, body-centered cubic (bcc), and simple cubic lattices in three dimensions. The result shows that the ferromagnetic instability is most enhanced in the fcc lattice, while the antiferromagnetic instability appears for the bipartite bcc and simple cubic lattices, where the instability is stronger in the bcc lattice than in the simple cubic lattice. The ferromagnetic instability for the fcc lattice becomes largest for a low band filling ( $n \sim 0.2$ ), where the Fermi energy is near the peak of the DOS (Fig. 5.2). They confirmed their FLEX results with the two-particle self-consistent approximation, which includes a contribution from the vertex corrections.

· *Dynamical mean-field approximation*

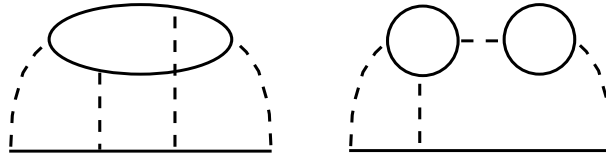


Figure 5.5: An example of the self-energy diagrams omitted in the FLEX.

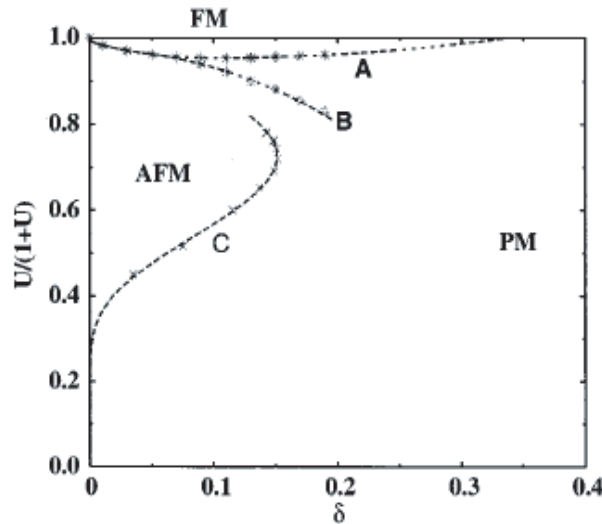


Figure 5.6: Magnetic phase diagram for the  $d = \infty$  single-orbital Hubbard model on the hypercubic lattice with  $W_{\text{eff}} = 2\sqrt{2}$ , obtained by Obermeier *et al.* [141]. The ordinate is the Coulomb interaction, where  $U/(1+U) = 1$  corresponds to the strong coupling limit, while the abscissa is a hole-doping from the half filling, i.e.,  $\delta = 1 - n$  ( $n$ : band filling). PM, FM and AFM denote paramagnetic, ferromagnetic and antiferromagnetic phases, respectively. (After Ref. [141].)

By contrast to the above  $T$ -matrix and FLEX theories, the dynamical mean-field theory (DMFT) can treat intermediate and strong couplings so that it can describe the Mott transition. Some authors have investigated ferromagnetic instabilities with the DMFT for the infinite-dimensional Hubbard model. For hypercubic lattices no ferromagnetism has been found at any band filling for  $U \lesssim 3W$  [22, 140]. Obermeier *et al.* [141] investigated the large  $U$  limit with the DMFT + non-crossing approximation (NCA) method, and found a ferromagnetism for fillings slightly doped from the half filling ( $n=1$ ). Figure 5.6 is the magnetic phase diagram obtained by Obermeier *et al.* A ferromagnetic region appears for large  $U$  ( $\gtrsim 7W$ ) bordered by an antiferromagnetic region. Obermeier *et al.* discussed the ferromagnetism in relation to the Nagaoka state.

Meanwhile, Ulmke [142] studied fcc lattices in three and infinite dimensions with the DMFT+QMC method. He obtained a ferromagnetic state for a reasonable value of  $U$  ( $\sim W$ ). Figure 5.7 is the  $T$ - $n$  phase diagram for the three-dimensional fcc lattice with next-nearest-neighbor hopping  $t' = t/4$ , obtained by Ulmke. Similar phase diagram was

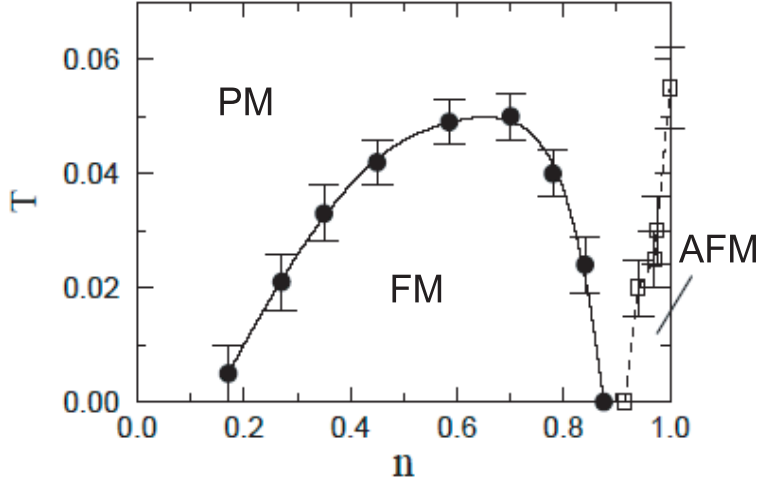


Figure 5.7: Magnetic  $T$ - $n$  phase diagram for the single-orbital Hubbard model on the  $d = 3$  fcc lattice with  $t' = t/4$  for  $U = 6$  ( $W_{\text{eff}} = 4$ ), obtained by Ulmke [142]. PM, FM and AFM denote paramagnetic, ferromagnetic and antiferromagnetic phases, respectively. (After Ref. [142].)

also obtained by Wegner *et al.* [237] with the DMFT + (third-order) iterative perturbation theory (IPT). They found that the Curie temperature  $T_c$  is highest for  $n \sim 0.6$  and it becomes almost zero for low fillings ( $n \lesssim 0.2$ ). This filling dependence differs from the  $T$ -matrix [30] and the FLEX results [143] in the weak-coupling region.

### 5.1.3 Ferromagnetism in the multiorbital Hubbard model

As described in §1.3, the inclusion of the orbital degrees of freedom can significantly affect spin states through Hund's exchange coupling. While Hund's coupling aligns two electron spins *on the same site*, it may become a cause for a long-range ferromagnetic order via electrons' motion through the crystal. Because most of transition-metal-based ferromagnets (not only Fe, Co, Ni but also  $\text{SrRuO}_3$ ,  $\text{La}_{1-x}\text{Sr}_x\text{CoO}_3$ , etc.) indeed have the  $d$ -orbital degeneracy, Hund's coupling may be playing a crucial role in the appearance of the ferromagnetism. For such a reason, many authors have addressed ferromagnetism in multiorbital systems.

#### · Ferromagnetism with orbital ordering at $n = 1$

Especially, two-orbital cases on a bipartite lattice at  $n = 1$  (i.e., one electron per atom) have attracted most intensive attentions since a ferromagnetic order involving an antiferro-orbital order is anticipated from a simple discussion on the kinetic exchange interaction (see §1.3.2). Roth [58] introduced a multiorbital Hubbard model which includes Hund's coupling, and showed the existence of the ferromagnetic state with the antiferro-orbital order in a strong coupling regime within the random phase approximation. The result was supported by the quantum Monte Carlo (QMC) simulation [238], the exact diagonalization (ED) [239, 240, 241] and the density-matrix renormalization-group (DMRG) method

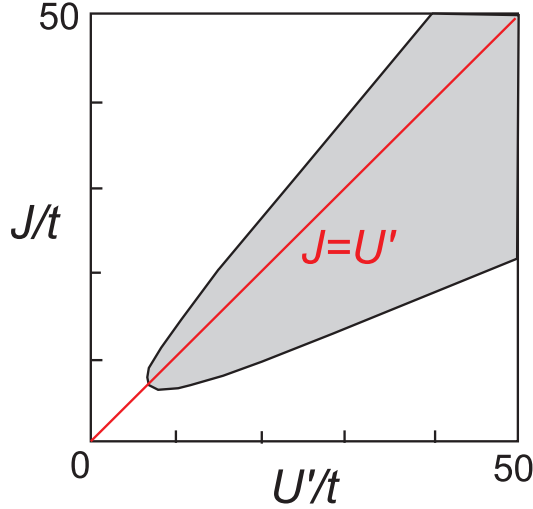


Figure 5.8: The ground-state phase diagram for the two-orbital Hubbard model with SU(2) Hund’s coupling and the pair-hopping term in one dimension for  $n = 1$ , obtained by Kusakabe and Aoki [239] with the exact diagonalization method for six-site system with the open-boundary condition. The shaded region represents ferromagnetic state, which is metallic on the line  $J = U'$  while insulating otherwise. The physical region is  $J < U'$ . Parameters are fixed as  $U = U' + J$ . (From Ref. [239].)

[242] for finite-size one-dimensional systems (Fig. 5.8).

Momoi and Kubo [172] investigated, with the DMFT+ED method, the  $d = \infty$  two-orbital Hubbard model on a hypercubic lattice, taking account of SU(2) Hund’s coupling and the pair-hopping interaction. For the quarter filling ( $n = 1$ ), they found a ferromagnetic ground state with the antiferro-orbital order for a strong coupling region ( $U \gtrsim 3W_{\text{eff}}$  and  $J \gtrsim W_{\text{eff}}/3$ ).

#### · *Metallic ferromagnetism*

However, the ferromagnetism with the antiferro-orbital order may be peculiar to two-orbital systems, and since the ferromagnetic state is insulating, it cannot account for the itinerancy in transition-metal-based ferromagnets. There have been a few studies for the metallic ferromagnetism in the multiorbital Hubbard model.

Kusakabe and Aoki [239] investigated, by means of the ED, the double-orbital Hubbard model with the SU(2)-Hund and pair-hopping interactions in one dimension. They showed the existence of itinerant ferromagnetism at  $n = 1$  for a specific parameter region  $J = U'$  (Fig. 5.8). They also mentioned that a doping of extra electrons drastically expands the region of the metallic ferromagnetism in the  $U'$ - $J$  plane. Hirsch [241] examined itinerant ferromagnetism away from quarter filling with the ED for one-dimensional chains. The result indicates that the Hund exchange by itself does not lead to a ferromagnetic state for a realistic parameter region for transition metals, so that he suggested the importance of interatomic exchange interactions. However, the one-dimensional calculation does not take account of the lattice structure of real materials, which is an important fac-

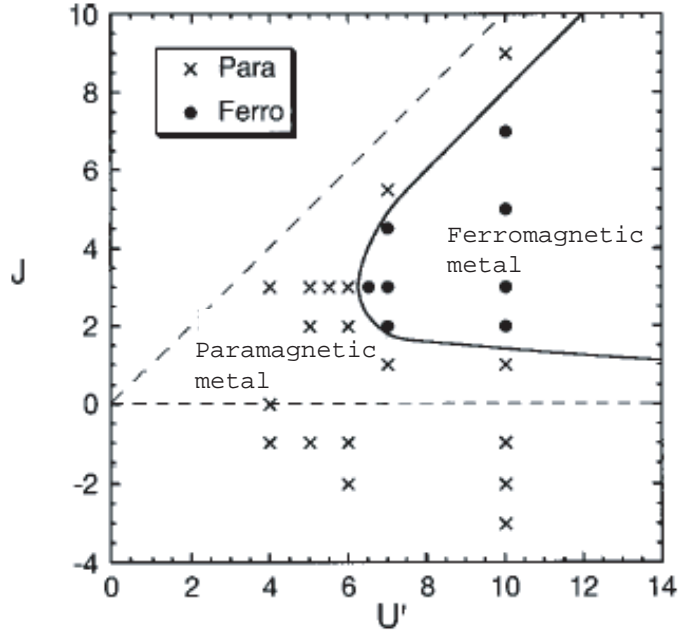


Figure 5.9: The ground-state phase diagram for the two-orbital Hubbard model with SU(2) Hund's coupling on a hypercubic lattice at  $n = 1.2$ , obtained with the DMFT+ED calculation by Momoi and Kubo [172]. The effective bandwidth  $W_{\text{eff}}$  is  $2\sqrt{2}$ . Parameters are fixed as  $U = U' + 2J$ . The physical region is  $0 < J < U'$ . (From Ref. [172].)

tor for multiorbital ferromagnetism, as we discuss below. Sakamoto *et al.* [242] studied a one-dimensional system with the DMRG method, and found itinerant ferromagnetism for  $J < U'$  from low to high electron densities ( $0 < n < 1.75$ ) except for  $n = 1$ , where the insulating ferromagnetism appears.

On the other hand, the infinite dimensional limit of the double-orbital Hubbard model has been investigated by some authors. Momoi and Kubo [172] have also applied the DMFT+ED method to study the doping effect to the  $n = 1$  insulating ferromagnet in the model with the SU(2) Hund and pair-hopping terms. They obtained metallic ferromagnetism in an electron-doped case ( $n = 1.2$ ) for rather strong interactions ( $U \gtrsim 4W_{\text{eff}}$  and  $J \gtrsim W_{\text{eff}}$ ) (Fig. 5.9). In a hole-doped case ( $n = 0.8$ ), however, no ferromagnetism was found for  $J \leq U' \lesssim 7W$ . Held and Vollhardt [164] adopted the model with Ising Hund's coupling on the Bethe lattice, which has a semielliptical DOS (3.8), and implemented a DMFT+(Hirsch-Fye)QMC calculation at finite temperatures. They calculated the spin and orbital susceptibilities in the paramagnetic phase, and determined phase boundaries from the temperatures at which the susceptibilities diverge. The obtained  $T$ - $n$  phase diagram (Fig. 5.10), where the interaction parameters are  $U = 2.25W$ ,  $U' = 1.25W$  and  $J = W$  (which hold a relation  $U = U' + J$ , instead of the relation (2.7)), shows that a metallic ferromagnetism appears in a wide range of filling,  $0.4 < n < 1.8$ . They mentioned that above the Curie temperature no orbital order was found for these interaction parameters even for  $n = 1$ , while the orbital order may appear below the Curie temper-

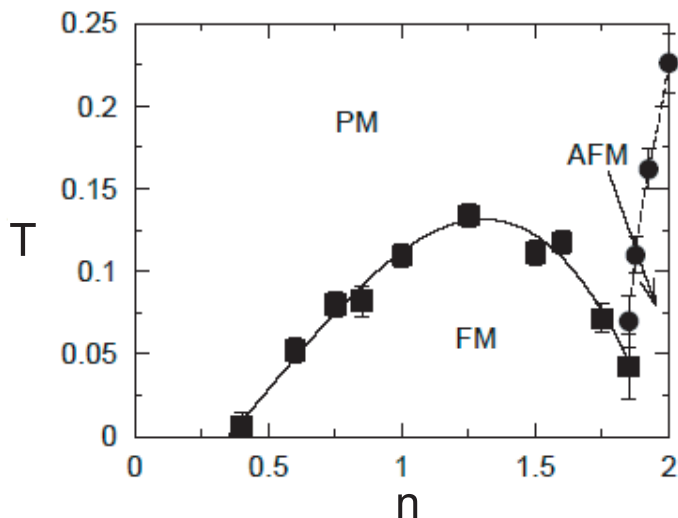


Figure 5.10: The magnetic  $T$ - $n$  phase diagram for the two-orbital Hubbard model with Ising Hund's coupling on the Bethe lattice with  $W = 4$ , obtained with the DMFT+HFQMC calculation by Held and Vollhardt [164]. Parameters are set to be  $U = 9$ ,  $U' = 5$  and  $J = 4$ . PM, FM and AFM denote paramagnetic, ferromagnetic and antiferromagnetic phases, respectively. (From Ref. [164].)

ature, which was not addressed by the calculation in the paramagnetic phase. Held and Vollhardt also examined a possibility of the orbital ordering in the paramagnetic phase, and found it near  $n = 1$  for smaller  $J$  than that used in Fig. 5.10. These DMFT results indicate that the itinerant ferromagnetism requires unrealistically large values of  $U$  and  $J$  on ordinary lattices.

A more realistic calculation was done by Bünemann *et al.* [243] with the Gutwiller approximation for the multiorbital Hubbard model with the Ni bandstructure. The calculated results for the exchange splitting, the magnetic moment, etc., for the ground state show a better agreement with experiments than the LDA results. However, roles of the lattice structure and of the orbitals are not clear in their study. In §5.3 we shall discuss this point with a more refined method, the multiorbital DMFT.

## 5.2 Comparison of the ferromagnetic instability between Ising and SU(2) Hund's couplings

In this section we discuss the difference in the ferromagnetic instability between Ising and SU(2) Hund's couplings [234]. We calculated the ferromagnetic spin susceptibility,

$$\begin{aligned} \chi(\mathbf{0}, 0) &\equiv \sum_{mm'} \chi_{mm'}^{zz}(\mathbf{0}, 0), \\ \chi_{mm'}^{zz}(\mathbf{q}, i\nu) &\equiv \frac{1}{\beta} \int_0^\beta d\tau \int_0^\beta d\tau' \langle T_\tau S_{\mathbf{q}_m}^z(\tau) S_{-\mathbf{q}_{m'}}^z(\tau') \rangle e^{i\nu(\tau-\tau')}, \end{aligned} \quad (5.10)$$

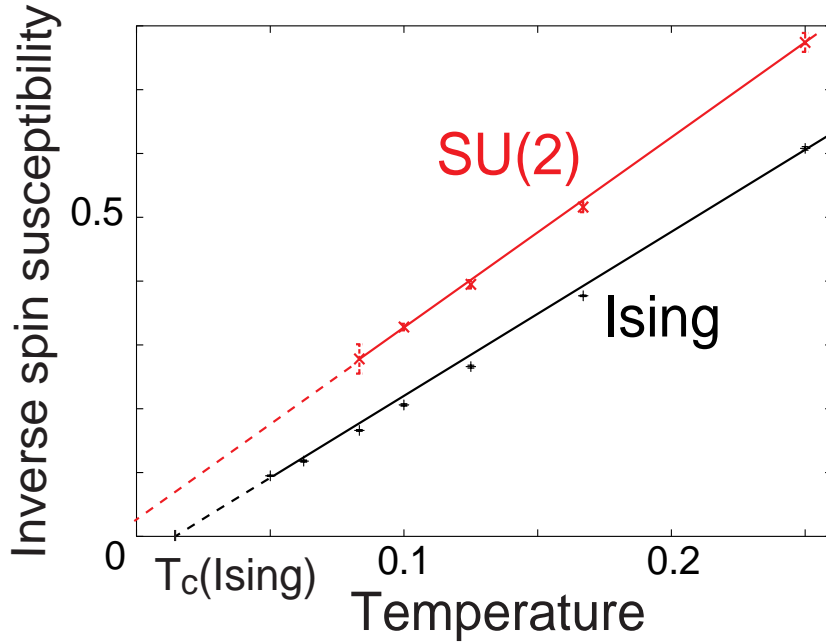


Figure 5.11: Inverse spin susceptibility for the two-orbital Hubbard model with the SU(2)-type Hund and pair-hopping interactions as compared with the Ising-type Hund coupling for  $U' = 2.5$  and  $J = 1$  for the semielliptical density of states of width  $W = 2$ . The solid lines are guide to the eye, and the dashed lines extrapolations. (From Ref. [233].)

in the paramagnetic phase in the two-fold degenerate Hubbard model in the infinite dimensions, where  $\chi_{mm'}^{zz}$  is obtained through the Bethe-Salpeter equation similar to that for the single-orbital case, Eq. (3.16). In Ising case, we exploited the conventional Hirsch-Fye QMC algorithm while in SU(2) case we employed the QMC algorithm developed in §4.5.

Figure 5.11 plots the inverse of the spin susceptibilities against temperature for  $U = 4.5$  and  $J = 1$  at  $n = 1.25$ , where the Bethe lattice with the bandwidth  $W = 2$  has been adopted. Since calculations at temperatures below  $T = 0.05(0.08)$  for Ising[SU(2)] Hund's coupling are rather expensive, we fitted the data above  $T = 0.05(0.08)$  with the Curie-Weiss law,  $\chi^{-1} \propto T - T_c$ , and extrapolated the lines to lower temperatures. We can see that the susceptibility in the Ising case diverges at a finite temperature around 0.02, while that in the SU(2) case remains finite down to  $T = 0$ . This result indicates that the Ising treatment of Hund's exchange grossly overestimates the ferromagnetic instability.

We consider that this result is a general consequence of the different energy of the two-electron states, discussed in §2.2, between the Ising and SU(2) Hund couplings. Namely, in the Ising case the lower energy states consist of the two states,

$$\begin{aligned} c_{im\uparrow}^\dagger c_{im'\uparrow}^\dagger & \text{ with } S^z = 1 \text{ and} \\ c_{im\downarrow}^\dagger c_{im'\downarrow}^\dagger & \text{ with } S^z = -1, \end{aligned}$$

so that spin flips between these two states must go through a higher energy state,

$$\frac{1}{\sqrt{2}}(c_{im\uparrow}^\dagger c_{im'\downarrow}^\dagger + c_{im'\uparrow}^\dagger c_{im\downarrow}^\dagger) \text{ with } S^z = 0.$$

In the SU(2) case, on the other hand, the lower energy states consist of the three states,

$$\begin{aligned} & c_{im\uparrow}^\dagger c_{im'\uparrow}^\dagger \text{ with } S^z = 1, \\ & c_{im\downarrow}^\dagger c_{im'\downarrow}^\dagger \text{ with } S^z = -1, \text{ and} \\ & \frac{1}{\sqrt{2}}(c_{im\uparrow}^\dagger c_{im'\downarrow}^\dagger + c_{im'\uparrow}^\dagger c_{im\downarrow}^\dagger) \text{ with } S^z = 0, \end{aligned}$$

so that these spin states can move to each other without the cost of the energy  $J$ . Then, the local moment is stiffer in the Ising case than in the SU(2) case, which accounts for the stronger tendency to ferromagnetism in the former case.

In fact, preceding DMFT+QMC calculations with Ising Hund's coupling have a tendency to overestimate the Curie temperatures for transition-metal-based materials, compared with the experimental values: For example, the Curie temperatures calculated for manganites [244] and iron [146] are  $\sim 1000\text{K}$  and  $1900\text{K}$ , respectively, which are much higher than the experimental values,  $\sim 300\text{K}$  for manganites and  $1043\text{K}$  for iron. The present comparison indicates that the main reason for overestimating the Curie temperature in such calculations is not only the mean-field nature of the DMFT but also the incorrect symmetry of Hund's coupling.

## 5.3 Effect of Hund's coupling on metallic ferromagnetism

In this section, we address the problem whether we can attribute the appearance of itinerant ferromagnetism in  $d$ -electron systems to a single mechanism; lattice structures *or* the  $d$ -orbital degeneracy. We study ferromagnetism on the fcc lattice in an intermediate-coupling region, keeping Ni in mind, which has been considered a typical example of Kanamori's  $T$ -matrix approximation theory.

### 5.3.1 Consideration from the Kanamori theory — particle-hole channel

As explained in §5.1.2, the Kanamori theory neglects the  $d$ -orbital degeneracy since the contribution of Hund's coupling  $J$  on the stability of ferromagnetism is estimated to be  $J/(1 + U'\chi^{\text{pp}})^2$ , which is much smaller than that of  $U$ , i.e.,  $U/(1 + U\chi^{\text{pp}})$ .

However, this discussion cannot apply beyond the  $T$ -matrix approximation, which takes into account only particle-particle scatterings and is reliable only for low band fillings. For a general band filling contributions from other type of scatterings become im-

portant. In particular, if we take in particle-hole scatterings,<sup>1</sup> the above discussion on the orbital degeneracy breaks down: In a similar way to the  $T$ -matrix theory (see §5.1.2), we can estimate the contribution of the particle-hole (ph) scatterings to the stability of the ferromagnetism as

$$\frac{U}{1 - U\chi^{\text{ph}}} \quad (5.11)$$

for  $U$ , and

$$\frac{J}{(1 - U'\chi^{\text{ph}})^2} \quad (5.12)$$

for  $J$ . Notice that the contribution of  $J$  is amplified by a factor  $(1 - U'\chi^{\text{ph}})^{-2}$ , which is expected to be much larger than that of  $U$ , i.e.,  $(1 - U\chi^{\text{ph}})^{-1}$ . Therefore, the orbital degrees of freedom, especially Hund's exchange coupling, can play a significant role when the particle-hole scatterings are included.

From such a perspective, we investigated the two-orbital Hubbard model with Hund's exchange coupling on an fcc lattice in three dimensions. Comparing the result with that for a multiorbital simple cubic lattice and that for a single-orbital fcc lattice, we discuss whether a single mechanism, *lattice or orbital*, can account for the itinerant ferromagnetism in Ni.

We employed the DMFT combined with the (Trotter + Series-expansion) QMC, evolved in §4.5, as the impurity solver. The algorithm enables us to obtain results holding the spin- and orbital-rotational symmetries. Although the DMFT neglects the momentum dependence of the self-energy, the approximation is expected to be good for the present system since an fcc lattice has a rather large configuration number, that is, twelve nearest neighbors and six next-nearest neighbors. Apart from the neglect of the momentum dependence, the DMFT takes in all types of the Feynman diagrams including the particle-particle and particle-hole scatterings.

### 5.3.2 Result for the simple cubic lattice

Before turning to the results for the fcc lattice, we first show results for the simple cubic lattice. We calculated the spin susceptibility for the double-orbital Hubbard model on the simple cubic lattice with the dispersion,

$$\epsilon(\mathbf{k}) = 2t \sum_{i=1}^3 \cos(k_i). \quad (5.13)$$

Here we take  $t = \frac{1}{\sqrt{6}} \simeq 0.408$ , which gives an effective bandwidth (defined by Eq. (3.10))  $W_{\text{eff}} = 4$ . The initial density of states is plotted in Fig. 5.12.

<sup>1</sup>Liebsch [245] discussed an effect of particle-hole scatterings due to the Coulomb interaction  $U$  in Ni. He incorporated the effect into a renormalization of the hole propagator, and suggested that the particle-hole scatterings should be included to account for experimental photoemission spectra.

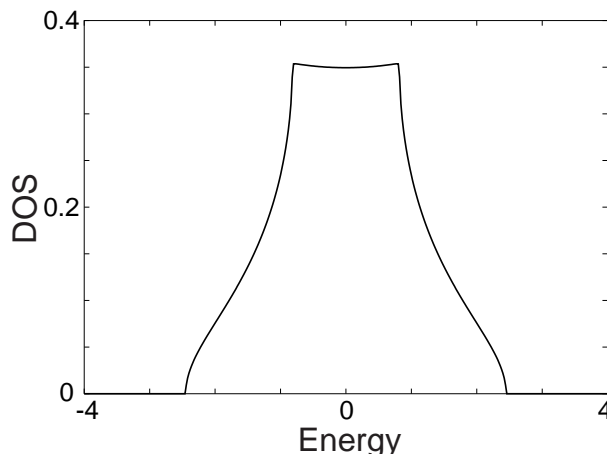


Figure 5.12: The density of states for noninteracting electrons on the three-dimensional simple cubic lattice with  $W_{\text{eff}} = 4$ .

Figure 5.13 is a plot for the inverse of the spin susceptibility (5.10) against temperature for various band fillings. The calculations were done above  $T = 0.1$ , and we fitted the data with the Curie-Weiss law and extrapolated the fitting lines to lower temperatures. We used  $U = 8$ , which is twice larger than  $W_{\text{eff}}$ , and  $J = 1$ , and varies the band filling  $n$  from 0.75 to 1.5. The result implies that there is no ferromagnetic transition for any band filling for these interaction parameters. This result may be compared with the result for the  $d = \infty$  hypercubic lattice [172], where a ferromagnetic ground state is found only for a very large  $U (\gtrsim 4W_{\text{eff}})$  and  $J (\gtrsim W_{\text{eff}})$ . Since the present parameters are large compared with those for transition-metal-based materials ( $U \sim W$ ), it seems impossible to attribute the itinerant ferromagnetism in the materials solely to Hund's exchange coupling.

### 5.3.3 Result for the fcc lattice

Now we show results for the fcc lattice. We have the dispersion,

$$\epsilon(\mathbf{k}) = 4t \sum_{i < j} \cos(k_i) \cos(k_j) + 2t' \sum_{i=1}^3 \cos(2k_i), \quad (5.14)$$

with the hopping parameters  $t = 4t' = \frac{2\sqrt{2}}{3\sqrt{11}} \simeq 0.2843$  ( $t'$ : next-nearest-neighbor hopping), for which the effective bandwidth  $W_{\text{eff}}$  is 4. The density of states for noninteracting electrons is shown in Fig. 5.2, where the bandwidth (the width between the upper and lower band edges) is 4.83. Since the width of Ni- $d$  bands is about 4.5 eV (as we can see from Fig. 5.1), the energy unit roughly corresponds to eV.

#### · Temperature dependence

Figure 5.14 depicts the temperature dependence of the spin susceptibility at  $n = 1.5$ . We selected this filling because the ferromagnetic instability is most enhanced at around

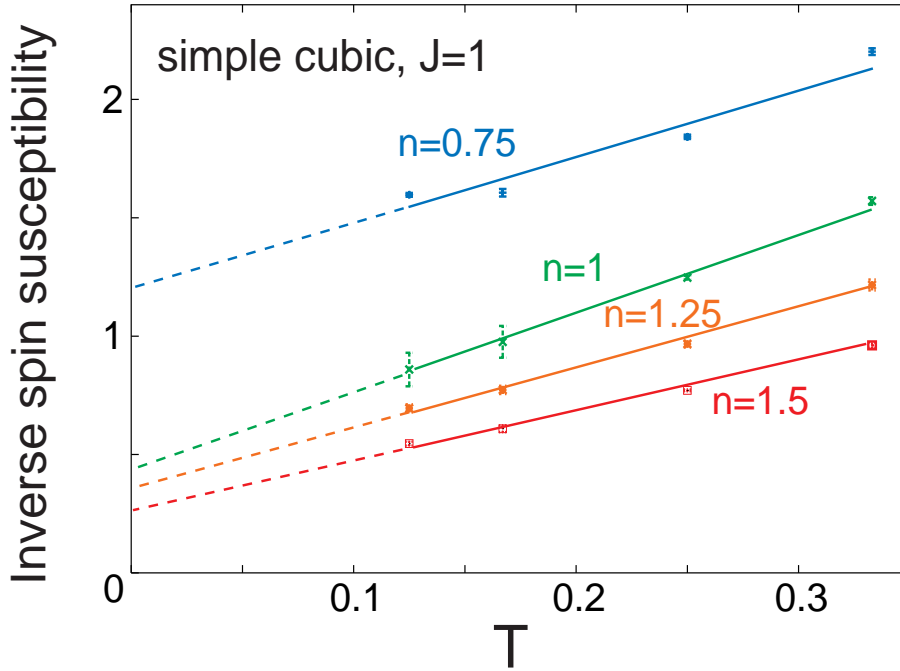


Figure 5.13: The inverse spin susceptibilities plotted against temperature for the two-orbital Hubbard model on the  $d = 3$  simple cubic lattice with  $W_{\text{eff}} = 4$  for various band fillings. Interaction parameters are  $U = 8$ ,  $U' = 6$  and  $J = 1$ .

$n = 1.5$  for  $U = 4$  and  $J = 0.5$ , as we can see from Fig. 5.17 below. The calculations were done above  $T = 0.067$ , and the Curie temperatures were estimated with extrapolations. The intraorbital Coulomb interaction  $U$  is set to be 4, which is a reasonable value for transition metals. We introduce interactions one by one;

- (i) single-orbital case, i.e., multiorbital case with  $U' = J = 0$ ,
- (ii) multiorbital case with  $U' = 4$  and  $J = 0$ ,
- (iii) multiorbital case with  $U' = 3.5$  and  $J = 0.25$ , and
- (iv) multiorbital case with  $U' = 3$  and  $J = 0.5$ .

In (ii)-(iv) we have kept the relation  $U = U' + 2J$ .

In the case (i) the Curie temperature is estimated to be about 0.03. When the interorbital Coulomb interaction  $U'$  is introduced, the ferromagnetic fluctuation is suppressed and the transition disappears [case (ii)]. However, Hund's coupling  $J$  grossly enhances the ferromagnetic tendency and the Curie temperature comes back to finite values [(iii) and (iv)], which are as large as the Curie temperature in the single-orbital case. Moreover, we can see that the Curie temperature significantly depends on  $J$ ;  $T_c \sim 0.015$  for  $J = 0.25$  while  $T_c \sim 0.05$  for  $J = 0.5$ . These results clearly show crucial roles of the interorbital interactions on the ferromagnetism.

Figure 5.15 is a similar plot for a lower band filling  $n = 0.75$ . This filling for the two-orbital model roughly corresponds to the filling of fcc Ni, where almost degenerate five  $d$  bands have two holes per site, so that two  $d$  bands have about 0.8 holes per site. We

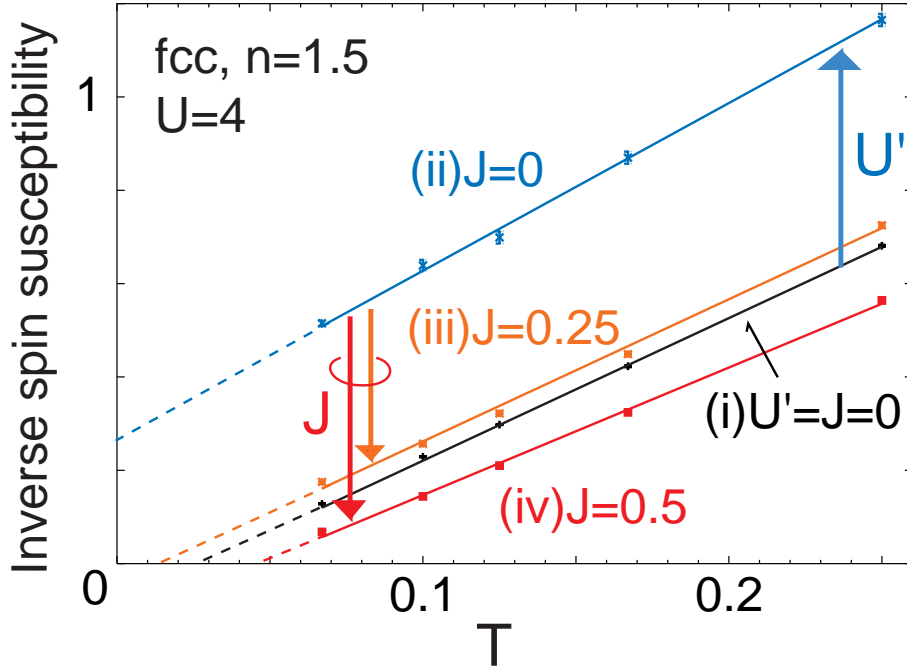


Figure 5.14: The inverse spin susceptibilities plotted against temperature for the two-orbital Hubbard model on the fcc lattice with  $t = 4t'$  and  $W_{\text{eff}} = 4$  for  $U = 4$  at  $n = 1.5$ . We have kept  $U = U' + 2J$  for (ii)-(iv). The solid lines are guide to the eye, and the dashed lines extrapolations.

compare the following four cases;

- (i) single-orbital case, i.e., multiorbital case with  $U' = J = 0$ ,
- (ii) multiorbital case with  $U' = 4$  and  $J = 0$ ,
- (iii) multiorbital case with  $U' = 3$  and  $J = 0.5$ , and
- (iv) multiorbital case with  $U' = 2.5$  and  $J = 0.75$ .

In the case (i) the Curie temperature is around 0.03, and no transition at finite temperatures for the case (ii). The Curie temperatures for  $J = 0.5$  [(iii)] and  $0.75$  [(iv)] are estimated to be about 0.01 and 0.03, respectively.

When we compare the Curie temperature for  $J = 0.5$  at  $n = 0.75$  with that for  $J = 0.5$  at  $n = 1.5$ , we can see that the ferromagnetic instability is smaller in the former case. Since the Fermi energy for  $n = 0.75$  is closer to the peak of the DOS (Fig. 5.2) than that for  $n = 1.5$ , the above filling dependence is totally out of the Stoner picture, so that it also indicates the importance of correlation effects. For  $J = 0.75$  we obtained the Curie temperature as large as that for the single-orbital case [(i)]. This value of  $J$  is still in a range of estimates for transition-metal-based materials.

While the qualitative behavior is similar to that for  $n = 1.5$ , we notice that the  $U'$  and  $J$  dependence of the susceptibility for  $n = 0.75$  is weaker than that for  $n = 1.5$ . It may be due to the low electron density, which makes the interactions, especially the scatterings in the particle-hole channel, less effective. Nevertheless, the interorbital interactions still play

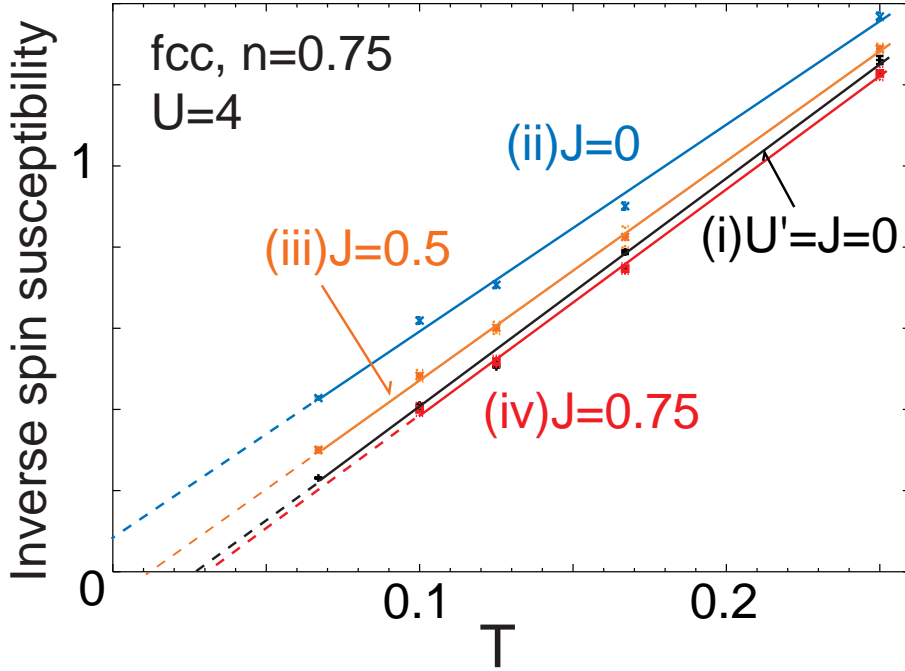


Figure 5.15: The inverse spin susceptibilities plotted against temperature for the two-orbital Hubbard model on the fcc lattice with  $t = 4t'$  and  $W_{\text{eff}} = 4$  at  $n = 0.75$ . The solid lines are guide to the eye, and the dashed lines extrapolations.

important roles, in contrast to the Kanamori theory, where the orbital degrees of freedom are neglected on the basis of the  $T$ -matrix approximation. The present result indicates that even for fillings as low as that for Ni (0.4 holes per band), the contribution from particle-hole scatterings is significant. Therefore we need strong-coupling theory beyond the  $T$ -matrix approximation, which simultaneously means that the  $d$ -orbital degeneracy must be taken into account.

· *Local spin moment*

Since Hund's exchange coupling aligns electron spins on the same site, one might think that the enhancement of the spin susceptibility by  $J$  may result from the formation of a local spin moment.

Figure 5.16 is the  $z$  component of the local spin moment,

$$\langle (\hat{S}^z)^2 \rangle = \frac{1}{4} \left\langle \left[ \sum_m (n_{m\uparrow} - n_{m\downarrow}) \right]^2 \right\rangle, \quad (5.15)$$

calculated for (a)  $n = 1.5$  at  $T = 0.067$  and for (b)  $n = 0.75$  at  $T = 0.1$ , corresponding to Fig. 5.14 and 5.15, respectively. For both of the fillings, temperature dependence of the local moments is weak for  $0.067 < T < 0.25$ . For  $n = 1.5$  the local moment increases as  $J$  is increased with the fixed relation  $U' = U - 2J$  while the moment is almost constant for  $0 < J < 0.75$  at  $n = 0.75$ .

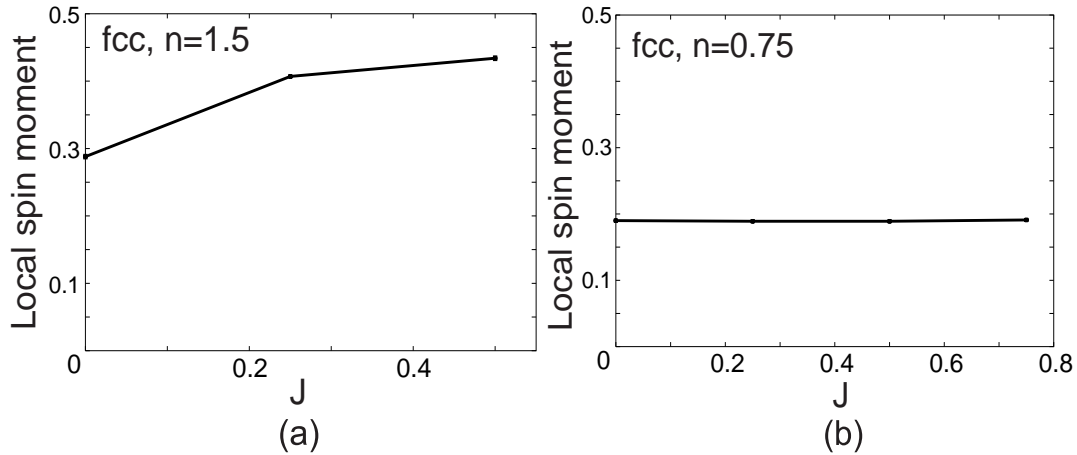


Figure 5.16: The local spin moment calculated for the two-orbital Hubbard model on the fcc lattice at (a)  $n = 1.5$  and (b)  $n = 0.75$ .  $U = 4$  and the relation  $U' = U - 2J$  are fixed.

These results suggest that the formation of a local spin moment is only a minor factor in the enhancement of the spin susceptibility, especially for low band fillings, and that  $J$  enhances *nonlocal* ferromagnetic correlations via electron transfers.

· *Filling dependence*

Figure 5.17 displays the filling and  $U$  dependence of the spin susceptibility at  $T = 0.1$ . We fixed  $J = 0.5$  and varied  $U$  from 2 to 5, keeping the relation  $U' = U - 2J$ . We can see that the susceptibilities take the largest value at around  $n = 1.2-1.5$ , and the peak position shifts to higher fillings as  $U$  is increased. This filling dependence is considerably different from that with single-orbital weak-coupling theories, such as the  $T$ -matrix [30] and the FLEX [143] approximations, where the ferromagnetic instability is most dominant for lower densities ( $n \sim 0.4$  for two orbits). The present behavior against filling is, however, similar to that obtained in other strong-coupling DMFT studies on the single-orbital fcc lattice [142] and on the two-orbital Bethe lattice with Ising Hund's coupling [164].

### 5.3.4 Discussion

We saw in §5.3.2 that no ferromagnetism occurs in the simple cubic lattice for  $U \sim 2W_{\text{eff}}$  and  $J \sim W_{\text{eff}}/4$ , which are considered substantially larger than the realistic values of  $U$  and  $J$  for transition metals and transition-metal oxides. On the other hand, we saw in §5.3.3 that for the fcc lattice, where ferromagnetism exists already for the single-orbital model for an intermediate coupling ( $U \sim W$ ), the Curie temperature significantly changes with the interorbital interactions: The interorbital Coulomb interaction  $U'$  suppresses ferromagnetic fluctuations while Hund's coupling and the pair-hopping interaction considerably enhance the fluctuations. Thus the Curie temperature is determined by the balance of these interactions. Therefore, we need to consider both lattice structures and orbital degrees of freedom to understand the appearance of itinerant ferromagnetism in transition-metal-based materials.

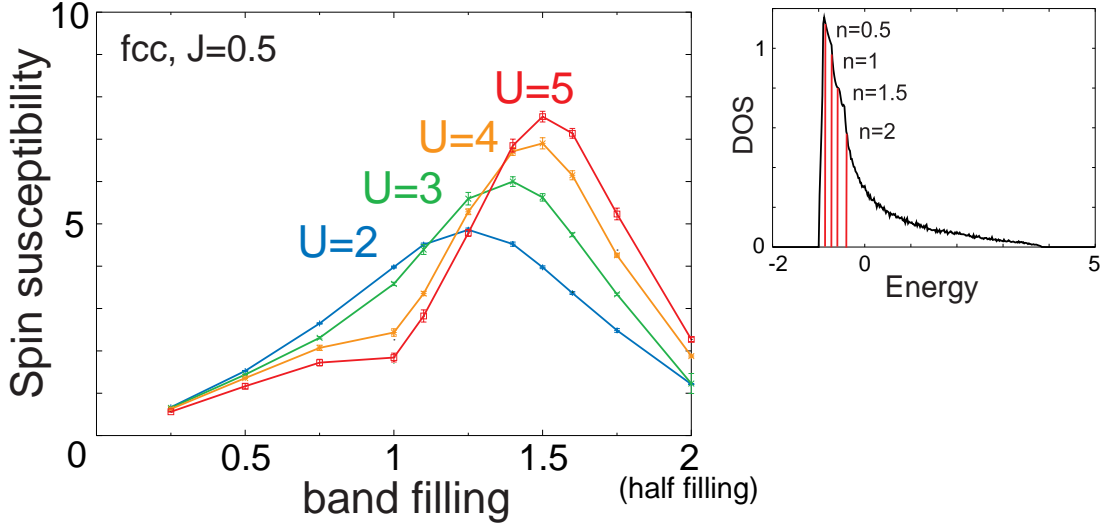


Figure 5.17: Left: Spin susceptibility plotted against the band filling for the two-orbital Hubbard model on the fcc lattice at  $T = 0.1$  for various values of  $U$ , where  $J = 0.5$  and the relation  $U' = U - 2J$  are fixed. Right: The density of states for noninteracting electrons on the fcc lattice (the same as Fig. 5.2).

Here we consider why  $U'(J)$  suppresses(enhances) the magnetic susceptibility. We discuss the behavior from the strong-coupling limit and from the weak-coupling regime.

· *Reduction of spin susceptibility with  $U'$*

At first glance, it may seem strange that the interorbital Coulomb interaction,  $U'n_1n_2$  ( $n_m \equiv \sum_{\sigma} n_{m\sigma}$ ), affects the spin polarization (Fig. 5.14, 5.15), since the interaction is spin independent. To understand the effect of  $U'$  qualitatively, it is helpful to consider on-site two-electron states in the strong-coupling (or atomic) limit, where the Hamiltonian is given only by the on-site interactions,

$$\begin{aligned} \hat{H}_{\text{atom}} &= U \sum_m n_{m\uparrow} n_{m\downarrow} + \sum_{\sigma} [U' n_{1\sigma} n_{2,-\sigma} + (U' - J) n_{1\sigma} n_{2\sigma}] \\ &+ J(c_{1\uparrow}^{\dagger} c_{2\downarrow}^{\dagger} c_{1\downarrow} c_{2\uparrow} + c_{1\uparrow}^{\dagger} c_{1\downarrow}^{\dagger} c_{2\downarrow} c_{2\uparrow} + \text{H.c.}). \end{aligned} \quad (5.16)$$

The two-electron eigenstates for the Hamiltonian are classified by the symmetries with respect to spin and orbital as

Notation	Spin	Orbital	Expression
$1S^0$	singlet	symmetric	$\frac{1}{\sqrt{2}}(c_{1\uparrow}^{\dagger} c_{2\downarrow}^{\dagger} + c_{2\uparrow}^{\dagger} c_{1\downarrow}^{\dagger}) 0\rangle$
$1S^{\pm}$	singlet	symmetric	$\frac{1}{\sqrt{2}}(c_{1\uparrow}^{\dagger} c_{1\downarrow}^{\dagger} \pm c_{2\uparrow}^{\dagger} c_{2\downarrow}^{\dagger}) 0\rangle$
$3^0 A$	triplet	antisymmetric	$\frac{1}{\sqrt{2}}(c_{1\uparrow}^{\dagger} c_{2\downarrow}^{\dagger} - c_{2\uparrow}^{\dagger} c_{1\downarrow}^{\dagger}) 0\rangle$
$3^{\sigma} A$	triplet	antisymmetric	$c_{1\sigma}^{\dagger} c_{2\sigma}^{\dagger}  0\rangle.$

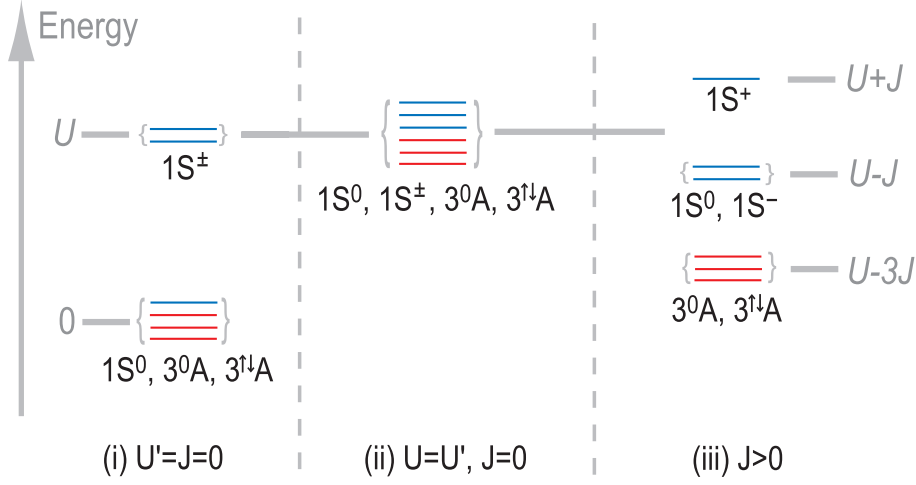


Figure 5.18: Level scheme for the strong coupling limit. (i) Single-orbital case i.e.,  $U > 0$  and  $U' = J = 0$ . (ii) Multiorbital case with  $U = U' > 0$  and  $J = 0$ . (iii) Multiorbital case with  $U' = U - 2J$  and  $J > 0$ . Blue (red) lines denote spin-singlet (triplet) states.

The eigenenergies for the six states (Fig. 5.18) are

$$\begin{aligned}
 E_{1S^+} &= U + J, \\
 E_{1S^0} &= U' + J, \\
 E_{1S^-} &= U - J, \\
 E_{3^0A} &= E_{3^{\uparrow\downarrow}A} = U' - J.
 \end{aligned} \tag{5.17}$$

While the spin-triplet states have the same energy  $U' - J$ , the orbital-symmetric states split into three energies,  $U + J$ ,  $U' + J$  and  $U - J$ , because there is no  $SU(2)$  symmetry for orbitals. Then, the ground state for  $U > 0$  and  $U' = J = 0$  [case (i)] is a superposition of the four states,  $1S^0$ ,  $3^0A$  and  $3^{\uparrow\downarrow}A$ , while the ground state for  $U = U' > 0$  and  $J = 0$  [case (ii)] is a superposition of the six states,  $1S^0$ ,  $1S^\pm$ ,  $3^0A$  and  $3^{\uparrow\downarrow}A$ . Counting the number of spin-singlet states, we find that there are three times larger number of spin singlets in the case (ii) than in the case (i). These spin-singlet states will reduce the ferromagnetic tendency, which may account for the reduction of the susceptibility by  $U'$  in Fig. 5.14 and 5.15.

#### · Enhancement of spin susceptibility with $J$

Next we discuss the enhancement of the spin susceptibility with  $J$ . From the above discussion in the strong-coupling limit, we can see that the introduction of  $J$ , keeping the relation  $U = U' + 2J$ , brings down the energy of the spin-triplet states. This may be one reason for the increase of the susceptibility. Indeed, the local moment for  $n = 1.5$  [Fig. 5.16(a)] increases as  $J$  is increased.

However, for  $n = 0.75$  the local moment is almost constant while the Curie temperature noticeably increases with  $J$ . This behavior may be understood in the weak-coupling

regime. As we discussed in §5.3.1, it is expected in the weak-coupling region that  $J$  considerably reduces the energy of spin triplets through electron scatterings in the particle-hole channel. As for the filling dependence (Fig. 5.17), the susceptibility for  $J = 0.5$  increases as  $n$  is increased from a low density to around  $n = 1.5$ , which should be due to the increase of the contribution from particle-hole scatterings. For  $n \gtrsim 1.5$ , the susceptibility decreases as  $n$  approaches to the half filling ( $n = 2$ ), which will result from increasing antiferromagnetic correlations.

## 5.4 Summary

We have discussed an important problem of, whether a single mechanism, lattice structure *or* Hund's exchange, can account for the itinerant ferromagnetism in  $d$ -electron systems, such as transition metals and transition-metal oxides. We modelled the system as the multi-orbital Hubbard model (2.9), and calculated the spin susceptibility in the paramagnetic phase, using the DMFT combined with the (Trotter + Series-expansion) QMC method, which preserves the spin and orbital rotational symmetries.

First we show that the conventional Ising treatment of Hund's coupling grossly overestimates the ferromagnetic instability, so that the preservation of the spin and orbital rotational symmetries is crucial for discussing ferromagnetism.

Then we calculated the magnetic susceptibility for the simple cubic and fcc lattices in three dimensions. The result shows that no ferromagnetism arises in the simple cubic lattice for an intermediate-coupling region ( $U \sim W$ ). On the other hand, in the fcc lattice the Curie temperature is already estimated to be finite in the single-orbital model, and  $T_c$  strongly depends on the values of  $U'$  and  $J$ :  $U'$  remarkably suppresses the spin susceptibility, which can be understood from the strong-coupling limit as the reduction of energy splitting in the three spin-singlet states. By contrast,  $J$  considerably enhances the ferromagnetic instability, which should be due to a local and a nonlocal alignments of spins, especially contributed from the electron scatterings in the *particle-hole channel*. Therefore, the Curie temperature on the fcc lattice highly depends on the balance between the interactions.

We can thus conclude from the present calculations that both lattice structure *and* the  $d$ -orbital degrees of freedom are necessary for understanding the itinerant ferromagnetism in transition metals and their compounds.

# Chapter 6

## Application to a three-orbital system

To demonstrate the applicability of our QMC method (§4.5), we have performed a three-orbital calculation in the framework of the LDA+DMFT for a typical three-orbital system,  $\text{Sr}_2\text{RuO}_4$ .

In §6.1.1 we elaborate our motivation and why we chose this material for a test of our algorithm. The importance of correlation effects in this material has been suggested by many electronic structure calculations, as reviewed in §6.1.2. The detailed crystal structure and the bandstructure are explained in §6.2 (although the material and related materials have already been mentioned in §1.3.3). The model for the DMFT calculation is constructed in §6.3. We show in §6.4.1 results for the quasiparticle spectra of this material, and compare the spectra between Ising-type and  $\text{SU}(2)$ -symmetric Hund's couplings. Result for the quasiparticle mass is shown in §6.4.2. §6.5 is devoted to discussions of the results. Summary and conclusions in this chapter are given in §6.6.

### 6.1 Introduction

#### 6.1.1 Purpose

The main purpose in this chapter is to demonstrate the applicability of the QMC algorithm developed in §4.5 to three-orbital systems.

As explained in §4.2 and §4.5, the conventional Hirsch-Fye QMC method has a difficulty in treating the Hund-exchange and pair-hopping interactions. The difficulty becomes more conspicuous for more than two orbitals, and it seems almost beyond hope to formulate the Hirsch-Fye algorithm in a spin- $\text{SU}(2)$ -symmetric way for a practical use for three or more orbitals (see §4.2). Therefore, the Ising treatment of Hund's coupling has been invoked in many DMFT studies including LDA+DMFT (see §3.4). In §5.2 we saw, however, that the Ising treatment causes a considerable quantitative error (overestimation) in the spin susceptibility.

Our formulation of the QMC algorithm (§4.5) based on a series expansion makes it possible to address three or more orbitals with preserved spin and orbital rotational symmetries. Then our purposes are

- (i) to demonstrate the QMC calculation on a three-orbital system,
  - (ii) to show the applicability of the present method for real materials,
  - (iii) to compare the quasiparticle spectra with Ising and SU(2) Hund's couplings,
- and
- (iv) to give a guideline for Ising-type LDA+DMFT studies to estimate how spectra change with the recovery of the spin and orbital rotational symmetries.

Our QMC calculation is the first one for a three-orbital system with spin and orbital rotational invariance, as well as the first one for an LDA+DMFT calculation with full account of the multiorbital interactions in the Hamiltonian (2.9).

For the above purposes we selected  $\text{Sr}_2\text{RuO}_4$  [78] as a test. As was introduced in §1.3.3, this material is a prototype of three-orbital systems. The crystal has a single-layered perovskite structure without any rotational distortion of  $\text{RuO}_6$  octahedra (the detailed structure is explained in §6.2). The simple structure makes it easy to deal with the present method. Moreover, a partially extended nature of the Ru-4*d* orbitals allows for a relatively small interaction parameter ( $U/W \sim 0.4-1$ ), compared with those for the 3*d* transition-metal oxides ( $U/W \gtrsim 1$ ). This is advantageous for the computational time.

We also compare the obtained results with experimental ones. Since we treat  $U$  and  $J$  as parameters, we cannot discuss quantitative agreements with experimental results. Nevertheless, we could make qualitative arguments for correlation effects in  $\text{Sr}_2\text{RuO}_4$ , suggested in many experimental and theoretical studies.

## 6.1.2 Correlation effects in $\text{Sr}_2\text{RuO}_4$

Since the discovery of the superconductivity [2] and the subsequent experiments identifying its pairing symmetry as spin triplet [54, 246],  $\text{Sr}_2\text{RuO}_4$  has engaged considerable attentions.

The quasiparticle spectra in the normal state of the material have a special importance for understanding the occurrence of the superconductivity, since the transition temperature, in general, is determined by the density of states near the Fermi level. While the Fermi surface calculated with the LDA [247, 248, 249] is in good agreement with the angle-resolved photoemission spectroscopy (ARPES) [250]-[253] and de Haas-van Alphen (dHvA) experiments [78, 254], which detects energy levels in solids from a quantum oscillation of magnetization in a magnetic field, the LDA cannot reproduce the peak structure as observed in photoemission [195], [250]-[253], [255]-[259] and X-ray absorption spectra [257, 258]. In particular, the width, as well as the height, of the quasiparticle peak at around  $E_F$  is 2-3 times overestimated in the LDA. Also, the LDA cannot reproduce a satellite peak in the photoemission spectra at around  $-3 \sim -2.5$  eV (see Fig. 6.2 below), which is interpreted as a precursor of the lower Hubbard band. Moreover, the LDA gives 3-4 times smaller effective mass for quasiparticles than that evaluated from the dHvA [254], ARPES [250], optical conductivity [260] and specific heat measurements [261]. These failures in the LDA calculations suggest the importance of correlation effects in this material.

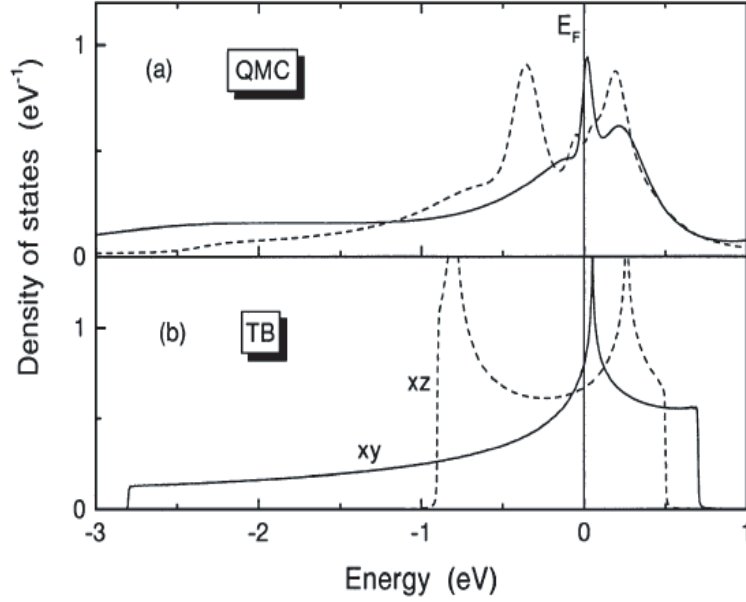


Figure 6.1: The quasiparticle spectra for Ru- $t_{2g}$  orbitals in  $\text{Sr}_2\text{RuO}_4$  calculated by Liebsch and Lichtenstein [212]. (a) The LDA+DMFT result for  $U = 1.2$  eV,  $U' = 0.8$  eV and Ising-type  $J = 0.2$  eV. (b) A tight-binding-model fitted DOS of the LDA result. (From Ref. [212].)

Pérez-Navarro *et al.* [262] investigated correlation effects on the density of states (DOS), particularly at  $E_F$ , comparing the LDA, the LDA+ $U$  and a result with a self-energy correction at RPA level. They incorporated a self-energy correction by fitting peaks of the LDA DOS for  $d$  electrons with a double-Lorentzian function. They observed that while both of the LDA and LDA+ $U$  fail to explain the experimentally obtained small DOS at  $E_F$ , the self-energy correction significantly reduces the DOS at  $E_F$ . Tran *et al.* [259] implemented a realistic Hartree-Fock calculation for  $\text{Sr}_2\text{RuO}_4$ , and compared the result with their X-ray photoemission data. The Hartree-Fock calculation fails to reproduce the experimental peak positions as well as overestimates the quasiparticle bandwidth. Then they examined a self-energy correction, to a second order in the interactions, to the Hartree-Fock solution. They found that the self-energy correction reduces the quasiparticle bandwidth, which is an improvement from the Hartree-Fock solution, while the peak positions and intensities were not remedied so much. This result implies that contributions from higher-order terms in the self-energy are crucial for  $\text{Sr}_2\text{RuO}_4$ .

Liebsch and Lichtenstein [212] applied the LDA+DMFT method to the material. Although  $\text{Sr}_2\text{RuO}_4$  is a quasi-two-dimensional system, the DMFT would give the momentum-independent part of the self-energy in a first approximation. Liebsch and Lichtenstein constructed a simple tight-binding model reproducing the LDA bandstructure and solved the model with the DMFT+(Hirsch-Fye)QMC, where they used  $U = 1.2$  eV,  $U' = 0.8$  eV and Ising-type  $J = 0.2$  eV. They found a pronounced narrowing of the  $d_{xz,yz}$  bandwidths and accompanying electron transfers from the  $d_{xz,yz}$  bands to the  $d_{xy}$  band, which shifts the

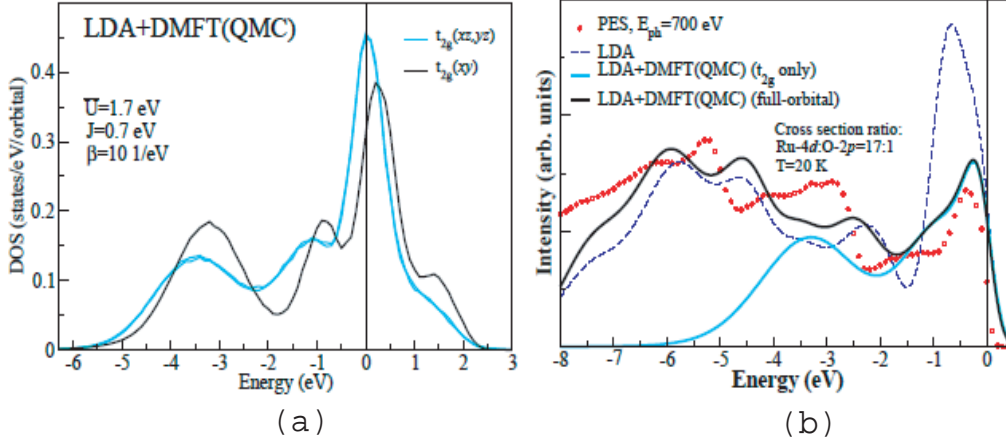


Figure 6.2: The quasiparticle spectra for Ru- $t_{2g}$  orbitals in  $\text{Sr}_2\text{RuO}_4$ , calculated theoretically and measured experimentally by Pchelkina *et al.* [195] (a) The  $t_{2g}$  DOS obtained with the LDA+DMFT method for  $U = 3.1$  eV,  $U' = 1.7$  eV and Ising-type  $J = 0.7$  eV. (b) The comparison of the LDA+DMFT result [(a)] with the X-ray photoemission and the LDA result. Light blue line is the spectral function for Ru- $t_{2g}$  orbitals only, while black solid line includes contributions from all orbitals. Red circles are the experimental data. The theoretical spectra were multiplied with the Fermi function at  $T = 20$  K and were broadened to account for the experimental resolution. (From Ref. [195].)

van Hove singularity of  $d_{xy}$  closer to  $E_F$  (Fig. 6.1). Recently Pchelkina *et al.* [195] proposed much larger interaction parameters ( $U = 3.1$  eV,  $U' = 1.7$  eV, Ising-type  $J = 0.7$  eV), based on a constrained LDA calculation. They implemented a self-consistent LDA+DMFT calculation [194], and compare the results with photoemission experiments. They found a lower Hubbard peak at around  $-3$  eV, consistent with the photoemission data (Fig. 6.2). The calculated effective mass enhancements are 2.62 for the  $d_{xy}$  orbital, and 2.28 for the  $d_{xz,yz}$  orbitals, which are similar to, but somewhat smaller than, the experimental estimates [250, 254, 260, 261].

Given these studies, we now implement a calculation preserving the spin and orbital rotational symmetries, contrary to the preceding LDA+DMFT calculations. We see how correlation effects change the spectra, by varying the strength of the interactions, and discuss the different behavior of the spectra between the Ising and SU(2) Hund couplings.

## 6.2 Crystal structure and bandstructure of $\text{Sr}_2\text{RuO}_4$

$\text{Sr}_2\text{RuO}_4$  has the  $\text{K}_2\text{NiF}_4$  crystal structure with the tetragonal symmetry [Fig. 6.3(a)]. A ruthenium atom is surrounded by six oxygen atoms, which compose an octahedron. The octahedra form two-dimensional arrays separated by strontium layers, and are elongated along  $c$  axis: The distance between a Ru atom and a neighboring O atom in the  $c$  direction is  $2.06\text{\AA}$ , which is larger than the sum of the ionic radii of  $\text{Ru}^{4+}$  and  $\text{O}^{2-}$ , while the distance

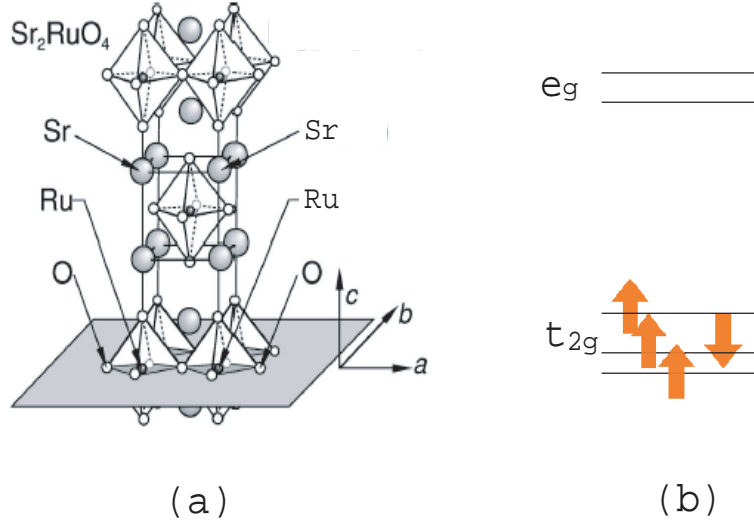


Figure 6.3: (a) The crystal structure of  $\text{Sr}_2\text{RuO}_4$  (from Ref. [78]). (b) Level scheme for  $d$  electrons.

between a Ru and O atoms in the  $ab$  plane is  $1.93\text{\AA}$  [263], which is smaller than the sum of the ionic radii. This suggests that the hybridization between Ru- $d$  and O- $p$  orbitals is strong in the  $a$  and  $b$  directions while it is weak in the  $c$  direction. Thus the system has a quasi-two-dimensional character.

A  $\text{Ru}^{4+}$  ion has four  $d$  electrons. Since the crystal field of the octahedra lifts the Ru- $e_g$  orbitals about 4 eV higher than the Ru- $t_{2g}$  orbitals, these four electrons occupy the  $t_{2g}$  orbitals and the  $e_g$  orbitals are nearly empty [Fig. 6.3(b)].

Figure 6.4 is the LDA bandstructure calculated by Singh [248]. The three curves crossing the Fermi energy ( $E = 0$ ) are the  $t_{2g}$  bands. One of the three bands has a bandwidth almost twice larger than the others. The wider band corresponds to the  $d_{xy}$  orbital extending in the  $ab$  plane and hybridizing with O- $2p$  orbits in the  $a$  and  $b$  direction, while the narrower bands correspond to the  $d_{yz}$  and  $d_{xz}$  orbitals extending perpendicular to the  $ab$  plane and hybridizing with O- $2p$  orbits in the  $c$  direction and in one of  $a$  and  $b$  directions. Since the Ru-O hybridization along the  $c$  axis is very small, the  $d_{xy}$  band has almost twice wider than the  $d_{yz}$  and  $d_{xz}$  bands.

The Fermi surface obtained with the LDA calculation is consistent with the experimental observations, such as ARPES [250]-[253] and dHvA measurements [78, 254] (Fig. 6.5). The Fermi surface consists of three cylindrical sheets: one hole-like sheet ( $\alpha$ ) centered at the  $X = (\pi, \pi)$  point and two electron-like sheets ( $\beta$  and  $\gamma$ ) centered at the  $\Gamma = (0, 0)$  point, and they have almost no dispersion along  $c$  axis.  $\gamma$  sheet reflects the two-dimensional character of  $d_{xy}$  orbital while  $\alpha$  and  $\beta$  sheets derive from  $d_{xz}$  and  $d_{yz}$  orbitals, which have a one-dimensional character in a  $\text{RuO}_2$  layer, after taking account of a weak hybridization between them.

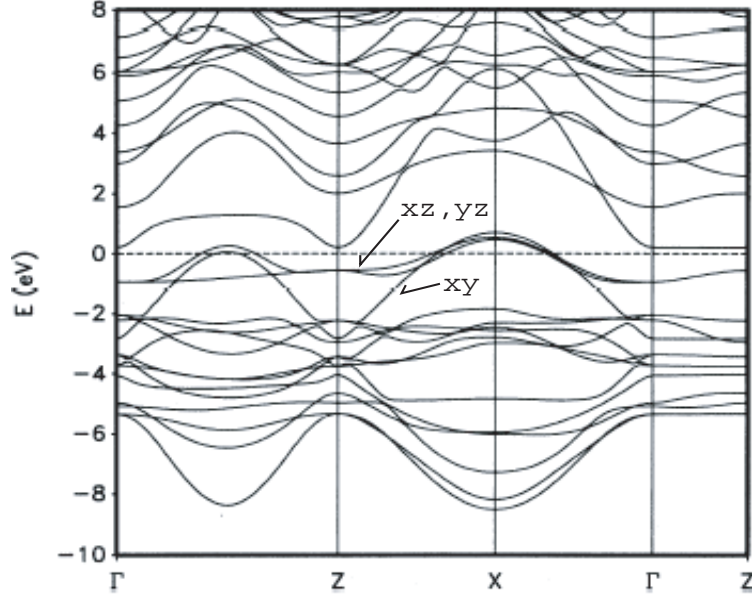


Figure 6.4: The LDA bandstructure of  $\text{Sr}_2\text{RuO}_4$  calculated by Singh [248].

### 6.3 Modeling

The bandstructure of  $\text{Sr}_2\text{RuO}_4$  near the Fermi level can be well reproduced by a simple tight-binding model focusing only on the Ru- $t_{2g}$  bands [212, 247, 248].

We follow the model construction by Liebsch and Lichtenstein [212]. They considered a two-dimensional square lattice, where the lattice points represent Ru sites, and a weak hybridization between  $\text{RuO}_2$  layers is neglected. Since the original  $\text{RuO}_6$  octahedra have no rotational distortion, hybridizations between  $d_{xy}$  and  $d_{xz,yz}$  orbitals are prohibited by the difference in the parity under the mirror operation  $z \rightarrow -z$ , i.e.,  $d_{xy}$  is even while  $d_{xz,yz}$  is odd. Although there is a weak hybridization between  $d_{xz}$  and  $d_{yz}$  orbitals through next-nearest-neighbor hoppings, here we neglect it according to Liebsch and Lichtenstein's formulation.

Then the dispersion on the square lattice with the hoppings up to next-nearest neighbors is

$$\epsilon(\mathbf{k}) = -\epsilon_0 - 2t_x \cos(k_x) - 2t_y \cos(k_y) + 4t' \cos(k_x) \cos(k_y). \quad (6.1)$$

Here we define the (orbitally-dependent) level shift  $\epsilon_0$ , the nearest-neighbor hoppings  $t_x, t_y$ , and the next nearest-neighbor hopping  $t'$ . Liebsch and Lichtenstein determined  $\epsilon_0, t_x, t_y$  and  $t'$  by fitting them to the LDA bandstructure Fig. 6.4, and obtained

$$(\epsilon_0, t_x, t_y, t') = (0.50, 0.44, 0.44, -0.14) \text{ eV} \quad (6.2)$$

for the  $d_{xy}$  band, and

$$(\epsilon_0, t_x, t_y, t') = (0.24, 0.31, 0.045, 0.01), (0.24, 0.045, 0.31, 0.01) \text{ eV} \quad (6.3)$$

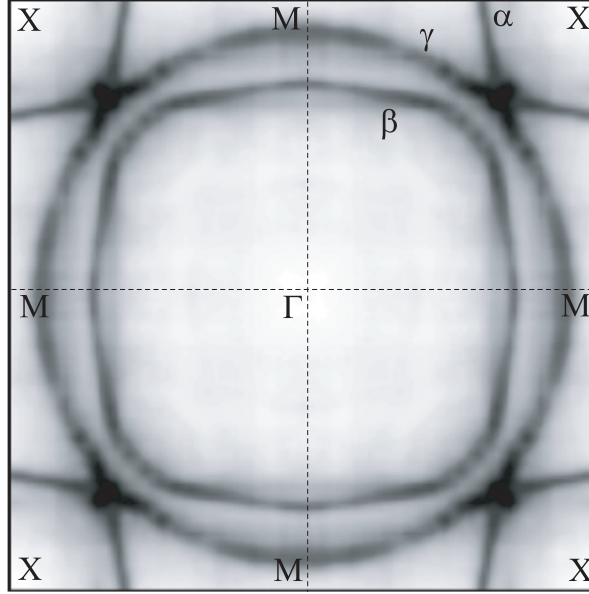


Figure 6.5: The two-dimensional Fermi surfaces of  $\text{Sr}_2\text{RuO}_4$  obtained with ARPES [252] (from Ref. [78]).

for the  $d_{xz,yz}$  bands, respectively. These parameters produce the density of states shown in Fig. 6.1(b), which has the  $d_{xy}$  band edges at  $-2.8$  eV and  $0.7$  eV, the  $d_{xz,yz}$  band edges at  $-0.9$  eV and  $0.5$  eV, and van Hove singularities at  $0.05$  eV for  $d_{xy}$  and at  $-0.80$  eV and  $0.26$  eV for  $d_{xz,yz}$ , in agreement with the LDA bandstructure [248]. We adopt this density of states as an initial input for the following DMFT calculations.

Next we consider the interaction part of the model. We employ the on-site interaction in the form  $H_{\text{int}}$  in Eq. (2.9). The problem is how to determine the parameters  $U$  and  $J$  (or  $U' = U - 2J$ ) because there is a large ambiguity in both theoretical and experimental estimates: Liebsch and Lichtenstein [212] employed  $U = 1.2\text{-}1.5$  eV and  $J = 0.2\text{-}0.4$  eV, based on the observation of a valence band satellite in the photoemission experiment [255], which leads to  $U \sim 1.5$  eV. Pérez-Navarro *et al.* [262] used  $U = 2.4$  eV (without  $J$  terms) on the ground of another photoemission experiments [256, 264], and Tran *et al.* [259] used a similar value  $U = 2.5$  eV with  $J = 0.5$  eV. Meanwhile, Pchelkina *et al.* [195] theoretically calculated these parameters by means of the constrained LDA, and obtained  $U = 3.1$  eV and  $J = 0.7$  eV. However, such theoretical calculations for  $U$  and  $J$  also have some uncertainties: There is an ambiguity in the first-principles definition of the basis of the tight-binding model (or definition of the Wannier functions), and in the treatment of the screening effect for electron-electron interactions.

So we implemented the LDA+DMFT calculation, changing values of  $(U, J)$  from  $(1.2, 0.2)$  eV to  $(2.4, 0.4)$  eV. Although a severe negative sign problem in the QMC algorithm prevents studies for stronger couplings, we can clearly see a behavior different from the weak-coupling region in the quasiparticle spectra already for  $(U, J) = (2.4, 0.4)$  eV. We compare the SU(2) result to that with Ising Hund's coupling and discuss difference be-

tween them.

## 6.4 Result

### 6.4.1 Quasiparticle spectra — Comparison between Ising and SU(2) cases

We have obtained the density of states for Sr<sub>2</sub>RuO<sub>4</sub> with the LDA+DMFT calculation preserving the spin and orbital rotational symmetries.

First we implemented the DMFT+(Trotter + Series-expansion)QMC calculation for the three-orbital Hubbard model (2.9) with the dispersion (6.1) and the parameters (6.2) and (6.3), changing  $(U, J)$  from (1.2, 0.2) eV to (2.4, 0.4) eV with a fixed ratio  $U = 1.5U' = 6J$ , which is a reasonable parameterization for real materials and satisfy  $U = U' + 2J$ . Throughout the calculations we used  $\beta = 10 \text{ eV}^{-1}$  and  $L = 40$ , which are the same as those employed in Ref. [195], but smaller than those in Ref. [212] (where  $\beta \sim 70 \text{ eV}^{-1}$  and  $L = 128$  were used), and took  $1.28 \times 10^8$  samples in one QMC calculation for the most computationally expensive case,  $(U, J) = (2.4, 0.4) \text{ eV}$ .

From the QMC calculation we obtained Green's function,  $G_a(\tau)$  ( $a = xy, xz, yz$ ), on the imaginary-time axis. Then we calculated the spectral function  $A_a(\omega)$  for real frequencies from the relation,

$$G_a(\tau) = - \int_{-\infty}^{\infty} d\omega \frac{e^{-\tau\omega}}{1 + e^{-\beta\omega}} A_a(\omega) \quad \text{for } 0 < \tau < \beta. \quad (6.4)$$

This integral equation is, however, an ill-defined inverse problem because a small deviation in  $G_a(\tau)$  significantly affects the solution  $A_a(\omega)$ . Indeed, a calculated  $G_a(\tau)$  contains some error bars coming from the stochastic process in the QMC simulation. Therefore, in order to solve the inverse problem (6.4), we applied the maximum entropy method [265], which provides a reasonable solution by use of some prior information of the solution  $A_a(\omega)$ , such as  $A_a(\omega) \geq 0$  and  $\int_{-\infty}^{\infty} A_a(\omega) d\omega = 1$ .

The obtained  $A_a(\omega)$ , the density of quasiparticle states, is shown in Fig. 6.6, where the DOS with Ising Hund's coupling is also plotted for comparison. For weak couplings,  $(U, J) = (1.2, 0.2) \text{ eV}$ , the spectra with SU(2) Hund's coupling have a similar structure to those obtained with Ising Hund's coupling, which agree well with Liebsch and Lichtenstein's result [212]. We can see that the van Hove singularity for the  $xy$  orbital remains just above  $E_F$  while those of the  $xz, yz$  orbitals shift closer to  $E_F$  than those in the LDA spectra. We can also see a precursor of the lower and upper Hubbard bands respectively at around  $-1.2 \text{ eV}$  and  $1.8 \text{ eV}$  for  $xz, yz$ , and at around  $-1.8 \text{ eV}$  for  $xy$ . The upper Hubbard band for  $xy$  is not visible in this resolution, which may be due to the wider width of the  $xy$  band.

As the interaction increases, the van Hove peaks become broader both in the Ising and SU(2) cases, and the initial two-peak structure in the  $xz$  and  $yz$  DOS almost disappears for  $(U, J) = (2.1, 0.35) \text{ eV}$ . However, for an increased  $(U, J) = (2.4, 0.4) \text{ eV}$ , a remarkable

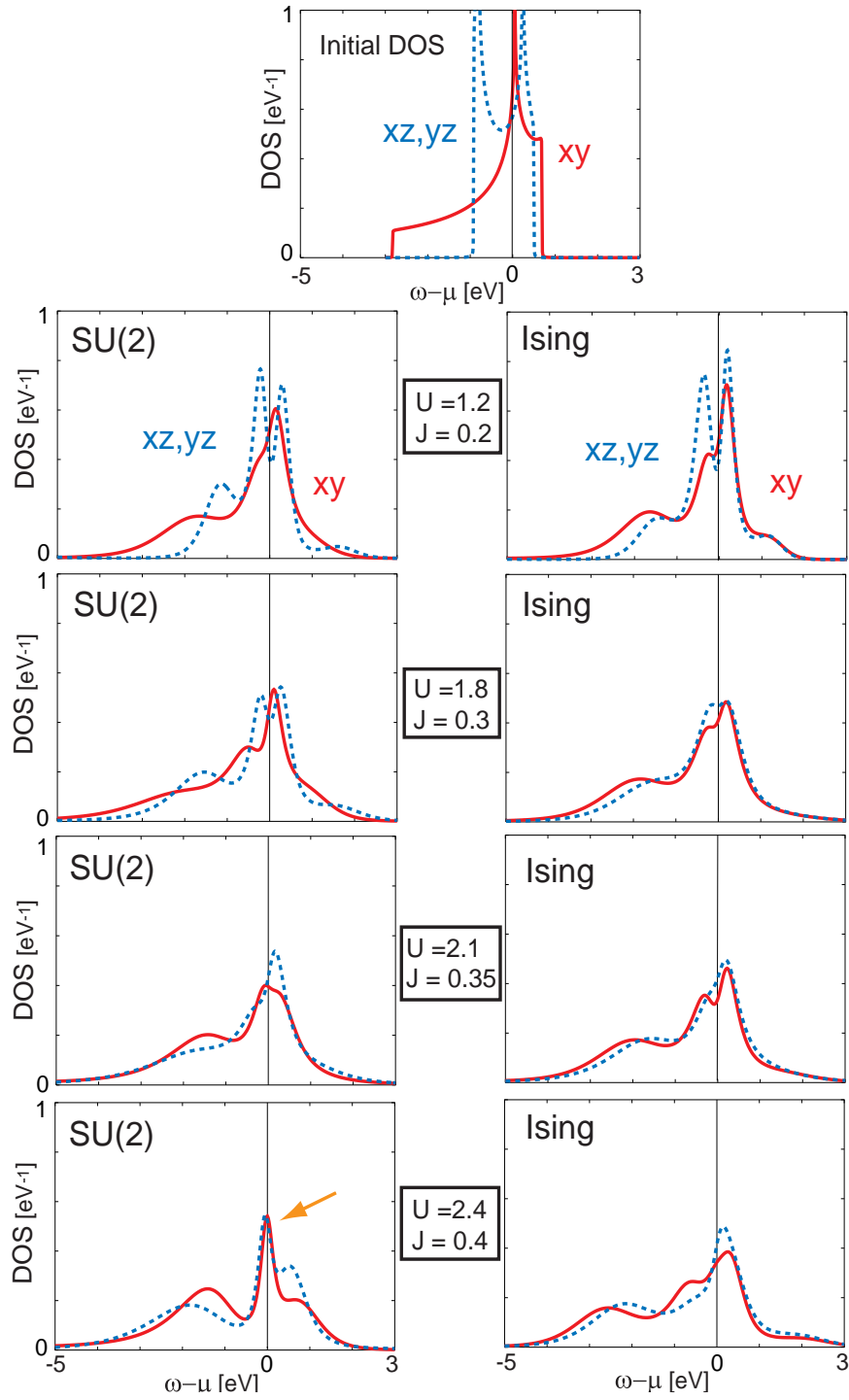


Figure 6.6: The LDA+DMFT DOS for Ru- $t_{2g}$  orbitals in  $\text{Sr}_2\text{RuO}_4$ , obtained with SU(2) Hund's coupling and the pair-hopping interaction (left panels), as compared with the DOS with Ising Hund's coupling (right). The ratio of the interactions is fixed as  $U = 1.5U' = 6J$ . The top panel displays the tight-binding-fitted LDA DOS [same as Fig. 6.1(b)]. The arrow in the lower left panel indicates the quasiparticle peak discussed in the text.

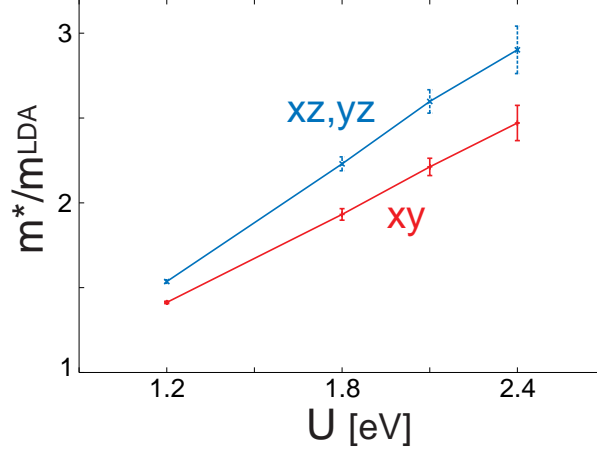


Figure 6.7: The quasiparticle mass enhancement for Ru- $t_{2g}$  orbitals of  $\text{Sr}_2\text{RuO}_4$ , obtained with the present SU(2)-symmetric calculation. The ratio of the interactions is fixed as  $U = 1.5U' = 6J$ . Lines are guide to the eye.

new structure emerges only for the SU(2) case, while the structure does not change so much in the Ising case. In the SU(2) case, a sharp quasiparticle peak, and pronounced lower and upper Hubbard peaks develop both for the  $xy$  and  $xz, yz$  bands.

## 6.4.2 Quasiparticle mass

We have calculated the quasiparticle mass enhancement  $m_a^*/m_a^{\text{LDA}}$  ( $a = xy, yz, zx$ ), where  $m_a^{\text{LDA}}$  is the band mass (i.e., mass for  $U=0$  in the present tight-binding model) and  $m_a^*$  is the mass obtained with the DMFT, from the imaginary part of the self-energy at the first Matsubara frequency  $i\omega_0 = i\pi T$ , using the relation,

$$\left(\frac{m_a^*}{m_a^{\text{LDA}}}\right)^{-1} \equiv 1 - \left.\frac{\partial \text{Re}\Sigma_a(\omega)}{\partial \omega}\right|_{\omega=0} \simeq 1 - \frac{\text{Im}\Sigma_a(i\omega_0)}{\omega_0}. \quad (6.5)$$

The result is plotted in Fig. 6.7. For both bands  $m_a^*/m_a^{\text{LDA}}$  increases almost linearly to  $U(= 6J)$ . For the largest parameters studied here,  $(U, J) = (2.4, 0.4)$  eV, the enhancement is about 2.5 for  $d_{xy}$  and about 2.9 for  $d_{xz,yz}$ , which are in agreement with experimental estimates ( $\sim 3$ ), but are somewhat smaller. Similar values are obtained with Ising Hund's coupling.

## 6.5 Discussion

First we discuss the different behaviors in the DOS for  $(U, J) = (2.4, 0.4)$  eV between the Ising and SU(2) Hund couplings. The behavior in the SU(2) case is similar to that for the single-orbital Hubbard model in the vicinity of Mott's transition, where the quasiparticle peak is interpreted as a Kondo resonance peak. Then the different behavior between the

Ising and SU(2) cases may be attributed to the different ease with which a Kondo singlet is formed.

Concerning the difference in the multiorbital system, we may refer to the discussion by Arita and Held [176] for the orbital-selective Mott transition in the two-orbital Hubbard model (see §3.3.4): For  $J > T_K$  ( $T_K$ : Kondo temperature) two electrons in the two different orbitals form a stiff spin-1 state. In SU(2) case, the spin-1 state can be screened by conduction electrons in two stages by spin  $\frac{1}{2}$ , while the two-stage screening is not possible in Ising case since the two-electron state with  $S^z = 0$  is higher in energy by  $J$  than the states with  $S^z = \pm 1$  (*cf.* Fig. 2.2). Actually, in the metallic phase near the orbital-selective Mott transition, a sharp quasiparticle peak has been observed for SU(2) Hund's coupling [104, 176], while it has not been observed for Ising Hund's coupling [165, 166, 169].

In the present three-orbital case, the difference between Ising and SU(2) is expected to be more pronounced, since the energy splitting between  $S^z = \pm\frac{3}{2}$  and  $S^z = \pm\frac{1}{2}$  in the Ising case is  $2J$ , which is twice the value for two-orbital Ising-type models.

Thus, although we took Sr<sub>2</sub>RuO<sub>4</sub> as an example, the different behaviors in the DOS should be a general consequence for multiorbital systems with  $J > T_K$ , not only for the present material. Since  $T_K$  approximates  $zW$  ( $z = \frac{m}{m^*}$ : the mass renormalization factor), the difference may be more prominent in the vicinity of Mott's transition. This means that the inclusion of SU(2) symmetric Hund's coupling and the pair-hopping interaction is requisite for realistic calculations for strongly correlated materials. Although most of the LDA+DMFT studies so far have employed Ising-type Hund's coupling, the treatment will underestimate the quasiparticle resonance.

Here we compare the present results with an experimental one. In Fig. 6.8 we plot the present SU(2)-symmetric calculation with the photoemission spectrum [195], where the theoretical spectra are multiplied by the Fermi function at 20K to adapt the experimental condition. We see that the present DMFT spectra are remarkably closer to the experimental result than the LDA spectrum. For all the  $(U, J)$  from (1.2, 0.2) to (2.4, 0.4) eV, the height and the width of the quasiparticle spectrum are considerably reduced from the LDA result. Although we can see a quasiparticle peak in the experimental spectra, we cannot distinguish whether it derives from the van Hove singularity in the original band-structure or from a formation of the Kondo singlet. We can also see a peak structure at around  $-2$  eV, which is considered to be a precursor of the lower Hubbard band. However, the position of the lower Hubbard peak is about 1 eV higher than the experimental assignment. Also, the mass enhancement in Fig. 6.7 is about 1.5 for  $(U, J) = (1.2, 0.2)$  eV and about 2.5 for  $(U, J) = (2.4, 0.4)$  eV, which are considerably improved from the LDA result but are still smaller than the experimental estimate ( $\sim 3$ ).

A part of these disagreements may be attributed to the fixed ratio of the interaction parameters we have taken, i.e.,  $U = 1.5U' = 6J$ , since we know that the mass enhancement in multiorbital systems highly depends on the balance between  $U$ ,  $U'$  and  $J$ , as well as their strengths: For example,  $J$  considerably increases the mass, as shown in Fig. 2.3(a).

Another reason for the above disagreements may be the neglect of the momentum dependence of the self-energy in the DMFT. Since Sr<sub>2</sub>RuO<sub>4</sub> is a quasi-two-dimensional system, the momentum dependence may be significant. Such momentum dependence

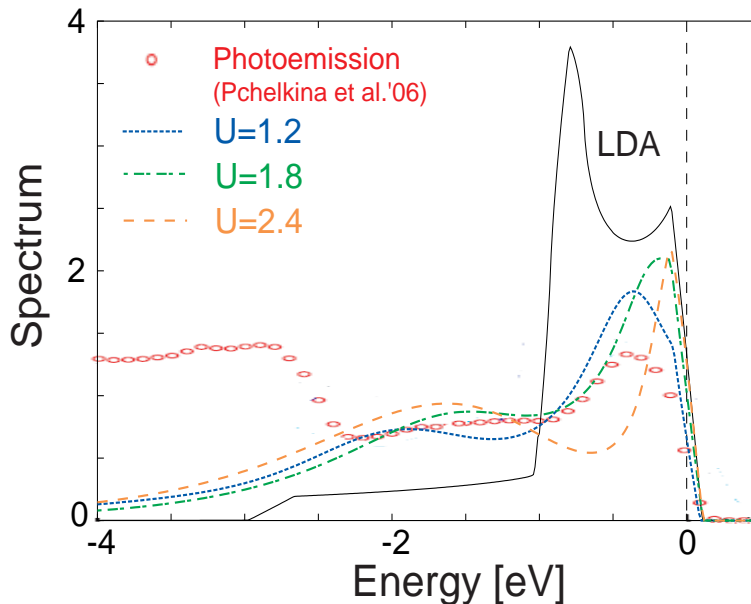


Figure 6.8: The comparison of the present result for the quasiparticle spectra with a photoemission result for  $\text{Sr}_2\text{RuO}_4$ . Solid curve represents the tight-binding-fitted LDA spectrum (i.e.,  $U = 0$  data for the tight-binding model), while dashed curves the results calculated for  $U = 6J = 1.2, 1.8$  and  $2.4$  eV. Circles are the photoemission data from Ref. [195]. The theoretical spectra are multiplied by the Fermi function at 20 K.

can, in principle, be taken into account with the cluster extensions of the DMFT [26], [144]-[154], [217] while such a calculation for three-orbital systems is too demanding to implement at present.

Also there may be other contributions, e.g., from the electron-phonon coupling [122, 266] or from the spin-orbit interactions [84, 259]. The estimation of the contributions from these effects requires further investigations.

## 6.6 Summary

We have demonstrated that the QMC algorithm developed in §4.5 can be applied to a real material with three orbitals.

We took  $\text{Sr}_2\text{RuO}_4$  for the test, and compared the dependence of the DOS on the interaction strength between Ising and  $\text{SU}(2)$  Hund's couplings. For an intermediate coupling  $[(U, J) = (2.4, 0.4)$  eV] we saw a remarkable difference between the Ising and  $\text{SU}(2)$  spectra: a sharp quasiparticle peak appears in the  $\text{SU}(2)$  case, while it does not in the Ising case. We attribute this difference to the different formations of the Kondo singlet for these two types of Hund's coupling. This is expected to generally apply to multiorbital materials, not only to  $\text{Sr}_2\text{RuO}_4$ . Although most of the LDA+DMFT studies so far have invoked the Ising-type Hund coupling, the present result indicates the importance of the rotationally symmetric Hund coupling and the pair-hopping interaction.

The quasiparticle spectra obtained in the present SU(2)-symmetric calculation tend to have smaller quasiparticle bandwidths and the weights, and reproduce the lower Hubbard peak, in agreement with the photoemission experiments. The present calculation also provides an effective mass much improved from the LDA result. However, the calculated position of the lower Hubbard peak is about 1 eV higher in energy than the experimental assignment. Also the effective mass is still smaller than experimental estimates. These disagreements require further studies, including estimations of more realistic values of the interaction parameters and a treatment of the momentum dependence of the self-energy, as well as an estimation of the contribution from the electron-phonon [122, 266] and the spin-orbit interactions [84, 259].

# Chapter 7

## Concluding remarks

### 7.1 Summary of the thesis

We have investigated the multiorbital Hubbard model (2.9) with the dynamical mean-field theory (DMFT), where our main interest is the effects of Hund's coupling in multiorbital systems.

· *Development of a new QMC method*

To study the effect, we have especially paid attention on the spin and orbital rotational symmetries in the Hamiltonian (2.9). The conventional Hirsch-Fye quantum Monte Carlo (QMC) method, which solves an effective impurity model in the DMFT, has difficulties in treating the spin-flip and the pair-hopping interactions. So most DMFT+QMC calculations have heretofore neglected these interactions, which violates the spin and orbital rotational symmetries.

To overcome the adversity, we have developed a novel auxiliary-field QMC method in §4.5. In the algorithm we separate out interaction terms from one-body part of the Hamiltonian, using a series expansion for the spin-flip and the pair-hopping terms ( $\hat{H}_J$ ) while the Trotter decomposition for the density-density interactions ( $\hat{H}_U$ ). Then we decouple the interaction terms by use of the conventional Hubbard-Stratonovich transformation for  $\hat{H}_U$ , and a new auxiliary-field transformation for  $\hat{H}_J$ .

The algorithm allows for spin- and orbital-rotational symmetric calculations not only for two but for three or more orbital systems. This is important since there are many real materials which involve three or more orbitals. The algorithm also considerably improves the negative sign problem coming from  $\hat{H}_J$  term (§4.3). The reduction of negative signs is a great advantage already for two-orbital systems.

· *Itinerant ferromagnetism in multiorbital systems*

We have investigated the metallic ferromagnetism in multiorbital systems with the present QMC method in combination with the DMFT. We calculated the spin susceptibility for the double-orbital Hubbard model in a paramagnetic phase. First we showed that the Ising treatment of the Hund exchange grossly overestimates the ferromagnetic instability (§5.2). Then we examined effects of interorbital interactions ( $U'$  and  $J$ ) on *itinerant* ferromagnetism in multiorbital systems (§5.3), where our eyes are set on the

problem whether metallic ferromagnetism in transition metals and their compounds can be attributed to a single mechanism; lattice structure *or* Hund's exchange. We have compared the magnetic susceptibility for the cubic and the fcc lattices in three dimensions, in the presence and the absence of Hund's exchange coupling. Our results show that the interorbital interactions significantly affect the ferromagnetic instability, in contrast to the Kanamori theory, where the interorbital interactions are considered to have only minor effects on metallic ferromagnetism. Our results indicate that both the lattice structure *and* Hund's exchange are crucial for the stability of the itinerant ferromagnetism in transition-metal-based materials.

· *Application to a three-orbital system —  $Sr_2RuO_4$*

Next we have demonstrated that the present algorithm is applicable to a three-orbital model with a realistic bandstructure and interaction parameters for  $Sr_2RuO_4$ , as the first QMC calculation for three-orbital systems and for the LDA+DMFT method in the presence of spin and orbital rotational symmetries. We showed that the quasiparticle spectra substantially differ between with the Ising and SU(2) Hund couplings for an intermediate-coupling region. In particular, we found a remarkable enhancement of a quasiparticle peak in the SU(2) spectra while we found no such structure in the Ising spectra. We attributed the difference to the different formations of a Kondo singlet in the effective impurity model for SU(2) and Ising Hund's couplings. The comparison with experimental photoemission spectrum shows an improvement in the present spectrum over the LDA result, although there remain some discrepancies between the present and experimental results.

## 7.2 Future problems

In the following we mention some future problems.

· *Effect of anisotropy of  $d$  orbitals*

In Chapter 5 we discussed itinerant ferromagnetism in the multiorbital Hubbard model, using the the dispersion (5.13) for the simple cubic lattice and (5.14) for the fcc lattice, where we have assumed that the electron transfers are isotropic, to make the discussions simple.

In reality, however,  $d$  orbitals have anisotropic shapes, so that the transfers in general depend on the orbitals and the directions. A study taking account of the anisotropy is under way.

· *Ferromagnetism in bcc Fe*

In connection with the above argument, we are interested in ferromagnetism in bcc Fe. Experimentally, the Curie temperature of Fe ( $T_c = 1043$  K) is much higher than that of Ni ( $T_c = 631$  K). An LDA+DMFT calculation [210] also found Fe to have a Curie temperature much higher than that for Ni, although the values should be overestimated for both materials owing to the Ising treatment of Hund's coupling.

However, some preliminary calculations for a bcc lattice with isotropic transfers show that ferromagnetism is less favored in the bcc lattice than in the fcc lattice, in agreement with a single-orbital case [143]. Therefore, it may be necessary to take account of the

anisotropy of the  $d$  orbitals to account for the high Curie temperature of bcc Fe. A study in this direction is also under way.

· *LDA+DMFT for other ruthenates*

A series of ruthenates have various intriguing properties. In particular, the Ruddlesden-Popper-type perovskite strontium ruthenates,  $\text{Sr}_{n+1}\text{Ru}_n\text{O}_{3n+1}$ , show spin-triplet superconductivity for  $n = 1$  [2, 78], metamagnetic quantum criticality for  $n = 2$  [267], ferromagnetism for  $n = 3$  [268] and  $n = \infty$  ( $\text{SrRuO}_3$ ) [269]. This implies some relevance of the ferromagnetism to the dimensionality in the ruthenates. The antiferromagnetic Mott insulator  $\text{Ca}_2\text{RuO}_4$  also becomes a ferromagnetic metal under pressure [270].

It is challenging to see whether the diverse properties can be reproduced in the present scheme.

# Appendix

We derive here the factor  $F(k; s_1, s_2, \dots, s_L)$  ( $s_i = 0, 1; k = \sum_{i=1}^L s_i$ ) for Eq. (4.32). We introduce this factor to account for the contribution from the terms with consecutive  $\hat{X}_1$ 's at the same imaginary-time interval in the sum (4.31). These terms have been replaced with terms having  $\hat{X}_1$ 's on proximate imaginary-time intervals in Eq. (4.32). In the following we abbreviate  $e^{-\Delta\tau(\hat{H}_0 + \hat{H}_U)}$  as  $h$ , and  $\hat{X}_1$  as  $x$ .

Central to our consideration are those terms that include a substring  $xhxhx \cdots hx$  where  $x$  and  $h$  appear alternately  $m$  and  $m - 1$  times, respectively, with  $2 \leq m \leq L$ . This is because any term with consecutive  $x$ 's will be replaced with a term having such substrings. For example,  $xxhhx \cdots hx$  and  $xhxxh \cdots hx$  are both approximately the same as  $xhxhx \cdots hx$  [where commuting an  $x$  and a  $h$  yields an error  $\sim O(\Delta\tau)$ ]. In general, we commute  $x$ 's and  $h$ 's until there are no consecutive  $x$ 's any longer. Hence, we end up with an alternation of  $x$ 's and  $h$ 's, i.e., an  $xhxhx \cdots hx$  substring. Because of these replacements, terms having such a substring have to be weighted more. In the following, we construct a rule for the replacement and weighting factor, avoiding a double counting.

Let us denote by  $i$  a position (from the left) in a substring which consists of  $m$   $x$ 's and  $(m - 1)$   $h$ 's altogether. We define  $\alpha_i$  and  $\beta_i$  as the number of  $x$ 's and  $h$ 's that are in  $[1, i]$ . All substrings having

$$\alpha_i \geq \beta_i \quad \text{for all } i \quad (7.1)$$

will be replaced with  $xhxhx \cdots hx$  which has alternating  $x$ 's and  $h$ 's.

For example, for  $m = 2$   $xhx$  and  $xxh$  will be replaced with  $xhx$ ; for  $m = 3$ ,  $xhxhx$ ,  $xhxxh$ ,  $xxhhx$ ,  $xxhxxh$  and  $xxhxxh$  will all be replaced with  $xhxhx$ . The condition (7.1) is necessary to avoid a double counting. However, the condition (7.1) excludes the substrings situated at the end of the imaginary time interval for which  $\exists i'$ , so that  $\alpha_{i'} < \beta_{i'}$ . These terms are replaced with a substring  $xhxhx \cdots hx$ , where the last  $x$  is at  $L$ , namely, only when the last  $x$  is at  $L$ , does  $xhxhx \cdots hx$  replace all the substrings having  $m$   $x$ 's and  $(m - 1)$   $h$ 's, which requires a separate treatment ( $c$  factors below).

A second factor to be taken into account is a correction of the volume in the imaginary-time integrals; namely, the weight for those terms having consecutive  $x$ 's at

$$j_i \neq j_{i+1} = j_{i+2} = \cdots = j_{i+l} \neq j_{i+l+1} \quad (7.2)$$

in the sum (4.31) should be reduced by a factor  $\frac{1}{l!}$ , since the imaginary times originally satisfy a relation

$$t_{i+1} < t_{i+2} < \cdots < t_{i+l} \quad (7.3)$$

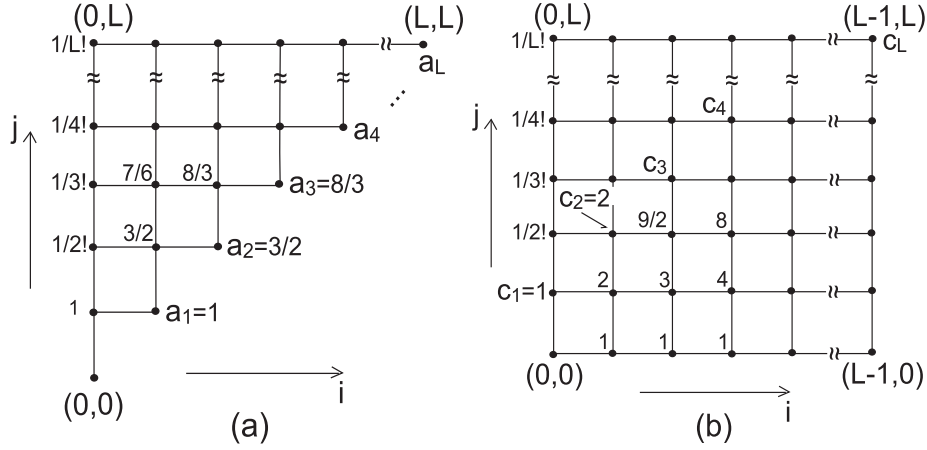


Figure 7.1: A schematic representation of the calculation of (a)  $a_m$  and (b)  $c_m$ . The coordinates in the  $i$  and  $j$  directions represent the numbers of  $h$  and  $x$ , respectively. The number at a point  $(i, j)$  denotes (a)  $b(i, j)$  and (b)  $d(i, j)$ , which are recursively calculated with Eq. (7.5) and (7.7), respectively.

in Eq. (4.30). Hence the volume for  $l$  consecutive  $x$  terms, as in Eq. (7.2), should be reduced to  $\frac{L^{-l}}{l!}$ .

Let us now introduce the quantity  $b(i, j)$  for the weight (apart from the volume factor  $L^{-j}$ ) of all the substrings having  $i$   $h$ 's and  $j$   $x$ 's. For  $j$  consecutive  $x$ 's, we simply have the aforementioned  $1/l!$  factor, i.e.,

$$b(0, j) = \frac{1}{j!} \quad \text{for } 0 \leq j \leq L. \quad (7.4)$$

This is the starting point for the recurrence formula [Fig. 7.1(a)],

$$b(i, j) = \sum_{k=i}^j \frac{1}{(j-k)!} b(i-1, k) \quad \text{for } 1 \leq i \leq j \leq L, \quad (7.5)$$

which arises from taking away the rightmost elements of the type  $hxxx \cdots x$  with  $(j-k)$   $x$ 's from the substring of length  $i+j$ . At the end, the recurrence formula (7.5) yields the weighting factor  $a_i$  for the substring ' $xhxx \cdots hx$ ' with  $m$   $x$ 's and  $m-1$   $h$ 's:

$$a_i = b(i-1, i) = b(i, i) \quad \text{for } 1 \leq i \leq L. \quad (7.6)$$

Only when the last  $x$  in  $xhxx \cdots hx$  is situated at the end of the imaginary-time interval ( $L$ ) do we use the factor  $c_m$  instead, which is obtained via the slightly different recurrence

formula [see Fig. 7.1(b)],

$$\begin{aligned}
 d(0, j) &= \frac{1}{j!} \quad \text{for } 0 \leq j \leq L, \\
 d(i, j) &= \sum_{k=0}^j \frac{1}{(j-k)!} d(i-1, k) \\
 &\quad \text{for } 1 \leq i \leq L-1 \text{ and } 0 \leq j \leq L, \\
 c_i &= d(i-1, i) \quad \text{for } 1 \leq i \leq L.
 \end{aligned} \tag{7.7}$$

From the  $a$ 's and  $c$ 's, the total weight  $F$  is calculated by multiplying the contributions  $a_m$  and  $c_m$  from each  $xhxhx\dots hx$ -type substring in the Boltzmann factor and the volume  $L^{-k}$ . For example, for  $L = 8$ ,

$$\begin{aligned}
 F(2; 1, 1, 0, 0, 0, 0, 0, 0) &= a_2 L^{-2}, \\
 F(5; 0, 1, 0, 1, 0, 1, 1, 1) &= c_3 L^{-5}, \\
 F(6; 1, 0, 1, 1, 0, 1, 1, 1) &= a_2 c_3 L^{-6}.
 \end{aligned} \tag{7.8}$$

In the first example, the Boltzmann factor is  $hxhxhhhhhh$ . This array replaces itself and  $hxxhhhhhhh$ , which is weighted  $\frac{1}{2!}$ , and thereby the factor for  $hxhxhhhhhh$  is  $a_2 = 1 + \frac{1}{2!} = \frac{3}{2}$  multiplied by  $L^{-2}$ . The second example corresponds to  $hxhxhxhxhxhx$   $hx$ , where the substring to be multiplied by a factor is only the last part  $xhxhx$ . Therefore the factor is  $c_3 L^{-5}$ . In the last example  $hxhhxhxhhxhxhx$ , two substrings  $xhx$  and  $xhxhx$  are multiplied by  $a_2$  and  $c_3$ , respectively. So the total factor is  $a_2 \times c_3 L^{-6}$ .

# Bibliography

- [1] J.G. Bednorz and K.A. Müller, *Z. Phys. B* **64**, 189 (1986).
- [2] Y. Maeno, H. Hashimoto, K. Yoshida, S. Nishizaki, T. Fujita, J.G. Bednorz, and F. Lichtenberg, *Nature* **372**, 532 (1994).
- [3] B. Raveau, A. Maignan, and V. Caignaert, *J. Solid State Chem.* **117**, 424 (1995).
- [4] Y. Tomioka, A. Asamitsu, Y. Moritomo, H. Kuwahara, and Y. Tokura, *Phys. Rev. Lett.* **74**, 5108; Y. Tomioka, A. Asamitsu, Y. Moritomo, and Y. Tokura, *J. Phys. Soc. Jpn.* **64**, 3626 (1995).
- [5] C.N.R. Rao, A.K. Cheetham, and R. Mahesh, *Chem. Mater.* **8**, 2421 (1996).
- [6] Y. Tokura and N. Nagaosa, *Science* **288**, 462 (2000).
- [7] P.M. Raccah and J.B. Goodenough, *Phys. Rev.* **155**, 932 (1967).
- [8] M. Abbate, J.C. Fuggle, A. Fujimori, L.H. Tjeng, C.T. Chen, R. Potze, G.A. Sawatzky, H. Eisaki, and S. Uchida, *Phys. Rev. B* **47**, 16124 (1993).
- [9] D. Louca, J.L. Sarrao, J.D. Thompson, H. Röder, and G.H. Kwei, *Phys. Rev. B* **60**, 10378 (1999).
- [10] J. Hubbard, *Proc. R. Soc. London A* **276**, 238 (1963); **281**, 401 (1964).
- [11] J.H. de Boer and E.J.W. Verway, *Proc. Phys. Soc. London, Sect A* **49**, 59 (1937).
- [12] N.F. Mott and R. Peierls, *Proc. Phys. Soc. London, Sect A* **49**, 72 (1937).
- [13] N.F. Mott, *Proc. Phys. Soc. London, Sect A* **62**, 416 (1949).
- [14] M. Imada, A. Fujimori, and Y. Tokura, *Rev. Mod. Phys.* **70**, 1039 (1998).
- [15] A. Fujimori, *J. Phys. Chem. Solids* **53**, 1595 (1992).
- [16] D.B. McWhan, J.P. Remeika, T.M. Rice, W.F. Brinkman, J.P. Maita, and A. Menth, *Phys. Rev. Lett.* **27**, 941 (1971); D.B. McWhan, A. Menth, J.P. Remeika, W.F. Brinkman, and T.M. Rice, *Phys. Rev. B* **7**, 1920 (1973).
- [17] W.F. Brinkman and T.M. Rice, *Phys. Rev. B* **2**, 4302 (1970).

- [18] A. Georges, G. Kotliar, W. Krauth, and M.J. Rozenberg, *Rev. Mod. Phys.* **68**, 13 (1996).
- [19] N. Furukawa and M. Imada, *J. Phys. Soc. Jpn.* **60**, 3604 (1991); **61**, 3331 (1992); **62**, 2557; *Physica B* **186-188**, 931 (1993); N. Furukawa, F.F. Assaad, and M. Imada, *J. Phys. Soc. Jpn.* **65**, 2339 (1996).
- [20] M. Jarrell, *Phys. Rev. Lett.* **69**, 168 (1992).
- [21] M.J. Rozenberg, X.Y. Zhang, and G. Kotliar, *Phys. Rev. Lett.* **69**, 1236 (1992); X.Y. Zhang, M.J. Rozenberg, and G. Kotliar, *ibid.* **70**, 1666 (1993); M.J. Rozenberg, G. Kotliar, and X.Y. Zhang, *Phys. Rev. B* **49**, 10181 (1994); M.J. Rozenberg, R. Chitra, and G. Kotliar, *Phys. Rev. Lett.* **83**, 3498 (1999).
- [22] M. Jarrell, Th. Pruschke, *Z. Phys. B* **90**, 187 (1993).
- [23] M. Imada, *J. Phys. Soc. Jpn.* **63**, 3059 (1994); **64**, 2954 (1995); **73**, 1851; **74**, 859 (2003); *Phys. Rev. B* **72**, 075113 (2005).
- [24] G. Moeller, Q. Si, G. Kotliar, M. Rozenberg, and D.S. Fisher, *Phys. Rev. Lett.* **74**, 2082; D.S. Fisher, G. Kotliar, and G. Moeller, *Phys. Rev. B* **52**, 17112 (1995).
- [25] F.F. Assaad and M. Imada, *Phys. Rev. Lett.* **76**, 3176 (1996); *Phys. Rev. B* **58**, 1845 (1998).
- [26] S. Onoda and M. Imada, *J. Phys. Soc. Jpn.* **70**, 3398; 632 (2001); *Phys. Rev. B* **67**, 161102(R) (2003) K. Hanasaki and M. Imada, *J. Phys. Soc. Jpn* **75**, 084702 (2006).
- [27] G. Kotliar, S. Murthy, and M.J. Rozenberg, *Phys. Rev. Lett.* **89**, 046401 (2002).
- [28] S. Watanabe and M. Imada, *J. Phys. Soc. Jpn.* **73**, 1251 (2004).
- [29] M. Imada and T. Kashima, *J. Phys. Soc. Jpn.* **69**, 2723 (2000); T. Kashima and M. Imada, *ibid.* **70**, 2287 (2001).
- [30] J. Kanamori, *Prog. Theor. Phys.* **30**, 275 (1963).
- [31] M.C. Gutzwiller, *Phys. Rev. Lett.* **10**, 159 (1963).
- [32] H. Tasaki, *Prog. Theor. Phys.* **99**, 489 (1998).
- [33] Y. Nagaoka, *Phys. Rev.* **147**, 392 (1966).
- [34] E.H. Lieb, *Phys. Rev. Lett.* **62**, 1201 (1989).
- [35] A. Mielke, *J. Phys. A* **24**, L73 ; 311 (1991); **25**, 4335 (1992).
- [36] H. Tasaki, *Phys. Rev. Lett.* **69**, 1608 (1992).
- [37] A. Mielke and H. Tasaki, *Commun. Math. Phys.* **158**, 341 (1993).

- [38] J.C. Slater, Phys. Rev. **49**, 537; 931 (1936); **52**, 198 (1937); J.C. Slater, H. Statz, and G.F. Koster, *ibid.* **91**, 1323 (1953).
- [39] J.H. van Vleck, Rev. Mod. Phys. **25**, 220 (1953).
- [40] D.J. Scalapino, Phys. Rep. **250**, 329 (1995).
- [41] J.E. Hirsch, Phys. Rev. Lett. **85**, 1317 (1985).
- [42] K. Miyake, S. Schmitt-Rink, and C.M. Varma, Phys. Rev. B **34**, 6554 (1986).
- [43] D.J. Scalapino, E. Loh, Jr., and J.E. Hirsch, Phys. Rev. B **35**, 6694 (1987).
- [44] N.E. Bickers, D.J. Scalapino, and S.R. White, Phys. Rev. Lett. **62**, 961; N.E. Bickers and D.J. Scalapino, Ann. Phys. (N.Y.) **193**, 206 (1989); N.E. Bickers and S.R. White, Phys. Rev. B **43**, 8044 (1991).
- [45] T. Moriya and Y. Takahashi, J. Phys. Soc. Jpn. **60**, 776 (1991); T. Moriya and K. Ueda, Adv. Phys. **49**, 555 (2000); Rep. Prog. Phys. **66**, 1200 (2003).
- [46] S.R. White, D.J. Scalapino, R.L. Suger, N.E. Bickers, and R.T. Scaletter, Phys. Rev. B **39**, 839(R); S.R. White, D.J. Scalapino, R.L. Suger, E.Y. Loh, J.E. Gubernatis, and R.T. Scaletter, *ibid.* **40**, 506 (1989).
- [47] S. Zhang, J. Carlson, and J.E. Gubernatis, Phys. Rev. Lett. **78**, 4486 (1997).
- [48] K. Kuroki and H. Aoki, Phys. Rev. B **56**, R14287 (1997).
- [49] Th. Maier, M. Jarrell, Th. Pruschke, and J. Keller, Phys. Rev. Lett. **85**, 1524 (2000); G. Su, *ibid.* **86**, 3690; Th. Maier, M. Jarrell, and Th. Pruschke, *ibid.* **86**, 3691; M. Jarrell, Th. Maier, M.H. Hettler, and A.N. Tahvildarzadeh, Europhys. Lett. **56**, 563 (2001); Th. Maier, M. Jarrell, A. Macridin, and C. Slezak, Phys. Rev. Lett. **92**, 027005 (2004); Th. Maier, M. Jarrell, T.C. Schulthess, P.R.C. Kent, and J.B. White, *ibid.* **95**, 237001; A. Macridin, M. Jarrell, Th. Maier, and G.A. Sawatzky, Phys. Rev. B **71**, 134527 (2005).
- [50] Th. Maier, M. Jarrell, Th. Pruschke, and M.H. Hettler, Rev. Mod. Phys. **77**, 1027 (2005).
- [51] N.D. Mermin and H. Wagner, Phys. Rev. Lett. **17**, 1133 (1966).
- [52] J. Kosterlitz and D. Thouless, J. Phys. C **6**, 1181 (1973).
- [53] K. Takada, H. Sakurai, E. Takayama-Muromachi, F. Izumi, R.A. Dilanian, and T. Sasaki, Nature **422**, 53 (2003).
- [54] K. Ishida, H. Mukuda, Y. Kitaoka, K. Asayama, Z.Q. Mao, Y. Mori, and Y. Maeno, Nature **396**, 658; G.M. Luke, Y. Fudamoto, K.M. Kojima, M.I. Larkin, J. Merrin, B. Nachumi, Y.J. Uemura, Y. Maeno, Z.Q. Mao, Y. Mori, H. Nakamura, and M. Sgrist, *ibid.* **394**, 558 (1998).

- [55] E.R. Davidson, J. Chem. Phys. **41**, 656 (1964); **42**, 4199 (1965).
- [56] K. Hongo, R. Maezono, Y. Kawazoe, H. Yasuhara, M.D. Towler, and R.J. Needs, J. Chem. Phys. **121**, 7144 (2004).
- [57] K.I. Kugel' and D.I. Khomskii, Sov. Phys. JETP **37**, 725 (1973).
- [58] L.M. Roth, Phys. Rev. **149**, 306 (1966).
- [59] M.A. Korotin, S. Yu. Ezhov, I.V. Solovyev, V.I. Anisimov, D.I. Khomskii, and G.A. Sawatzky, Phys. Rev. B **54**, 5309 (1996).
- [60] T. Mizokawa and A. Fujimori, Phys. Rev. B **54**, 5368 (1996).
- [61] T. Saitoh, T. Mizokawa, A. Fujimori, M. Abbate, Y. Takeda, and M. Takano, Phys. Rev. B **55**, 4257 (1997).
- [62] P. Ravindran, H. Fjellvåg, A. Kjekshus, P. Blaha, K. Schwarz, and J. Luitz, J. Appl. Phys. **91**, 291 (2002).
- [63] Y. Murakami, H. Kawada, H. Kawata, M. Tanaka, T. Arima, Y. Moritomo, and Y. Tokura, Phys. Rev. Lett. **80**, 1932; Y. Murakami, J.P. Hill, D. Gibbs, M. Blume, I. Koyama, M. Tanaka, H. Kawata, T. Arima, Y. Tokura, K. Hirota, and Y. Endoh, *ibid.* **81**, 582 (1998).
- [64] M. Noguchi, A. Nakazawa, S. Oka, T. Arima, Y. Wakabayashi, H. Nakao, and Y. Murakami, Phys. Rev. B **62**, R9271 (2000).
- [65] S. Miyasaka, Y. Okimoto, and Y. Tokura, J. Phys. Soc. Jpn. **71**, 2086 (2002).
- [66] H. Sawada, N. Hamada, K. Terakura, and T. Asada, Phys. Rev. B **53**, 12742 (1996).
- [67] H. Ichikawa, J. Akimitsu, M. Nishi, and K. Kakurai, Physica B **281-282**, 482 (2000).
- [68] M. Mochizuki, M. Imada, Phys. Rev. Lett. **91**, 167203 (2003); J. Phys. Soc. Jpn. **73**, 1833 (2004); M. Mochizuki, *ibid.* **71**, 2039 (2002).
- [69] H. Kawano, H. Yoshizawa, and Y. Ueda, J. Phys. Soc. Jpn. **63**, 2857 (1994).
- [70] Y. Ihara, K. Ishida, H. Takeya, C. Michioka, M. Kato, Y. Itoh, K. Yoshimura, K. Takada, T. Sasaki, H. Sakurai, and E. Takayama-Muromachi, J. Phys. Soc. Jpn. **75**, 013708 (2006).
- [71] T. Fujimoto, G.-Q. Zheng, Y. Kitaoka, R.L. Meng, J. Cmaidalka, and C.W. Chu, Phys. Rev. Lett. **92**, 047004 (2004).
- [72] Y. Kobayashi, H. Watanabe, M. Yokoi, T. Moyoshi, Y. Mori, and M. Sato, J. Phys. Soc. Jpn. **74**, 1800 (2005).

- [73] M. Mochizuki, Y. Yanase, and M. Ogata, Phys. Rev. Lett. **94**, 147005; J. Phys. Soc. Jpn. **74**, 1670 (2005).
- [74] Y. Yanase, M. Mochizuki, and M. Ogata, J. Phys. Soc. Jpn. **74**, 430 (2005).
- [75] G. Baskaran, Phys. Rev. Lett. **91**, 097003 (2003).
- [76] M.D. Johannes, I.I. Mazin, D.J. Singh, and D.A. Papaconstantopoulos, Phys. Rev. Lett. **93**, 097005 (2004).
- [77] K. Kuroki, Y. Tanaka, and R. Arita, Phys. Rev. Lett. **93**, 077001 (2004); K. Kuroki, S. Onari, Y. Tanaka, R. Arita, and T. Nojima, Phys. Rev. B **73**, 184503 (2006).
- [78] A.P. Mackenzie and Y. Maeno, Rev. Mod. Phys. **75**, 657 (2003); C. Bergemann, A.P. Mackenzie, S.R. Julian, D. Forsythe, and E. Ohmichi, Adv. Phys. **52**, 639 (2003).
- [79] S. Nakatsuji and Y. Maeno, Phys. Rev. Lett. **84**, 2666 (2000); S. Nakatsuji, D. Hall, L. Balicas, Z. Fisk, K. Sugahara, M. Yoshioka, and Y. Maeno, *ibid.* **90**, 137202 (2003).
- [80] S. Nakatsuji, S. Ikeda, and Y. Maeno, J. Phys. Soc. Jpn. **66**, 1868 (1997).
- [81] M. Braden, G. André, S. Nakatsuji, and Y. Maeno, Phys. Rev. B **58**, 847 (1998); O. Friedt, M. Braden, G. André, P. Adelman, S. Nakatsuji, and Y. Maeno, *ibid.* **63**, 174432 (2001).
- [82] Z. Fang and K. Terakura, Phys. Rev. B **64**, 020509(R) (2001).
- [83] V.I. Anisimov, I.A. Nekrasov, D.E. Kondakov, T.M. Rice, and M. Sigrist, Eur. Phys. J. B **25**, 191 (2002).
- [84] T. Mizokawa, L.H. Tjeng, G.A. Sawatzky, G. Ghiringhelli, O. Tjernberg, N.B. Brookes, H. Fukazawa, S. Nakatsuji, and Y. Maeno, Phys. Rev. Lett. **87**, 077202 (2001).
- [85] T. Hotta and E. Dagotto, Phys. Rev. Lett. **88**, 017201 (2001).
- [86] Z. Fang, N. Nagaosa, and K. Terakura, Phys. Rev. B **69**, 045116 (2004).
- [87] J. Kanamori, J. Phys. Chem. Solids **10**, 87 (1959).
- [88] A. Gukasov, M. Braden, R.J. Papoular, S. Nakatsuji, and Y. Maeno, Phys. Rev. Lett. **89**, 087202 (2002).
- [89] J.S. Lee, S.J. Moon, T.W. Noh, S. Nakatsuji, and Y. Maeno, Phys. Rev. Lett. **96**, 057401 (2006).
- [90] A.M. Oleś, Phys. Rev. B **28**, 327 (1983).

- [91] E. Antonides, E.C. Janse, and G.A. Sawatzky, *Phys. Rev. B* **15**, 1669 (1977).
- [92] Lo I Yin and T. Tsang, *Phys. Rev. B* **15**, 2974 (1977).
- [93] A. Fujimori, A.E. Bocquet, T. Saitoh, and T. Mizokawa, *J. Electron Spectrosc. Relat. Phenom.* **62**, 141 (1993).
- [94] M.R. Norman and A.J. Freeman, *Phys. Rev. B* **33**, 8896(R) (1986).
- [95] A.K. McMahan, R.M. Martin, and S. Satpathy, *Phys. Rev. B* **38**, 6650 (1988).
- [96] O. Gunnarsson, O.K. Andersen, O. Jepsen, and J. Zaanen, *Phys. Rev. B* **39**, 1708 (1989).
- [97] V.I. Anisimov, J. Zaanen, and O.K. Andersen, *Phys. Rev. B* **44**, 943 (1991).
- [98] I.V. Solovyev, *Phys. Rev. B* **73**, 155117 (2006).
- [99] K. Nakamura, R. Arita, Y. Yoshimoto, and S. Tsuneyuki, *Phys. Rev. B* **74**, 235113 (2006).
- [100] T. Kotani, *J. Phys.: Condens. Matter* **12**, 2413 (2000).
- [101] F. Aryasetiawan, M. Imada, A. Georges, G. Kotliar, S. Biermann, and A.I. Lichtenstein, *Phys. Rev. B* **70**, 195104 (2004).
- [102] F. Aryasetiawan, K. Karlsson, O. Jepsen, and U. Schönberger, *Phys. Rev. B* **74**, 125106 (2006).
- [103] M. Springer and F. Aryasetiawan, *Phys. Rev. B* **57**, 4364 (1998).
- [104] Th. Pruschke and R. Bulla, *Eur. Phys. J. B* **44**, 217 (2005).
- [105] W. Metzner and D. Vollhardt, *Phys. Rev. Lett.* **62**, 324 (1989).
- [106] F.J. Ohkawa, *J. Phys. Soc. Jpn.* **60**, 3218; *Prog. Theor. Phys. (Suppl.)* **106**, 95 (1991).
- [107] A. Georges and G. Kotliar, *Phys. Rev. B* **45**, 6479 (1992).
- [108] E. Müller-Hartmann, *Z. Phys. B* **74**, 507 (1989).
- [109] V. Zlatić and B. Horvatić, *Solid State Commun.* **75**, 263 (1990).
- [110] H. Schweitzer and G. Czycholl, *Z. Phys. B* **79**, 377 (1990); **83**, 93 (1991); *Solid State Commun.* **69**, 171 (1989); **74**, 735 (1990); *Phys. Rev. Lett.* **67**, 3724 (1991).
- [111] A. Georges, G. Kotliar, and Q. Si, *Int. J. Mod. Phys. B* **6**, 705 (1992); M.J. Rozenberg, G. Kotliar, and H. Kajueter, *Phys. Rev. B* **54**, 8452 (1996).

- [112] M. Jarrell, H. Akhlaghpour, and Th. Pruschke, Phys. Rev. Lett. **70**, 1670 (1993); M. Jarrell, Phys. Rev. B **51**, 7429 (1995).
- [113] S.-J. Sun, M.-F. Yang, and T.-M. Hong, Phys. Rev. B **48**, 16127 (1993).
- [114] T. Mutou and D.S. Hirashima, J. Phys. Soc. Jpn. **63**, 4475 (1994); **64**, 4799 (1995); **65**, 369 (1996).
- [115] T. Saso and M. Itoh, Phys. Rev. B **53**, 6877 (1996).
- [116] Y. Imai and N. Kawakami, Acta Phys. Pol. B **34**, 779; A. Koga and N. Kawakami, J. Phys.: Condens. Matter **15**, S2215 (2003); R. Sato, T. Ohashi, A. Koga, and N. Kawakami J. Phys. Soc. Jpn. **73**, 1864 (2004); T. Ohashi, A. Koga, S. Suga, and N. Kawakami, Physica B **359-361**, 738 (2005).
- [117] J.K. Freericks, M. Jarrell, and D.J. Scalapino, Phys. Rev. B **48**, 6302 (1993); J.K. Freericks, *ibid.* **50**, 403; J.K. Freericks and M. Jarrell, *ibid.* **50**, 6939 (1994).
- [118] P. Benedetti and R. Zeyher, Phys. Rev. B **58**, 14320 (1998); **59**, 9923 (1999).
- [119] J. Merino and R.H. McKenzie, Phys. Rev. B **62**, 16442 (2000).
- [120] Y. Motome and G. Kotliar, Phys. Rev. B **62**, 12800 (2000).
- [121] J.E. Han, E. Koch, and O. Gunnarsson, Phys. Rev. Lett. **84**, 1276 (2000); J.E. Han, O. Gunnarsson, and V.H. Crespi, *ibid.* **90**, 167006 (2003).
- [122] M. Capone, G. Sangiovanni, C. Castellani, and M. Grilli, Phys. Rev. Lett. **92**, 106401 (2004); G. Sangiovanni, M. Capone, C. Castellani, and M. Grilli, *ibid.* **94**, 026401 (2005); G. Sangiovanni, M. Capone, and C. Castellani, Phys. Rev. B **73**, 165123; G. Sangiovanni, O. Gunnarsson, E. Koch, C. Castellani, and M. Capone, Phys. Rev. Lett. **97**, 046404 (2006).
- [123] Y.-F Yang and K. Held, cond-mat/0603553.
- [124] P. Fazekas, B. Menge, and E. Müller-Hartmann, Z. Phys. B **78**, 69 (1990).
- [125] Th. Pruschke, D.L. Cox, and M. Jarrell, Europhys. Lett. **21**, 593; Phys. Rev. B **47**, 3553 (1993).
- [126] A. Georges and W. Krauth, Phys. Rev. B **48**, 7167 (1993).
- [127] G. Santoro, M. Airoidi, S. Sorella, and E. Tosatti, Phys. Rev. B **47**, 16216 (1993).
- [128] M. Caffarel and W. Krauth, Phys. Rev. Lett. **72**, 1545 (1994).
- [129] C. Gros, W. Wenzel, R. Valentí, G. Hülsenbeck, and J. Stolze, Europhys. Lett. **27**, 299 (1994).
- [130] J. Hong and H.-Y. Kee, Europhys. Lett. **33**, 453 (1996).

- [131] G. Kotliar, Eur. Phys. J. B **11**, 27 (1999); G. Kotliar, E. Lange, and M.J. Rozenberg, Phys. Rev. Lett. **84**, 5180 (2000).
- [132] R. Bulla, Phys. Rev. Lett. **83**, 136 (1999).
- [133] R. Bulla and M. Potthoff, Eur. Phys. J. B **13**, 257 (2000).
- [134] M. Potthoff, Phys. Rev. B **64**, 165114 (2001).
- [135] J. Joo and V. Oudovenko, Phys. Rev. B **64**, 193102 (2001).
- [136] N.-H. Tong, S.-Q. Shen, and F.-C. Pu, Phys. Rev. B **64**, 235109 (2001).
- [137] R. Zitzler, N.-H. Tong, Th. Pruschke, and R. Bulla, Phys. Rev. Lett. **93**, 016406 (2004).
- [138] K. Byczuk, W. Hofstetter, and D. Vollhardt, Phys. Rev. B **69**, 045112 (2004).
- [139] T. Ohashi, N. Kawakami, and H. Tsunetsugu, Phys. Rev. Lett. **97**, 066401 (2006).
- [140] J.K. Freericks and M. Jarrell, Phys. Rev. Lett. **74**, 186 (1995).
- [141] T. Obermeier, T. Pruschke, and J. Keller, Phys. Rev. B **56**, R8479 (1997).
- [142] M. Ulmke, Eur. Phys. J. B **1**, 301 (1998).
- [143] R. Arita, S. Onoda, K. Kuroki, and H. Aoki, J. Phys. Soc. Jpn. **69**, 785 (2000).
- [144] M.H. Hettler, A.N. Tahvildar-Zadeh, M. Jarrell, T. Pruschke, and H.R. Krishnamurthy, Phys. Rev. B **58**, R7475 (1998); M.H. Hettler, M. Mukherjee, M. Jarrell, and H.R. Krishnamurthy, *ibid.* **61**, 12739; Th. Maier, M. Jarrell, Th. Pruschke, and J. Keller, Eur. Phys. J. B **13**, 613 (2000); M. Jarrell, Th. Maier, C. Huscroft, and S. Moukouri, Phys. Rev. B **64**, 195130 (2001); Th.A. Maier, and M. Jarrell, *ibid.* **65**, 041104(R); 249904(E); K. Aryanpour, M.H. Hettler, and M. Jarrell, *ibid.* **65**, 153102 (2002).
- [145] T. Saso, J. Phys. Soc. Jpn. **68**, 3941 (1999); T. Kitajima and T. Saso, Physica B **281-282**, 853 (2000).
- [146] A.I. Lichtenstein and M.I. Katsnelson, Phys. Rev. B **62**, 9283 (2000).
- [147] G. Kotliar, S.Y. Savrasov, G. Pálsson, and G. Biroli, Phys. Rev. Lett. **87**, 186401 (2001); G. Biroli and G. Kotliar, Phys. Rev. B **65**, 155112 (2002).
- [148] P. Sun and G. Kotliar, Phys. Rev. B **66**, 085120 (2002).
- [149] N.E. Zein and V.P. Antropov, Phys. Rev. Lett. **89**, 126402 (2002).
- [150] S. Biermann, F. Aryasetiawan, and A. Georges, Phys. Rev. Lett. **90**, 086402 (2003).

- [151] M. Potthoff, Eur. Phys. J. B **32**, 429; M. Potthoff, M. Aichhorn, and C. Dahnken, Phys. Rev. Lett. **91**, 206402 (2003).
- [152] M.V. Sadovskii, I.A. Nekrasov, E.Z. Kuchinskii, Th. Pruschke, and V.I. Anisimov, Phys. Rev. B **72**, 155105 (2005).
- [153] A. Toschi, A.A. Katanin, and K. Held, cond-mat/0603100.
- [154] H. Kusunose, J. Phys. Soc. Jpn. **75**, 054713 (2006).
- [155] R. Arita, S. Onari, K. Kuroki, and H. Aoki, Physica B **359-361**, 584 (2005); R. Arita and K. Held, Phys. Rev. B **73**, 064515 (2006).
- [156] S. Sakai, R. Arita, and H. Aoki, Phys. Rev. B **70**, 172504 (2004).
- [157] M.J. Rozenberg, Phys. Rev. B **55**, R4855 (1997).
- [158] O. Gunnarsson, E. Koch, and R.M. Martin, Phys. Rev. B **54**, R11026 (1996).
- [159] J.E. Han, M. Jarrell, and D.L. Cox, Phys. Rev. B **58**, R4199 (1998).
- [160] S. Florens, A. Georges, G. Kotliar, and O. Parcollet, Phys. Rev. B **66**, 205102 (2002).
- [161] T. Fujiwara, S. Yamamoto, and Y. Ishii, J. Phys. Soc. Jpn. **72**, 777 (2003).
- [162] K. Inaba, A. Koga, S. Suga, and N. Kawakami, Phys. Rev. B **72**, 085112 (2005).
- [163] O. Miura and T. Fujiwara, J. Phys. Soc. Jpn. **75**, 014703 (2006).
- [164] K. Held and D. Vollhardt, Eur. Phys. J. B **5**, 473 (1998).
- [165] A. Liebsch, Phys. Rev. Lett. **91**, 226401 (2003); Phys. Rev. B **70**, 165103 (2004).
- [166] C. Knecht, N. Blümer, and P. G. J. van Dongen, Phys. Rev. B **72**, 081103(R) (2005); P.G.J. van Dongen, C. Knecht, and N. Blümer, Phys. Status Solidi B **243**, 116 (2006).
- [167] A. Liebsch, Phys. Rev. Lett. **95**, 116402 (2005).
- [168] S. Biermann, L. de' Medici, and A. Georges, Phys. Rev. Lett. **95**, 206401 (2005).
- [169] A. Liebsch and T.A. Costi, Eur. Phys. J. B. **51**, 523 (2006).
- [170] A. Koga, Y. Imai, and N. Kawakami, Phys. Rev. B **66**, 165107 (2002).
- [171] Y. Ōno, M. Potthoff, and R. Bulla, Phys. Rev. B **67**, 035119 (2003).
- [172] T. Momoi and K. Kubo, Phys. Rev. B **58**, R567 (1998).
- [173] J.E. Han, Phys. Rev. B **70**, 054513 (2004).

- [174] A. Koga, N. Kawakami, T.M. Rice, and M. Sigrist, Phys. Rev. Lett. **92**, 216402 (2004).
- [175] A. Koga, N. Kawakami, T. M. Rice, and M. Sigrist, Phys. Rev. B **72**, 045128 (2005).
- [176] R. Arita and K. Held, Phys. Rev. B **72**, 201102(R) (2005).
- [177] K. Inaba, A. Koga, S. Suga, and N. Kawakami, J. Phys. Soc. Jpn. **74**, 2393; A. Koga, K. Inaba, and N. Kawakami, Prog. Theor. Phys. Suppl. **160**, 253 (2005); K. Inaba and A. Koga, Phys. Rev. B **73**, 155106 (2006).
- [178] M. Ferrero, F. Becca, M. Fabrizio, and M. Capone, Phys. Rev. B **72**, 205126 (2005).
- [179] L. de' Medici, A. Georges, and S. Biermann, Phys. Rev. B **72**, 205124 (2005).
- [180] P. Hohenberg and W. Kohn, Phys. Rev. **136**, B864 (1964); W. Kohn and L.J. Sham, *ibid.* **140**, A1133 (1965).
- [181] R.O. Jones and O. Gunnarsson, Rev. Mod. Phys. **61**, 689 (1989).
- [182] A. Fujimori, I. Hase, H. Namatame, Y. Fujishima, Y. Tokura, H. Eisaki, S. Uchida, K. Takegahara, and F.M.F. de Groot, Phys. Rev. Lett. **69**, 1796; A. Fujimori, I. Hase, M. Nakamura, H. Namatame, Y. Fujishima, Y. Tokura, M. Abbate, F.M.F. de Groot, M.T. Czyzyk, J.C. Fuggle, O. Strebel, F. Lopez, M. Domke, and G. Kaindl, Phys. Rev. B **46**, 9841 (1992).
- [183] Y. Okimoto, T. Katsufuji, Y. Okada, T. Arima, and Y. Tokura, Phys. Rev. B **51**, 9581 (1995).
- [184] I. Solovyev, N. Hamada, and K. Terakura, Phys. Rev. B **53**, 7158 (1996).
- [185] F. Aryasetiawan and O. Gunnarsson, Rep. Prog. Phys. **61**, 237 (1998).
- [186] V.I. Anisimov, F. Aryasetiawan, and A.I. Lichtenstein, J. Phys.: Condens. Matter **9**, 767 (1997).
- [187] A.I. Lichtenstein and M.I. Katsnelson, Phys. Rev. B **57**, 6884 (1998).
- [188] V.I. Anisimov, A.I. Poteryaev, M.A. Korotin, A.O. Anokhin, and G. Kotliar, J. Phys.: Condens. Matter **9**, 7359 (1997).
- [189] K. Held, I.A. Nekrasov, G. Keller, V. Eyert, N. Blümer, A.K. McMahan, R.T. Scalettar, Th. Pruschke, V.I. Anisimov, and D. Vollhardt, Psi-k Newsletter **56**, 65 (2003); K. Held, Habilitation thesis, Stuttgart University, 2004 (cond-mat/0511293).
- [190] G. Kotliar, S.Y. Savrasov, K. Haule, V.S. Oudovenko, O. Parcollet, and C.A. Marianetti, Rev. Mod. Phys. **78**, 865 (2006).

- [191] S.Y. Savrasov, G. Kotliar, and E. Abrahams, *Nature* **410**, 793 (2001); G. Kotliar and S.Y. Savrasov, *Int. J. Mod. Phys. B* **17**, 5101 (2003).
- [192] K. Held, A.K. McMahan, and R.T. Scalettar, *Phys. Rev. Lett.* **87**, 276404 (2001); A.K. McMahan, K. Held, and R.T. Scalettar, *Phys. Rev. B* **67**, 075108 (2003).
- [193] A.K. McMahan, *Phys. Rev. B* **72**, 115125 (2005).
- [194] V.I. Anisimov, D.E. Kondakov, A.V. Kozhevnikov, I.A. Nekrasov, Z.V. Pchelkina, J.W. Allen, S.-K. Mo, H.-D. Kim, P. Metcalf, S. Suga, A. Sekiyama, G. Keller, I. Leonov, X. Ren, and D. Vollhardt, *Phys. Rev. B* **71**, 125119 (2005).
- [195] Z.V. Pchelkina, I.A. Nekrasov, Th. Pruschke, A. Sekiyama, S. Suga, V.I. Anisimov, and D. Vollhardt, *cond-mat/0601507*.
- [196] M.S. Laad, L. Craco, and E. Müller-Hartmann, *Europhys. Lett.* **69**, 984 (2005); *Phys. Rev. B* **73**, 045109; 195120 (2006).
- [197] K. Held, I.A. Nekrasov, N. Blümer, V.I. Anisimov, and D. Vollhardt, *Int. J. Mod. Phys. B* **15**, 2611; I.A. Nekrasov, K. Held, N. Blümer, A.I. Poteryaev, V.I. Anisimov, and D. Vollhardt, *Eur. Phys. J. B* **18**, 55 (2000).
- [198] M.B. Zöfl, T. Pruschke, J. Keller, A.I. Poteryaev, I.A. Nekrasov, and V.I. Vollhardt, *Phys. Rev. B* **61**, 12810 (2000).
- [199] E. Pavarini, S. Biermann, A. Poteryaev, A.I. Lichtenstein, A. Georges, and O.K. Andersen, *Phys. Rev. Lett.* **92**, 176403 (2004).
- [200] I.H. Inoue, I. Hase, Y. Aiura, A. Fujimori, K. Morikawa, T. Mizokawa, Y. Haruyama, T. Maruyama, and Y. Nishihara, *Physica C* **235-240**, 1007 (1994); K. Morikawa, T. Mizokawa, K. Kobayashi, A. Fujimori, H. Eisaki, S. Uchida, F. Iga, and Y. Nishihara, *Phys. Rev. B* **52**, 13711 (1995).
- [201] I.H. Inoue, O. Goto, H. Makino, N.E. Hussey, M. Ishikawa, *Phys. Rev. B* **58**, 4372; H. Makino, I.H. Inoue, M.J. Rozenberg, I. Hase, Y. Aiura, S. Onari, *ibid.* **58**, 4384 (1998); K. Maiti, D.D. Sarma, M.J. Rozenberg, I.H. Inoue, H. Makino, O. Goto, M. Pedio, and R. Cimino, *Europhys. Lett.* **55**, 246 (2001).
- [202] A. Sekiyama, H. Fujiwara, S. Imada, S. Suga, H. Eisaki, S.I. Uchida, K. Takegahara, H. Harima, Y. Saitoh, I.A. Nekrasov, G. Keller, D.E. Kondakov, A.V. Kozhevnikov, Th. Pruschke, K. Held, D. Vollhardt, and V.I. Anisimov, *Phys. Rev. Lett.* **93**, 156402 (2004); I.A. Nekrasov, G. Keller, D.E. Kondakov, A.V. Kozhevnikov, Th. Pruschke, K. Held, D. Vollhardt, and V.I. Anisimov, *Phys. Rev. B* **72**, 155106 (2005); I.A. Nekrasov, K. Held, G. Keller, D.E. Kondakov, T. Pruschke, M. Kollar, O.K. Andersen, V.I. Anisimov, and D. Vollhardt, *ibid.* **73**, 155112 (2006).
- [203] A. Liebsch, *Phys. Rev. Lett.* **90**, 096401 (2003).

- [204] F. Lechermann, A. Georges, A. Poteryayev, S. Biermann, M. Posternak, A. Yamasaki, and O.K. Andersen, Phys. Rev. B **74**, 125120 (2006).
- [205] K. Held, G. Keller, V. Eyert, V.I. Anisimov, and D. Vollhardt, Phys. Rev. Lett. **86**, 5345 (2001); G. Keller, K. Held, V. Eyert, V.I. Anisimov, and D. Vollhardt, Phys. Rev. B **70**, 205116 (2004).
- [206] S.-K. Mo, J.D. Denlinger, H.-D. Kim, J.-H. Park, J.W. Allen, A. Sekiyama, A. Yamasaki, K. Kadono, S. Suga, Y. Saitoh, T. Muro, P. Metcalf, G. Keller, K. Held, V. Eyert, V.I. Anisimov, and D. Vollhardt, Phys. Rev. Lett. **90**, 186403 (2003); S.-K. Mo, H.-D. Kim, J.W. Allen, G.-H. Gweon, J.D. Denlinger, J.-H. Park, A. Sekiyama, A. Yamasaki, S. Suga, P. Metcalf, and K. Held, *ibid.* **93**, 076404 (2004).
- [207] M.S. Laad, L. Craco, and E. Müller-Hartmann, Phys. Rev. Lett. **91**, 156402 (2003).
- [208] F. Lechermann, S. Biermann, and A. Georges, Phys. Rev. Lett. **94**, 166402 (2005).
- [209] V.I. Anisimov, M.A. Korotin, M. Zöfl, T. Pruschke, K. Le Hur, and T.M. Rice, Phys. Rev. Lett. **83**, 364 (1999); I.A. Nekrasov, Z.V. Pchelkina, G. Keller, T. Pruschke, K. Held, A. Krimmel, D. Vollhardt, and V.I. Anisimov, Phys. Rev. B **67**, 085111 (2003).
- [210] A.I. Lichtenstein, M.I. Katsnelson, and G. Kotliar, Phys. Rev. Lett. **87**, 067205 (2001).
- [211] A. Yamasaki, M. Feldbacher, Y.-F. Yang, O.K. Andersen, and K. Held, Phys. Rev. Lett. **96**, 166401 (2006).
- [212] A. Liebsch and A.I. Lichtenstein, Phys. Rev. Lett. **84**, 1591 (2000).
- [213] L. Craco, M.S. Laad, and E. Müller-Hartmann, Phys. Rev. Lett. **90**, 237203; Phys. Rev. B **68**, 233310 (2003).
- [214] H. Ishida, M.D. Johannes, and A. Liebsch, Phys. Rev. Lett. **94**, 196401 (2005).
- [215] R. Arita, T. Miyake, T. Kotani, M. van Schilfhaarde, T. Oka, K. Kuroki, Y. Nozue, and H. Aoki, Phys. Rev. B **69**, 195106 (2004).
- [216] M.B. Zöfl, I.A. Nekrasov, Th. Pruschke, V.I. Anisimov, and J. Keller, Phys. Rev. Lett. **87**, 276403 (2001); K. Haule, V. Oudovenko, S.Y. Savrasov, and G. Kotliar, *ibid.* **94**, 036401 (2005).
- [217] A.I. Poteryaev, A.I. Lichtenstein, and G. Kotliar, Phys. Rev. Lett. **93**, 086401 (2004).
- [218] H. Kajueter and G. Kotliar, Phys. Rev. Lett. **77**, 131 (1996).
- [219] M. Potthoff, T. Wegner, and W. Nolting, Phys. Rev. B **55**, 16132 (1997).

- [220] Th. Pruschke and N. Grewe, *Z. Phys. B* **74**, 439 (1989).
- [221] J.E. Hirsch, *Phys. Rev. B* **28**, 4059 (1983); **29**, 4159 (1984).
- [222] J.E. Hirsch and R.M. Fye, *Phys. Rev. Lett.* **56**, 2521 (1986); R.M. Fye and J.E. Hirsch, *Phys. Rev. B* **38**, 433 (1988).
- [223] R. Blankenbecler, D.J. Scalapino, and R.L. Sugar, *Phys. Rev. D* **24**, 2278 (1981).
- [224] Y. Motome and M. Imada, *J. Phys. Soc. Jpn.* **66**, 1872 (1997); **67**, 3199 (1998).
- [225] M. Feldbacher, K. Held, and F.F. Assaad, *Phys. Rev. Lett.* **93**, 136405 (2004).
- [226] G.G. Batrouni and R. T. Scalettar, *Phys. Rev. B* **42**, 2282 (1990); G.G. Batrouni and P. de Forcrand, *ibid.* **48**, 589 (1993).
- [227] N. Furukawa and M. Imada, *J. Phys. Soc. Jpn.* **60**, 810 (1991).
- [228] J. Yoo, S. Chandrasekharan, R.K. Kaul, D. Ullmo, and H.U. Baranger, *J. Phys. A: Math. Gen.* **38**, 10307 (2005).
- [229] S.M.A. Rombouts, K. Heyde, and N. Jachowicz, *Phys. Rev. Lett.* **82**, 4155 (1999).
- [230] S. Rombouts, K. Heyde, and N. Jachowicz, *Phys. Lett. A* **242**, 271 (1998).
- [231] A.N. Rubtsov and A.I. Lichtenstein, *JETP Lett.* **80**, 61 (2004); A.N. Rubtsov, V.V. Savkin, and A.I. Lichtenstein, *Phys. Rev. B* **72**, 035122 (2005).
- [232] P. Werner, A. Comanac, L. de' Medici, A.J. Millis, and M. Troyer, *Phys. Rev. Lett.* **97**, 076405 (2006); P. Werner and A.J. Millis, cond-mat/0607136.
- [233] S. Sakai, R. Arita, and H. Aoki, *Physica B* **378-380**, 288 (2006).
- [234] S. Sakai, R. Arita, K. Held, and H. Aoki, *Phys. Rev. B* **74**, 155102 (2006).
- [235] A. Barbieri and A.P. Young, *J. Phys.: Condens. Matter* **3**, 1801 (1991).
- [236] I.V. Solov'yev and M. Imada, *Phys. Rev. B* **71**, 045103 (2005).
- [237] T. Wegner, M. Potthoff, and W. Nolting, *Phys. Rev. B* **57**, 6211 (1998).
- [238] W. Gill and D.J. Scalapino, *Phys. Rev. B* **35**, 215 (1987).
- [239] K. Kusakabe and H. Aoki, *Physica B* **194-196**, 217 (1994).
- [240] J. Kuei and R.T. Scalettar, *Phys. Rev. B* **55**, 14968 (1997).
- [241] J.E. Hirsch, *Phys. Rev. B* **56**, 11022 (1997).
- [242] H. Sakamoto, T. Momoi, and K. Kubo, *Phys. Rev. B* **65**, 224403 (2002).

- [243] J. Bünemann, W. Weber, and F. Gebhard, Phys. Rev. B **57**, 6896 (1998); J. Bünemann, F. Gebhard, and W. Weber, Found. Phys. **30**, 2011 (2000); J. Bünemann, F. Gebhard, T. Ohm, R. Umstätter, R. Weiser, W. Weber, R. Claessen, D. Ehm, A. Harasawa, A. Kakizaki, A. Kimura, G. Nicolay, S. Shin, and V.N. Strocov, Europhys. Lett. **61**, 667 (2003).
- [244] K. Held and D. Vollhardt, Phys. Rev. Lett. **84**, 5168 (2000).
- [245] A. Liebsch, Phys. Rev. B **23**, 5203 (1981).
- [246] T.M. Rice and M. Sigrist, J. Phys.: Condens. Matter **7**, L643 (1995).
- [247] T. Oguchi, Phys. Rev. B **51**, 1385(R) (1995).
- [248] D.J. Singh, Phys. Rev. B **52**, 1358 (1995); I.I. Mazin and D.J. Singh, Phys. Rev. Lett. **79**, 733 (1997).
- [249] I. Hase and Y. Nishihara, J. Phys. Soc. Jpn. **65**, 3957 (1996).
- [250] A.V. Puchkov, Z.-X. Shen, T. Kimura, and Y. Tokura, Phys. Rev. B **58**, R13322 (1998).
- [251] T. Okuda, H. Daimon, M. Kotsugi, K. Nakatsuji, M. Fujikawa, S. Suga, Y. Tezuka, S. Shin, M. Kasai, and Y. Tokura, J. Electron Spectrosc. Relat. Phenom. **88-91**, 473 (1998).
- [252] A. Damascelli, D.H. Lu, K.M. Shen, N.P. Armitage, F. Ronning, D.L. Feng, C. Kim, Z.-X. Shen, T. Kimura, Y. Tokura, Z.Q. Mao, and Y. Maeno, Phys. Rev. Lett. **85**, 5194 (2000); **87**, 239702; A. Liebsch, *ibid.* **87**, 239701 (2001).
- [253] A. Sekiyama, S. Kasai, M. Tsunekawa, Y. Ishida, M. Sing, A. Irizawa, A. Yamasaki, S. Imada, T. Muro, Y. Saitoh, Y. Ōnuki, T. Kimura, Y. Tokura, and S. Suga, Phys. Rev. B **70**, 060506(R); A. Sekiyama and S. Suga, J. Electron Spectrosc. Relat. Phenom. **137-140**, 681 (2004).
- [254] A.P. Mackenzie, S.R. Julian, A.J. Diver, G.J. McMullan, M.P. Ray, G.G. Lonzarich, Y. Maeno, S. Nishizaki, and T. Fujita, Phys. Rev. Lett. **76**, 3786 (1996); C. Bergemann, J.S. Brooks, L. Balicas, A.P. Mackenzie, S.R. Julian, Z.Q. Mao, and Y. Maeno, Physica B **294**, 371 (2001).
- [255] T. Yokoya, A. Chainani, T. Takahashi, H. Katayama-Yoshida, M. Kasai, Y. Tokura, N. Shanthi, and D.D. Sarma, Phys. Rev. B **53**, 8151; T. Yokoya, A. Chainani, T. Takahashi, H. Katayama-Yoshida, M. Kasai, and Y. Tokura, Phys. Rev. Lett. **76**, 3786 (1996); **78**, 2272 (1997); T. Yokoya, A. Chainani, T. Takahashi, H. Ding, J.C. Campuzano, H. Katayama-Yoshida, M. Kasai, and Y. Tokura, Phys. Rev. B **54**, 13311 (1996).

- [256] I.H. Inoue, Y. Aiura, Y. Nishihara, Y. Haruyama, S. Nishizaki, Y. Maeno, T. Fujita, J.G. Bednorz, and F. Lichtenberg, *Physica B* **223-224**, 516; I.H. Inoue, Y. Aiura, Y. Nishihara, Y. Haruyama, S. Nishizaki, Y. Maeno, T. Fujita, F. Lichtenberg, and J.G. Bednorz, *J. Electron Spectrosc. Relat. Phenom.* **78**, 175 (1996); I.H. Inoue, A. Kimura, A. Harasawa, A. Kakizaki, Y. Aiura, S. Ikeda, and Y. Maeno, *J. Phys. Chem. Solids* **59**, 2205 (1998).
- [257] M. Schmidt, T.R. Cummins, M. Bürk, D.H. Lu, N. Nücker, S. Schuppler, and F. Lichtenberg, *Phys. Rev. B* **53**, R14761 (1996).
- [258] E.Z. Kurmaev, S. Stadler, D.L. Ederer, Y. Harada, S. Shin, M.M. Grush, T.A. Callcott, R.C.C. Pereira, D.A. Zatsopin, N. Ovechkina, M. Kasai, Y. Tokura, T. Takahashi, K. Chandrasekharan, R. Vijayaraghavan, and U.V. Varadaraju, *Phys. Rev. B* **57**, 1558 (1998).
- [259] T.T. Tran, T. Mizokawa, S. Nakatsuji, H. Fukazawa, and Y. Maeno, *Phys. Rev. B* **70**, 153106 (2004).
- [260] T. Katsufuji, M. Kasai, and Y. Tokura, *Phys. Rev. Lett.* **76**, 126 (1996).
- [261] Y. Maeno, S. Nishizaki, K. Yoshida, S. Ikeda, and T. Fujita, *J. Low. Temp. Phys.* **105**, 1577 (1996).
- [262] A. Pérez-Navarro, J. Costa-Quintana, and F. López-Aguilar, *Phys. Rev. B* **61**, 10125 (2000).
- [263] L. Walz and F. Lichtenberg, *Acta Cryst. C* **49**, 1268 (1993).
- [264] Y. Maeno, *Physica C* **282-287**, 206 (1997).
- [265] J.E. Gubernatis, M. Jarrell, R.N. Silver, and D.S. Sivia, *Phys. Rev. B* **44**, 6011 (1991); M. Jarrell and J.E. Gubernatis, *Phys. Rep.* **269**, 133 (1996).
- [266] M. Braden, W. Reichardt, S. Nishizaki, Y. Mori, and Y. Maeno, *Phys. Rev. B* **57**, 1236 (1998).
- [267] S.A. Grigera, R.S. Perry, A.J. Schofield, M. Chiao, S.R. Julian, G.G. Lonzarich, S.I. Ikeda, Y. Maeno, A.J. Millis, and A.P. Mackenzie, *Science* **294**, 329 (2001); R.S. Perry, K. Kitagawa, S.A. Grigera, R.A. Borzi, A.P. Mackenzie, K. Ishida, and Y. Maeno, *Phys. Rev. Lett.* **92**, 166602 (2004); R.S. Perry, T. Tayama, K. Kitagawa, T. Sakakibara, K. Ishida, and Y. Maeno, *J. Phys. Soc. Jpn.* **74**, 1270 (2005).
- [268] M.K. Crawford, R.L. Harlow, W. Marshall, Z. Li, G. Cao, R.L. Lindstrom, and Q. Huang, and J.W. Lynn, *Phys. Rev. B* **65**, 214412 (2002); G. Cao, L. Balicas, W.H. Song, Y.P. Sun, Y. Xin, V.A. Bondarenko, J.W. Brill, S. Parkin, and X.N. Lin, *ibid.* **68**, 174409 (2003).

- [269] J.J. Randall and R. Ward, *J. Am. Chem. Soc.* **81**, 2629 (1959); A. Callaghan, C.W. Moeller, and R. Ward, *Inorg. Chem.* **5**, 1572 (1966); A. Kanbayasi, *J. Phys. Soc. Jpn.* **41**, 1876 (1976); G. Cao, S. McCall, M. Shepard, J.E. Crow, and R.P. Guertin, *Phys. Rev. B* **56**, 321 (1997).
- [270] F. Nakamura, T. Goto, M. Ito, T. Fujita, S. Nakatsuji, H. Fukazawa, and Y. Maeno, *Phys. Rev. B* **65**, 220402(R) (2002).